

**ALTERNATIVE TECHNIQUES OF BACKSCATTER RADIOGRAPHY:
SNAPSHOT APERTURE BACKSCATTER RADIOGRAPHY AND
COLLIMATED SEGMENTED DETECTOR SCATTER X-RAY IMAGING**

By

OLIVIER BOUGEANT

A THESIS PRESENTED TO THE GRADUATE SCHOOL
OF THE UNIVERSITY OF FLORIDA IN PARTIAL FULFILLMENT
OF THE REQUIREMENTS FOR THE DEGREE OF
MASTER OF SCIENCE

UNIVERSITY OF FLORIDA

2009

© 2009 Olivier Bougeant

To my family: Alain, Christiane, Carole and Nathalie, and to Verena

ACKNOWLEDGMENTS

I would like to thank Dr. Edward Dugan, my advisor, for his precious guidance and for sharing with me his knowledge and his wisdom during the past two years. I thank Dr. James Baciak for being on the committee.

I would also like to thank Dan Shedlock who offered valuable help, Dan Ekdahl, Georgi Gorgiev, and my colleagues and friends: Nissia Sabri, Christopher Meng and Kara Beharry. I thank all the students, professors and staff members at the department of Nuclear and Radiological Engineering for so warmly welcoming me and for making me feel at home in Florida.

Finally, I would like to thank my family and all my friends for their unconditional support. I especially want to thank Verena, my girlfriend, for her love and her patience.

Financial acknowledgment:

- University of Florida, Department of Nuclear and Radiological Engineering
- Nucsafe

TABLE OF CONTENTS

| | <u>page</u> |
|--|-------------|
| ACKNOWLEDGMENTS..... | 4 |
| LIST OF FIGURES | 7 |
| ABSTRACT | 12 |
| CHAPTER | |
| 1 INTRODUCTION..... | 14 |
| Radiography by Selective Detection..... | 14 |
| Limits to Radiography by Selective Detection..... | 15 |
| 2 SABR: INTRODUCTION..... | 19 |
| Snapshot Backscatter Radiography..... | 19 |
| Principle of SABR..... | 20 |
| Experimental Setup for SABR | 21 |
| 3 SABR: IMPORTANT FACTORS ON IMAGE QUALITY..... | 26 |
| Effects of the X-ray Generator Configuration..... | 26 |
| Exposure..... | 26 |
| Voltage | 27 |
| Notes on MCNP Photon Source for SABR Simulations..... | 28 |
| Effects of the Substrate | 30 |
| Effects of the Size of the Lead Tiles | 32 |
| Effect of a Gap Between the CR Plate and the Object | 33 |
| Effect of a Gap Between the Object and the Substrate | 34 |
| 4 SABR: VARIOUS OBJECTS THAT HAVE BEEN IMAGED | 45 |
| SABR Images of a Spray-on-Foam Insulation Block..... | 46 |
| SABR Images of a Corroded Piece of Aluminum | 47 |
| Other Objects that have been Imaged with the SABR Technique | 49 |
| 5 SABR: CONCLUSIONS | 56 |
| 6 CSD-SXI: INTRODUCTION | 58 |
| Computed Image Backscatter Radiography | 58 |
| Backscatter Radiography using an Uncollimated Segmented Detector | 58 |

| | | |
|----------|---|------------|
| 7 | CSD-SXI: PRINCIPLE AND MONTE CARLO SIMULATIONS | 65 |
| | Principle of Collimated Segmented Detector Scatter X-ray Imaging..... | 65 |
| | Resolution | 68 |
| | Influence of Collimation..... | 69 |
| | Depth information and Possibility of 3D Imaging | 71 |
| | 2D Collimation Grid for Better Depth Resolution | 71 |
| | Possibility of 3D Backscatter Imaging | 72 |
| | CSD-SXI 3D Imaging: Example of a Ring of Air Inside Aluminum | 75 |
| 8 | CSD-SXI: CONSTRUCTION AND TEST OF A FIRST PROTOTYPE..... | 92 |
| | Experimental Setup | 92 |
| | Segmented Detector..... | 92 |
| | Collimation Grid..... | 93 |
| | X-ray fan Beam Source | 94 |
| | Test of the First CSD-SXI Prototype | 94 |
| | Contrast and Details..... | 94 |
| | Resolution and Modulation Transfer Function (MTF) for CSD-SXI | 95 |
| | Depth Penetration | 96 |
| 9 | CSD-SXI: CONCLUSIONS AND FUTURE WORK | 108 |
| | LIST OF REFERENCES | 110 |
| | BIOGRAPHICAL SKETCH | 111 |

LIST OF FIGURES

| <u>Figure</u> | | <u>page</u> |
|---------------|---|-------------|
| 1-1 | Principle of backscatter Radiography by Selective Detection | 17 |
| 1-2 | NaI and YSO detectors mounted on a pencil beam RSD system..... | 17 |
| 1-3 | Scanning pattern of pencil beam RSD systems..... | 18 |
| 2-1 | Letters of lead on a nylon substrate..... | 23 |
| 2-2 | Principle of Shadow Aperture Backscatter Radiography | 23 |
| 2-3 | Differential scattering cross section per unit solid angle at 1 keV, 100 keV and 2 MeV..... | 24 |
| 2-4 | SR 115 portable X-ray generator | 24 |
| 2-5 | Typical energy spectrum of a medical X-ray generator at 75 kVp with and without aluminum filter | 25 |
| 2-6 | Assemblies of 1", 1.5" and 2" lead tiles..... | 25 |
| 3-1 | Foreign Object Debris on a nylon substrate | 36 |
| 3-2 | Geometry of the MCNP simulation of the Shadow Aperture Backscatter Radiography of a steel washer on a nylon substrate. | 36 |
| 3-3 | Flux of photons received after a MCNP simulation by each point of the CR plate for three photon energy..... | 36 |
| 3-4 | Flux of photons received after a MCNP simulation by each 0.5 pixel of the CR plate.... | 37 |
| 3-5 | Steel Washer on nylon background..... | 37 |
| 3-6 | Foreign Object Debris on a nylon substrate | 38 |
| 3-7 | MCNP simulated SABR images | 38 |
| 3-8 | Foreign Object Debris on an aluminum substrate..... | 39 |
| 3-9 | Profile plot of the previous SABR image on which can be seen two features (the hole in the large washer and a small washer). | 39 |
| 3-10 | Foreign Object Debris on a lead substrate | 40 |
| 3-11 | MCNP simulated SABR images of a steel washer | 40 |

| | | |
|------|--|----|
| 3-12 | Foreign Object Debris on a nylon substrate | 41 |
| 3-13 | MCNP simulated SABR images of a steel washer on a nylon background..... | 41 |
| 3-14 | SABR images of Foreign Object Debris on a nylon background at 75 kVp, 60mAs, at 25 inches | 42 |
| 3-15 | Possible paths of photons backscattered in the target object..... | 42 |
| 3-16 | Geometry of the MCNP simulation of the Shadow Aperture Backscatter Radiography of a steel washer on a nylon substrate, with a 4 mm gap between the washer and the CR plate | 43 |
| 3-17 | MCNP simulated SABR images of a steel washer on a nylon background..... | 43 |
| 3-18 | Nylon washer suspended by a thread over a lead background..... | 43 |
| 3-19 | Geometry of the MCNP simulation of the Shadow Aperture Backscatter Radiography of a steel washer located 3.5 inches over a nylon substrate..... | 44 |
| 3-20 | MCNP simulated SABR images of a steel washer on a nylon background..... | 44 |
| 4-1 | SABR of Foreign Object Debris on a nylon background taken at 75 kVp, 60 mAs, 25 inches | 50 |
| 4-2 | MCNP simulated SABR images of a steel washer on a nylon background..... | 50 |
| 4-3 | SABR of Foreign Object Debris on a nylon background taken at 75 kVp, 60 mAs, 25 inches | 51 |
| 4-4 | Block of spray-on-foam insulation..... | 51 |
| 4-5 | Five holes, 0.75 inch in diameter and of different depth in a spray-on-foam block | 52 |
| 4-6 | Five dimes placed in holes drilled in foam, 0.75 inch in diameter and of different depth..... | 52 |
| 4-7 | Zoom of the area of the previous SABR image that contained the third coin. | 53 |
| 4-8 | Corroded aluminum plate on a nylon background | 53 |
| 4-9 | Corroded aluminum plate suspended 3.5 inches over a nylon background | 54 |
| 4-10 | Corroded aluminum plate covered by a 1mm thick aluminum plate and suspended 3.5 inches over a nylon background..... | 54 |
| 4-11 | Image enhancement of the previous SABR image with features surrounded in red | 55 |
| 6-1 | Backscatter radiography images with a 1 mm resolution of letters of lead on nylon..... | 62 |

| | | |
|------|---|----|
| 6-2 | Geometry of the MCNP simulation of the backscatter radiography of a lead strip on a nylon background using an uncollimated segmented detector..... | 62 |
| 6-3 | Energy spectrum of the X-ray source at 65 kVp..... | 63 |
| 6-4 | Geometry of the MCNP simulation of the pencil beam backscatter radiography of a lead strip on a nylon background | 63 |
| 6-5 | Comparison between the normalized fluxes observed in the uncollimated array detector with a fan beam source and with a pencil beam source. | 64 |
| 6-6 | Possible paths of backscattered X-ray photons toward the uncollimated segmented detector with a fan beam source..... | 64 |
| 7-1 | Geometry of the MCNP simulation of a Collimated Segmented Detector Scatter X-ray Image of a lead strip on a nylon background | 79 |
| 7-2 | Possible paths of backscattered X-ray photons from a fan beam source toward the segmented detector..... | 79 |
| 7-3 | Comparison between the normalized fluxes observed in the collimated array detector with a fan beam source and with a pencil beam source for a lead strip on the surface of a nylon block..... | 80 |
| 7-4 | Possible paths of X-ray photons eventually reaching an image pixel. | 80 |
| 7-5 | Measure of the resolution for Collimated Segmented Detector Scatter X-ray Imaging.... | 81 |
| 7-6 | Backscatter X-ray secondary source as seen from point $y = t$ | 81 |
| 7-7 | Normalized contribution to a 0.6 mm wide pixel, with a 1 cm collimation..... | 82 |
| 7-8 | Geometry of the MCNP simulation of a Collimated Segmented Detector Scatter X-ray Image of a lead strip 2 cm deep inside a nylon block..... | 82 |
| 7-9 | Comparison between the normalized fluxes observed in the collimated array detector with a fan beam source and with a pencil beam source for a lead strip 2 cm deep in a nylon block | 83 |
| 7-10 | Comparison between the normalized fluxes observed in the collimated array detector with a fan beam source for four different collimation lengths for a lead strip 2 cm deep in a nylon block | 83 |
| 7-11 | Geometry of the MCNP simulation of a Collimated Segmented Detector Scatter X-ray Image of a 1 cm deep air gap inside an aluminum block with a 2D grid collimated detector at a 45° inclination | 84 |
| 7-12 | Geometries of the 3 MCNP simulations of an air gap inside an aluminum block, views of the XZ-plane..... | 84 |

| | | |
|------|--|-----|
| 7-13 | Comparison between the normalized fluxes from MCNP simulations of a 1 cm deep air gap inside an aluminum block with a fan beam source..... | 85 |
| 7-14 | Geometry of the 2D collimated array detector at a 45° inclination, view of the XZ-plane | 85 |
| 7-15 | Backscatter X-ray secondary source as seen from point t | 86 |
| 7-16 | Normalized contribution of each z-level in the target object to all 6 rows of pixels and to the sum of the rows..... | 87 |
| 7-17 | Comparison between the fluxes recorded by rows 1, 2, 3, 4, 5 and 6 of the 2D collimated array detector, with a 45° inclination from an MCNP simulation of CSD-SXI of an air gap inside an aluminum block | 87 |
| 7-18 | Geometry of the ring of air located 1 cm deep inside aluminum..... | 88 |
| 7-19 | Geometries of the three different imaging systems..... | 88 |
| 7-20 | MCNP generated X-ray backscatter images of a ring of air inside aluminum using a NaI detector with a pencil beam source with the following collimation lengths..... | 89 |
| 7-21 | MCNP generated X-ray backscatter images of a ring of air inside aluminum using a linearly collimated segmented detector with a fan beam source with the following collimation lengths | 89 |
| 7-22 | MCNP generated X-ray backscatter images of a ring of air inside aluminum using a 2D collimated segmented detector at a 45° inclination with a fan beam source..... | 90 |
| 7-23 | Z-levels corresponding to each of the six MCNP generated images of the ring of air | 91 |
| 8-1 | Photograph of the 12" Envision Product Design segmented detector | 98 |
| 8-2 | Simplified diagram of the segmented detector used for CSD-SXI | 98 |
| 8-3 | Segmented detector mounted on the X-ray tube at a 40° angle | 99 |
| 8-4 | Flux detected by the linearly segmented detector with and without the X-rays on | 99 |
| 8-5 | Collimation grid made of 0.4 mm thick lead..... | 100 |
| 8-6 | Lead collimation grid mounted on the bottom surface of the segmented detector | 100 |
| 8-7 | CSD-SXI image of letters of lead (1 mm thick) on nylon | 101 |
| 8-8 | Lead collimation grids made of 0.4 mm and 1.08 mm thick lead plates and spacers..... | 101 |
| 8-9 | Explanation of the apparition of artifacts in CSD-SXI images when the collimation grid pitch does not match the size of pixel bins | 102 |

| | | |
|------|---|-----|
| 8-10 | CSD-SXI images of a disk of lead on nylon | 102 |
| 8-11 | Lead shield with a 1 mm slit..... | 103 |
| 8-12 | Lead shield with variable aperture, in this case 0.2 mm..... | 103 |
| 8-13 | Various objects on an aluminum background | 104 |
| 8-14 | Letters of lead on a nylon background..... | 104 |
| 8-15 | Lead test pattern on an aluminum background | 105 |
| 8-16 | Modulation Transfer Functions (MTF) for the CSD-SXI and RSD images shown in Figure 8-15..... | 106 |
| 8-17 | Various objects on an aluminum background | 106 |
| 8-18 | Various objects on an aluminum background | 107 |
| 8-19 | Various objects on an aluminum background | 107 |

Abstract of Thesis Presented to the Graduate School
of the University of Florida in Partial Fulfillment of the
Requirements for the Degree of Master of Science

ALTERNATIVE TECHNIQUES OF BACKSCATTER RADIOGRAPHY:
SNAPSHOT APERTURE BACKSCATTER RADIOGRAPHY AND
COLLIMATED SEGMENTED DETECTOR SCATTER X-RAY IMAGING

By

Olivier Bougeant

August 2009

Chair: Edward T. Dugan

Major: Nuclear Engineering Sciences

Unlike standard transmission radiography, Compton Backscatter Imaging (CBI) techniques are non-destructive examination methods that rely on the detection of X-ray photons *backscattered* in the target object. They have the advantage of being single-sided imaging techniques and can yield better images than transmission radiography for certain applications.

The X-ray backscatter imaging system currently used at the University of Florida employs a method called Radiography by Selective Detection (RSD). It uses an X-ray pencil beam to illuminate the target object while scintillation detectors positioned around the X-ray source count backscattered photons. As the X-ray beam scans the target object, one real-time 2D image is created per detector based on the recorded counts. Lead collimation sleeves placed around the detector prevent particles scattered above a given depth from being detected, and help provide good depth information in RSD images. This system has been commercialized and can be used for detection of land mines, security inspections and detection of defects or foreign object debris. One of the drawbacks of this technique, however, is the image acquisition time, especially when detectors are highly collimated. The two X-ray backscatter imaging techniques presented in this thesis were originally designed to yield images with a shorter acquisition time.

Snapshot Aperture Backscatter Radiography (SABR) is a single-sided Compton Backscatter Imaging technique that is based on a snapshot acquisition method, contrary to most other X-ray Backscatter Imaging systems which generate images by scanning. This characteristic of the SABR technique greatly reduces image acquisition time. The detector used with this technique is a CR plate shielded from direct X-ray radiations by a lattice of lead tiles: X-rays illuminate the target object through apertures between the lead tiles and are backscattered toward the CR plate. However, both Monte Carlo simulations and actual experiments have shown that this technique, with the employed aperture arrangements, yields images with poor depth information.

Collimated Segmented Detector-based Scatter X-ray Imaging (CSD-SXI) is a new backscatter radiography technique. Its principle relies on the use of a pixelated detector, collimated by a fine grid of a strongly absorbing material. The X-ray source comes in the form of a fan beam, parallel to the segmented detector. Monte Carlo simulations and the first practical experimental tests have shown very promising results in both image quality and depth information.

CHAPTER 1

INTRODUCTION

The purpose of this work is to present two new X-ray backscatter imaging techniques: Snapshot Aperture Backscatter Radiography (SABR) and Collimated Segmented Detector Scatter X-ray Imaging (CSD-SXI), both originally designed to yield faster images than existing Compton Backscatter Imaging (CBI) systems currently used at the University of Florida, while bringing additional information.

Radiography by Selective Detection

Backscatter Radiography by Selective Detection (RSD) is a single-sided imaging technique developed by the Scatter X-Ray Imaging (SXI) group at the University of Florida. Its principle is shown in Figure 1-1. X-rays are emitted in the form of a pencil beam from an X-ray tube toward the object to be imaged. Sodium Iodide (NaI) and Yttrium Orthosilicate (YSO) scintillation detectors (Figure 1-2) placed around the X-ray tube then record the number of photons backscattered toward them for a particular pencil beam position. As the system scans across the target object, a real-time image is formed based on the counts recorded by each detector.

Lead collimation sleeves, positioned around the scintillation detectors prevent the detection of photons backscattered above a certain depth, called the collimation plane. Thanks to this feature, RSD can yield high quality images of features located at selected depths inside the target object.¹

Applications of backscatter Radiography by Selective Detection include, among other things, detection of land mines and Homeland Security inspections. It is, however, currently used for detection of flaws and defects, such as cracks, voids and corrosion in a wide variety of materials including aluminum, steel, concrete, carbon-carbon composites and Spray-On-Foam-

Insulation (SOFI). In particular, since 2004, six RSD systems have been used by NASA and the Lockheed Martin Space Systems Co. to detect flaws in the foam insulation on the external tank of the space shuttle prior to each launch.² Such flaws caused parts of this foam to strike the wing of the Columbia Space Shuttle in 2003 shortly after lift-off, damaging the shuttle's heat shield. RSD is also used for the detection of Foreign Object Debris (FOD).

Limits to Radiography by Selective Detection

Because RSD is based on a pencil beam X-ray source, it allows obtaining very accurate backscatter images, with sub-millimeter resolution. In order to detect small differences in contrast between features of a target object, the RSD technique needs to achieve a high count rate to reduce the statistical uncertainty associated with the measurement. However, because this technique requires a narrow pencil beam source, it is necessary to shield the majority of the photons as they exit the X-ray tube to reduce the dispersion in the pencil beam. As only a fraction of the photons produced by the X-ray tube is used, RSD systems must spend sufficient time on every pixel of the image to ensure that the statistical uncertainties are limited. Total scanning time is obviously an important factor for an imaging technique, and much of the research work accomplished by the SXI group is aimed at reducing the image acquisition time. Nucsafe, a company based in Oak Ridge, Tennessee, which is working with the University of Florida, has mobile pencil beam systems capable of imaging over a square meter per minute and portable systems capable of imaging several square meters per minute. However, these fast systems do not use collimated detectors and as a result, there is only limited depth information.

The scanning pattern for RSD is shown in Figure 1-3. The X-ray source sweeps across the target object to record the counts for one line of pixels, before going to the next line and so on until the whole area has been imaged. To scan a square foot area with a 1 mm resolution, assuming that the required illumination time per pixel is 0.1 second, the total image acquisition

time with the RSD system currently in place at the University of Florida, and constructed in 2004, would be two hours and thirty five minutes.

The two backscatter radiography systems presented in this thesis, Snapshot Aperture Backscatter Radiography (SABR) and Collimated Segmented Detector Scatter X-ray Imaging (CSD-SXI) were designed in an effort to reduce the acquisition time.

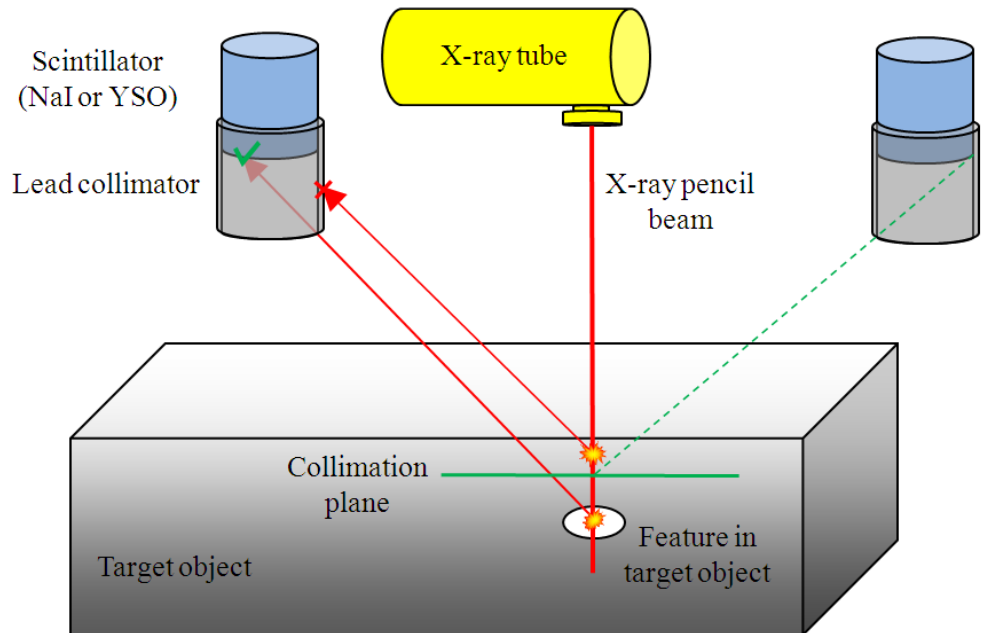


Figure 1-1. Principle of backscatter Radiography by Selective Detection.

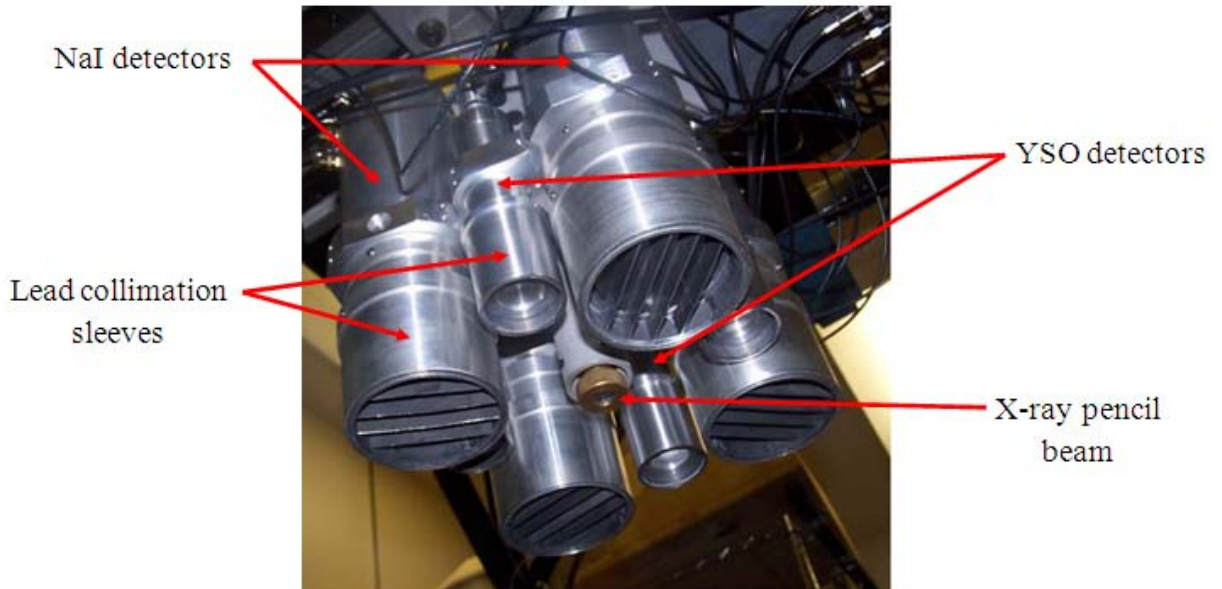


Figure 1-2. NaI and YSO detectors mounted on a pencil beam RSD system.

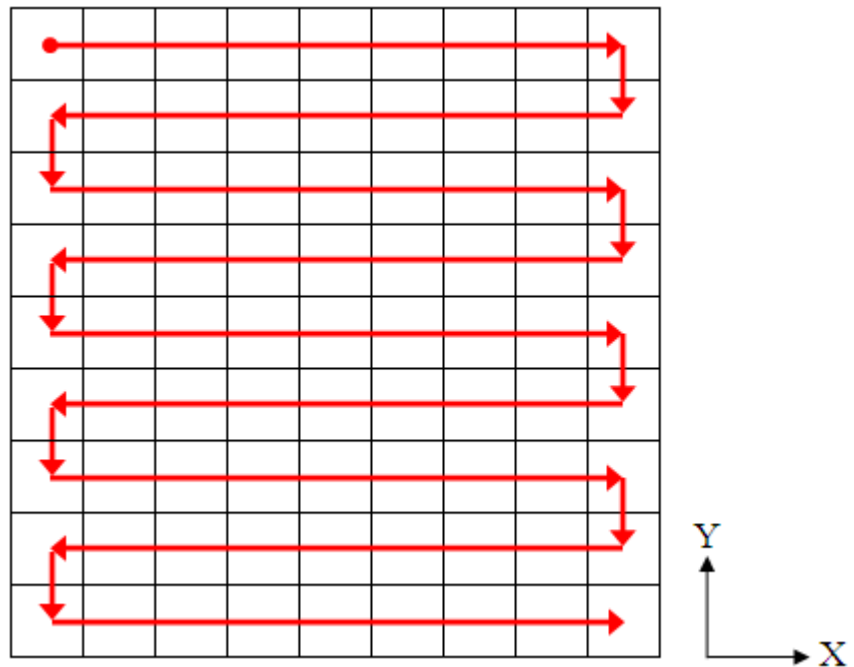


Figure 1-3. Scanning pattern of pencil beam RSD systems.

CHAPTER 2

SABR: INTRODUCTION

Snapshot Backscatter Radiography

The SABR technique is a method of X-ray backscatter imaging originally based on the Snapshot Backscatter Radiography (SBR), a technique developed by the Scatter X-Ray Imaging group at the University of Florida.³

The SBR technique obtains backscatter, single-sided images of an object without scanning, thus reducing the image acquisition time. SBR images are obtained by placing a Computed Radiography (CR) plate directly on the top the target object, which could, for example, be composed of Foreign Object Debris (FOD) placed on a background, and then exposing this target to an X-ray snapshot through the CR plate. As a result the CR plate is exposed a first time by the X-ray photons which are then scattered in the background and can be absorbed in the FOD placed under the CR plate. Depending on the scattering-to-absorption ratio of the background and the FOD objects, a given fraction of these photons reach the Computed Radiography plate. The background, or substrate, behaves like a secondary source of X-rays and the Foreign Object Debris shadows the CR plate from this source. This is why the best images were obtained with a highly scattering substrate and strongly absorbing objects.

A CR plate is a film-like plate that is made of photo-stimulable storage phosphors. As the X-rays, emitted by the X-ray generator, strike the phosphor's atoms; the electrons are excited to a higher energy level. Then a CR plate reader (in this case, a Kodak INDUSTREX ACR-2000 Digital System) scans the plate with a laser that causes the electrons to go back to their ground state. In the process, they release visible light photons that the reader collects and counts in order to compute a digital image.

However, the SBR technique often results in an overexposure of the CR plate and a very low signal-to-noise ratio because the backscatter signal is superimposed onto the transmission signal on the image. Figure 2-1 shows the photograph of a target object and the corresponding SBR image. In this case, letters of lead were placed on a nylon background to obtain the highest possible contrast as the nylon is a highly scattering material and the lead is a strong absorber. This image was taken at 50 kVp (peak kilovoltage) with a 2.85 mAs exposure, with the X-ray source placed 23 inches away from the target object.

Principle of SABR

Because of the low signal-to-noise ratio of SBR based images, the SXI group developed a new technique, called Shadow Aperture Backscatter Radiography, which is based on the SBR method but in which the backscatter signal is not superimposed onto the transmission signal.³

The principle of the SABR technique is shown in Figure 2-2. As for the SBR method, a CR plate is placed on the object that is to be imaged. However, in the case of the SABR technique, the CR plate is covered by tiles of lead to prevent it from being completely saturated by illumination photons. Instead, the illumination X-rays can only reach the CR plate and the target object through apertures between the lead tiles. These X-ray photons are then absorbed in the object or backscattered toward the parts of the CR plate that are shadowed by the lead tiles.

As a result, the contrast in the shadowed parts of the CR plate is greatly enhanced when compared to the images obtained with the SBR technique, but while the exposure of most parts of the image is good, there are some saturation (white) lines on the image corresponding to the illumination apertures between the lead tiles. Consequently, these parts of the images cannot be used to detect features directly under the CR plate. This problem can be overcome by simply acquiring one image of an object, and then by shifting the lead tiles, and by reacquiring another image to make sure that all the missing parts from the first image can be seen on the second one.

However, because the intensity received by each point of the CR plate decreases exponentially with its distance to the apertures, image reconstruction is complex and two images cannot be simply overlapped to get rid of the white lines.

The energy range used in this experiment was roughly from 0 to 100 keV, which corresponds to energies at which the Compton scattering is still relatively isotropic, as shown in Figure 2-3, whereas higher energy photons experience strongly forward peaked scattering.⁴ This range of energy allows a large proportion of X-ray photons to be backscattered toward the CR plate, while still allowing them to travel through a moderately absorbing medium, such as aluminum for instance.

Experimental Setup for SABR

The X-ray source used for SABR was a Source Ray SR 115 portable x-ray generator (Figure 2-4) which allowed maximum photon spectrum energies from 40 to 100 keV. The designation used for such spectra is e.g., 40 kVp or 100 kVp (meaning 40 or 100 keV peak). The energy spectrum of such an X-ray source usually resembles a Maxwell-Boltzmann distribution with average photon energy of about 40% the maximum energy. Figure 2-5 displays a typical medical X-ray source energy spectrum at 75 kVp with a 2.7 mm aluminum filter, with average photon energy of 39 keV. This graph does not represent real measurements done on the Source Ray X-ray generator used for the SABR experiments but is an accurate energy spectrum for a standard X-ray source.

The single shot exposure on this X-ray generator can vary between 0.15 mAs and 60 mAs, but it was possible to take several shots to obtain even higher exposures (the cooling time between two 60 mAs shots is about two minutes).

The CR plate used was a Kodak GP Digital Imaging Plate SO-170, which is about 0.6 mm thick and which is mainly composed of a layer of bariumfluorobromoisodide (BaFBr) protected

by a thin polyester coat.⁵ In the MCNP calculations detailed later in this report, the CR plate was assumed to be only made of BaFBr. The density of this type of CR plate is roughly 5.0 g/cm^3 . Although a CR plate can theoretically be scanned thousands of times if handled with extra caution, the plates used were not in perfect condition and this resulted in artifacts in some of the images.

To obtain a SABR image, the target objects, which are generally composed of various objects on a scattering substrate, is placed on a lead sheet that is laid on a steel table. Then, the CR plate is put directly on the objects that are to be imaged. Finally, an assembly of tiles of lead is placed over the CR plate. Three different assemblies of tiles were used to shade the CR plate and create the apertures to allow illumination of the objects. Each assembly consisted of 1 mm thick square tiles of lead glued next to each other on a sheet of paper with an average spacing of 1 mm between the tiles for the apertures. The square tiles of the three assemblies were about 1, 1.5 and 2 inches long (Figure 2-6).

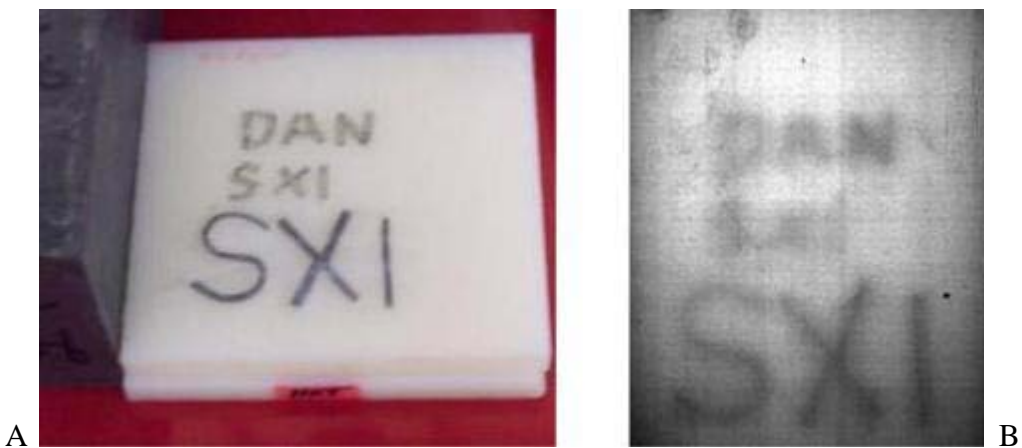


Figure 2-1. Letters of lead on a nylon substrate: A) Photograph B) SBR image at 50 kVp, 2.85 mAs and 23 inches between the X-ray source and target.

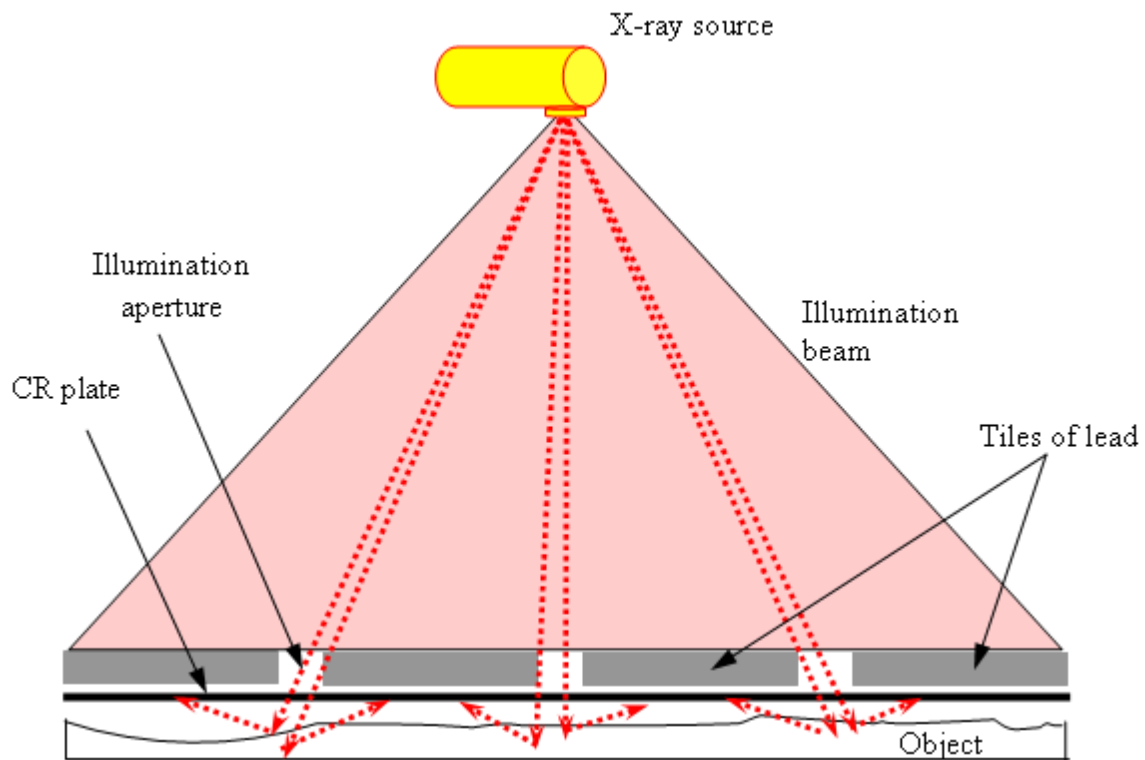


Figure 2-2. Principle of Shadow Aperture Backscatter Radiography.

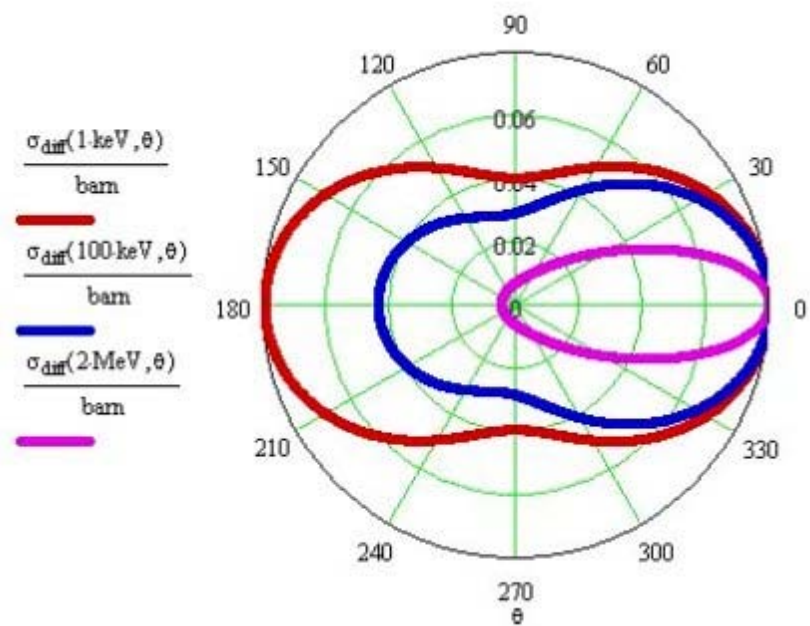


Figure 2-3. Differential scattering cross section per unit solid angle at 1 keV, 100 keV and 2 MeV.⁴



Figure 2-4. SR 115 portable X-ray generator.⁶

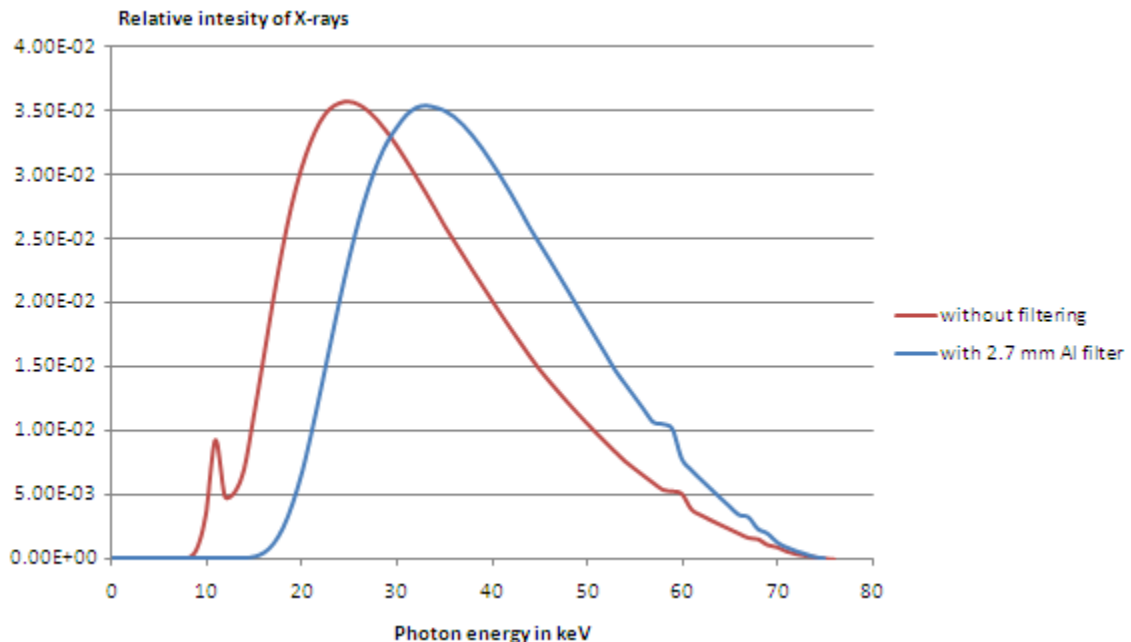


Figure 2-5. Typical energy spectrum of a medical X-ray generator at 75 kVp with and without aluminum filter.

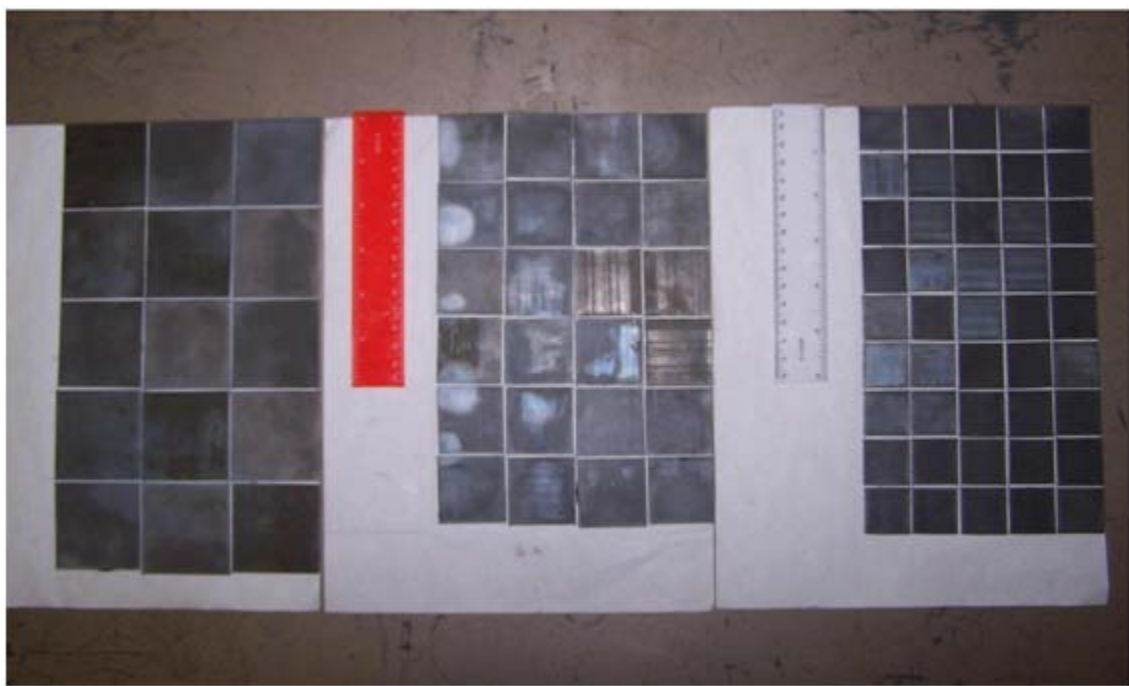


Figure 2-6. Assemblies of 1", 1.5" and 2" lead tiles.

CHAPTER 3

SABR: IMPORTANT FACTORS ON IMAGE QUALITY

Effects of the X-ray Generator Configuration

There are several factors that can affect the quality of images obtained with the SABR technique. Perhaps the most important ones are the maximum energy of the X-ray photons and the exposure. These factors can be modified directly on the SR-115 X-ray generator.

Exposure

The exposure, measured in mAs (on the SR-115, the current is fixed at 15 mA, and the exposure time varies between 0.01 and 4.0 seconds⁶), is very important for obtaining a reasonable amount of photons to avoid under or overexposure of the CR plate. This factor is also strongly linked to the distance between the X-ray source and the CR plate. Indeed, because X-ray photons are roughly emitted isotropically at the anode in the X-ray tube for energies below 100 kVp, the number of photons reaching the CR plate is proportional to $1/R^2$, where R is the distance between the source and the CR plate. For example, by increasing the distance between the X-ray source and the CR plate by a factor of two, the exposure needs to be increased by a factor of four to obtain roughly the same image.

Affirmation of this behavior is demonstrated in Figure 3-1. A number of metallic objects (a lead wedge, some steel washers and a penny shown in Figure 3-1A) were placed on a nylon substrate which is a very good scattering material. A first SABR image (Figure 3-1B) was obtained at 75 kVp with an exposure of 60 mAs and with the CR plate located 25 inches away from the X-ray source. The exposure of this image is, given the very high sensitivity of CR plates, very close to the exposure of the second image (Figure 3-1C) obtained with the SABR method at 240 mAs and with a 47 inch distance between the source and the CR plate (47 inches is the maximum possible distance between the source and the top of the table that was used), still

at 75 kVp. The exposure and voltage were chosen to obtain the best possible images. The vertical and horizontal white lines that can be seen on the two SABR images correspond to the illumination apertures.

Voltage

The effects of voltage variations are even more important. For instance, at 50 kVp, with a source-to-target distance of 25 inches, the objects on a nylon surface are only visible for exposures above 240 mAs, and with an aluminum substrate, only the white lines are visible at exposures as high as 360 mAs; the rest of the CR plate remains completely dark. This can be explained by the fact that at lower energies (below 20 keV), the dominant collision type of photons in the nylon and the aluminum is photoelectric absorption, and as a result a lower fraction of X-rays can be backscattered in the substrate through the various objects and toward the CR plate.

On the other hand, at energies greater than 80 kVp, for tiles of lead 1 mm thick, there is too much transmission through the 1 mm thick lead shadow shields and the signal-to-noise ratio is decreased because the backscatter signal is superimposed onto the transmission signal. This is because, at energies higher than 80 keV, a significant fraction of photons have a mean free path in lead on the order of 1 mm. For instance, for a photon of 30 keV, which is roughly the average energy of X-ray photons for a source voltage of 70 kVp, the mean free path in lead is about 0.03 mm⁷; so, at this energy, very few photons actually go through the lead. However, at 90 kVp, a non-negligible fraction of photons have energies higher than 80 keV for which the mean free path in lead is about 0.3 mm, which is of the same order as the thickness of the lead tiles.

MCNP calculations were performed to confirm the impact of photon energy on the SABR image contrast. MCNP is a Monte Carlo particle simulation code developed by the Los Alamos National Lab. Figure 3-2 shows the MCNP geometry used to simulate the SABR image of a steel

washer on a nylon substrate. The air is represented in purple, the lead in dark blue, the CR plate in light blue, the nylon in yellow and the steel washer in green. The source for this geometry was a circular surface source placed above the lead tiles and which emitted photons at a given energy directed downward (Because the point source for the SABR experiment was 25 inches away, and the total size of the nylon background was 6 inches, it can be safely assumed that all photons had the same direction).

Figure 3-3 shows the flux received by each point of the CR plate when the source emitted 500 million photons at 10 keV, 50 keV and 100 keV. The average relative error per pixel of the background for the simulation at 50 keV is close to 50%, whereas, on a SABR image at 75 kVp, 60 mAs and 25 inches, the average statistical uncertainty per pixel is 3%. Therefore, it can be estimated that 500 millions photons in the MCNP simulation correspond to a SABR image with an exposure of about 0.2 mAs only. However, due to the lack of sensitivity of the CR plate, SABR images taken at 0.2 mAs appear dark. The parts of the image in white have not received any photon during the MCNP calculations, each of which lasted roughly 90 minutes, and would be represented by very dark pixels on the corresponding SABR image. As explained before, the image with the best contrast is by far the one at 50 keV, which is close to the mean energy used with the SABR technique. The pixels size for each image was 0.5 mm, and each lead tile measures 2 inches. Because the circular source of the MCNP simulation did not cover the whole area, the corners are underexposed compared to the rest of the image.

Notes on MCNP Photon Source for SABR Simulations

Although, the image quality at 50 keV is better than at 10 or 100 keV, some parts of the CR plate, corresponding to white pixels were not crossed by any photon during the MCNP calculation. Moreover, the relative error of the flux for pixels that received very few photons is close to 100 %, even after hours of MCNP calculation. In fact, this is due to the very low

probability of photons going through the lead tile assembly. Indeed, the aperture holes only take less than 0.5 % of the total area of the assembly, and the mean free path of 50 keV photons in lead is about 0.1 mm, which is less than the tenth of the thickness of the lead tiles, so the probability of a photon to pass through the lead is roughly 4×10^{-5} . As a result, more than 99.5% of photons are wasted if a continuous surface source is used.

Consequently, a better source was introduced in all the other MCNP input files. The particles were then emitted over the aperture holes between the lead tiles only. Figure 3-4 shows the flux received at each point of the CR plate for the two different source types. The image shown in Figure 3-4A was created with the continuous source, with 500 million photons emitted and the calculation lasted for more than 90 minutes. The other image, shown in Figure 3-4B was made using the other source, for which only 5 million particles were emitted in less than 50 minutes (the inefficiency of the source sampling is responsible for such a small number of particles emitted per unit time).

The difference in image quality is explained by the fact that on average, the CR plate pixels received ten times more particles with the modified source than with the regular one (this can be seen on the scales). Also the largest uncertainty of flux value for a 0.5 mm wide pixel is only about 20% with the modified source. Figure 3-5 shows the proximity between the image observed experimentally with the SABR of a steel washer (Figure 3-5A), and the image created after a MCNP simulation of a SABR of the same steel washer (Figure 3-5B). This similitude validates the MCNP geometry and source models used.

Finally, it was observed that typically, variations of voltage between 60 and 80 kVp do not seem to dramatically change the contrast between the objects and the substrate they are placed on. In general, for most objects and backgrounds, 75 kVp, 60 mAs and 25 inches are settings that

offer fairly good SABR images and the contrast is rarely improved significantly by changing the energy or the voltage, as long as the image exposure is acceptable.

Effects of the Substrate

The substrate, or background, is a plate on which the target objects are placed. Its composition can greatly modify the SABR image. Three types of substrates were used and compared: a nylon substrate, an aluminum substrate and a lead substrate. The first two offered fairly good images, because their scattering-to-absorption ratios are high enough. At 30 keV, the approximate average energy of photons for voltages of about 70 kVp, the scattering-to-absorption ratio is 0.3 for the aluminum, and 3.0 for the nylon.⁷ However, the SABR images of objects placed directly on a lead substrate were very dark, except for the white lines corresponding to the apertures. This is due to the very low scattering-to-absorption ratio of lead (0.05 for 30 keV photons). Indeed, the vast majority of photons that are allowed through the apertures are absorbed in the lead substrate instead of being scattered back toward the CR plate.

In Figure 3-6, can be seen a variety of objects on a 0.5 inch thick nylon substrate and the resulting SABR image taken at 75kVp with an exposure of 60 mAs, the CR plate being 25 inches away from the X-ray source. The tiles used to obtain this image were medium sized tiles, of about 1.5 inches. All the different objects are visible on this SABR image, except the nylon washer, as could be expected, because the average mean free path of photons in that energy range in the nylon is about 4 cm, so a very small fraction of X-rays collided in the 2 mm thick nylon washer. As a result the CR plate was not shaded by this object enough to detect the nylon washer. It can be noticed that the holes in some of the washers cannot be detected, probably because of their relative position to the aperture grid (objects that are too close or too far from the aperture lines tend to appear with less contrast).

MCNP calculations confirm that on nylon or aluminum background, only a relatively strong absorbing material can be detected. Figure 3-7 shows MCNP simulations of SABR images of a steel washer (Figure 3-7A) and a nylon washer (Figure 3-7B) laid on a nylon substrate. The steel washer is clearly visible on the first image, whereas the nylon washer is invisible on the other image. These MCNP calculations also used five millions 50 keV photons.

Figure 3-8 shows a similar SABR image but this time, the various objects were placed on an aluminum substrate. The X-ray generator setup was the same: 75 kVp, 60 mAs and at 25 inches. Also, the same medium sized lead tiles were used. It can be clearly noticed that the quality of this image is not as good as the one with the nylon substrate. This is due to the low scattering-to-absorption ratio of X-rays in aluminum at this energy range compared to nylon. As a result, fewer photons are backscattered toward the CR plate and can therefore be detected. However, because most of the objects laid on the aluminum substrate are strong absorbers they still appear on the SABR image but with a much lower contrast. It becomes extremely difficult to see the hole in the large steel washer or even to see the smallest washers. However, with a profile plot, those features can be easily detected (Figure 3-9).

Contrary to more conventional X-ray backscatter imaging methods, with which the contrast between objects in aluminum and nylon can be easily detected (the nylon being a strong scattering material and the aluminum a relatively good absorber), SABR cannot detect a thin nylon washer on an aluminum plate. What appears very surprising at first can be easily explained by the fact that objects placed on the substrate are merely shading the CR plate from the photons backscattered in the substrate. Because the average mean free path for photons between 20 and 50 keV in the nylon is on the order of 4.0 cm, very few photons are absorbed in the nylon washer which does not provide sufficient shade for it to be detected on the CR plate. In fact, the SABR

technique was never able to detect scattering material with a very small absorption cross section, which reduces the field of possible applications for the SABR technique to the detection of strong absorbers, like metals.

Figure 3-10 shows another SABR image of various objects on a 1.5 mm thick lead background. The setup for this experiment was exactly the same as previously: 75 kVp, 60 mAs of exposure and a distance between the X-ray source and the CR plate of 25 inches. As can be seen in the SABR image, not a single object can be detected at all. The fact that these objects do not appear on the SABR image, is not due to an underexposure of the CR plate for this particular X-ray generator setting, because gradually increasing the exposure did not help to detect any object, and the only effect was the broadening of the white lines on the image. In fact, the impossibility to see these objects is due to the very low scattering-to-absorption ratio of photons in lead in the 10 keV to 75 keV range (about 0.05).⁷ Indeed, a large fraction of the photons which pass through the aperture grid are absorbed in the lead and very few are scattered back toward the objects, which prevent these objects from being visible.

This SABR experiment was also simulated by MCNP calculations, which gave results very close to what was observed experimentally. Figure 3-11 shows the flux received by each pixel of the CR plate after MCNP simulation of Shadow Aperture Backscatter Radiography of a steel washer on nylon, aluminum or lead substrate. The white pixels in the third image represent areas that were not crossed by any photon.

Effects of the Size of the Lead Tiles

The size of the lead tiles is also an important factor for SABR image quality. First of all, the amount of exposure should be increased with the size of the tiles because, for large lead tiles, a very small fraction of the X-ray photons that are going through the aperture holes backscatter toward the center part of the tiles. For a smaller tile size, on the other hand, a large part of the

resulting SABR image is overexposed because the surface taken by the aperture grid (white lines) is increased, and the surface taken by the shadowed areas is decreased (Figure 3-12). The overall trend is that image quality tends to be better for medium-sized or large tiles.

The effects of the size of the lead tiles observed on the SABR images are in accordance with MCNP simulations too. On Figure 3-13 can be seen the two simulated images of a steel washer on a nylon substrate, with 1 and 2 inches lead tiles. For both images, the contrast, defined as the ratio of the average flux detected over the steel washer to the average flux detected over the nylon background, is equivalent (steel-to-nylon ratio of about 0.5%). However, a much larger area of the CR plate is overexposed (red lines) with the small lead and this can lead to more hidden features in SABR images. 50 keV photons were emitted by the enhanced source for both MCNP runs.

Effect of a Gap Between the CR Plate and the Object

Another interesting and surprising factor affecting the image quality is the distance between the CR plate and the objects to be imaged. Indeed, even a small gap of a few millimeters can hurt the image quality a lot. This is shown in Figure 3-14, where the first SABR image represents metallic objects placed on a nylon substrate without any gap between the CR plate and the objects (the CR plate was placed directly on the objects), at 75 kVp, 60 mAs, and 25 inches. The second SABR image shows the same objects but with a 4 mm gap between the CR plate and the objects, the X-ray generator setup being the same (75 kVp, 60mAs and 25 inches).

It is obvious in these images that introducing even a small gap between the CR plate and the target objects dramatically reduces the image quality. Even by modifying the X-ray generator setup it was not possible to increase the contrast for the SABR image with the 4 mm gap. This implies that the SABR technique, using the configurational setups examined in this work, can only be used to detect near-surface defects or Foreign Object Debris that are very close to a

reachable thin surface. (It was possible for instance to detect large metallic objects just behind aluminum or carbon-carbon composite plates, as seen later in this report.)

The explanation for this phenomenon is shown in Figure 3-15. It is at first surprising that for the SABR technique, a small gap between the CR plate and the target object can hurt the image quality so dramatically whereas for a pencil-beam scanning backscatter imaging system, such as the RSD (Radiography by Selective Detection) system, the image quality remains good even with a large gap between the detectors and the target object. In fact, with the pencil beam scanning technique, if multiple-scattered photons are ignored, then, when the beam is over the target object, all the X-ray photons reaching the detectors were previously backscattered in the object (Figure 3-15A). On the other hand, with the SABR technique the entire background is illuminated directly or indirectly through the aperture holes. Consequently, as the gap between the CR plate and the object is increased, the solid angle with which the area of the CR plate directly over the object sees distant parts of the background is increased, and X-ray photons backscattered in another part of the background reach that area of the CR plate (Figure 3-15B). As a result, the contrast is rapidly nullified.

Once again this experimental observation was validated by a MCNP calculation for which the geometry can be seen in Figure 3-16. Figure 3-17 shows the difference between the images obtain with MCNP simulation of a SABR image of a steel washer on a nylon background with the CR plate directly laid on the object, or with a 4 mm gap. The steel washer appears much sharper, and with more contrast between the objects and the background when there is no gap between the object and the CR plate.

Effect of a Gap Between the Object and the Substrate

The last noticeable effect is caused by the introduction of a gap between the object and the substrate, with the CR plate directly on the object. Shadow Aperture Backscatter Radiography of

objects suspended with the help of threads 3.5 inches above the substrate gave images with an extremely good contrast. This phenomenon is explained by the fact that the suspended object is crossed by photons which have been backscattered from every single area of the substrate. Therefore from the point of view of both the object and the CR plate just above it, the substrate acts as a much more uniform secondary source. Moreover, the areas of the CR plate that are close to the illumination apertures are not crossed by a larger number of particles than the areas under the center of the tiles. This causes less area of the SABR image to be overexposed. In fact, suspending objects a few centimeters over the substrate allows detecting objects that could not be detected when the object was in contact with the substrate. The nylon washer could even be detected when suspended over aluminum or lead background, despite the fact that those materials are strong absorbers. Indeed, Figure 3-18 shows the SABR image of a nylon washer suspended 3.5 inches over a lead background, at 70 kVp, 60 mAs and at 25 inches, and proves that this object can be detected when suspended, whereas it could not be seen in Figure 3-6 for instance. This feature of the SABR method could have some application, for instance to help detect objects located inside of a plane, in contact with the external hull and with an aluminum background a few centimeters behind them.

A MCNP simulation of a steel washer suspended 3.5 inches over a nylon substrate also proves that the contrast of SABR images is improved when the object is suspended. The geometry of this MCNP calculation can be seen in Figure 3-19 and the comparison between the MCNP simulated SABR images of a steel washer laid or suspended 3.5 inches over the nylon substrate is shown in Figure 3-20. The background for the suspended washer (Figure 3-20B) is more uniform than in Figure 3-20A, and therefore, the steel washer is more easily detectable.

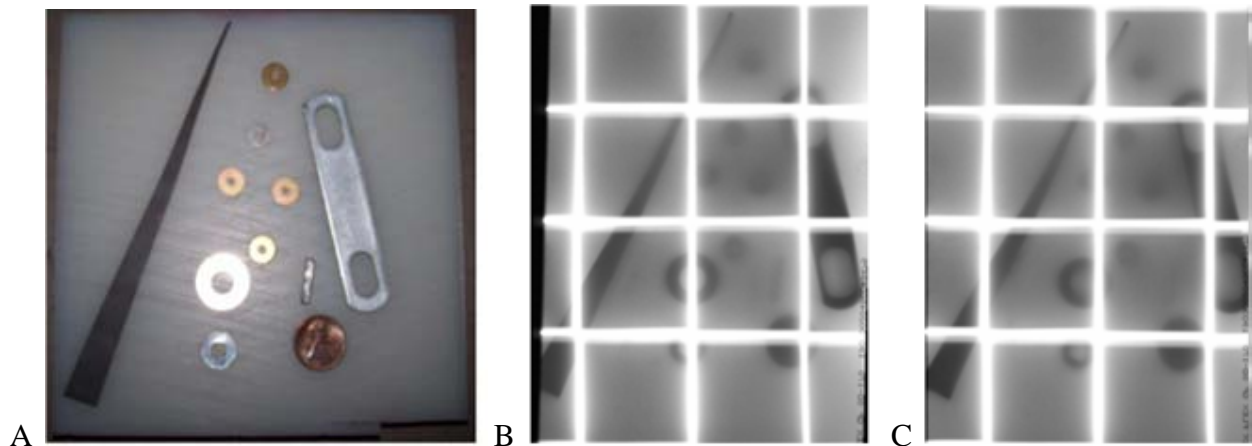


Figure 3-1. Foreign Object Debris on a nylon substrate: A) photograph, B) SABR images at 75 kVp, for 60 mAs at 25 inches, C) SABR images at 75 kVp, for 240 mAs at 47 inches.

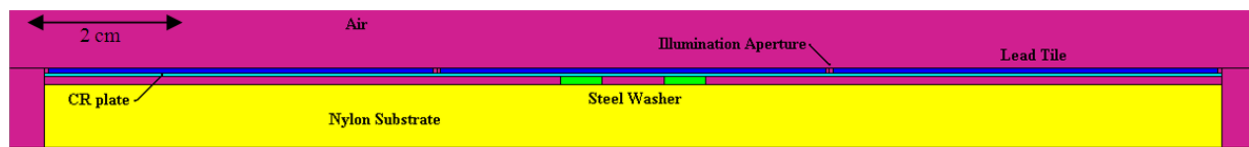


Figure 3-2. Geometry of the MCNP simulation of the Shadow Aperture Backscatter Radiography of a steel washer on a nylon substrate.

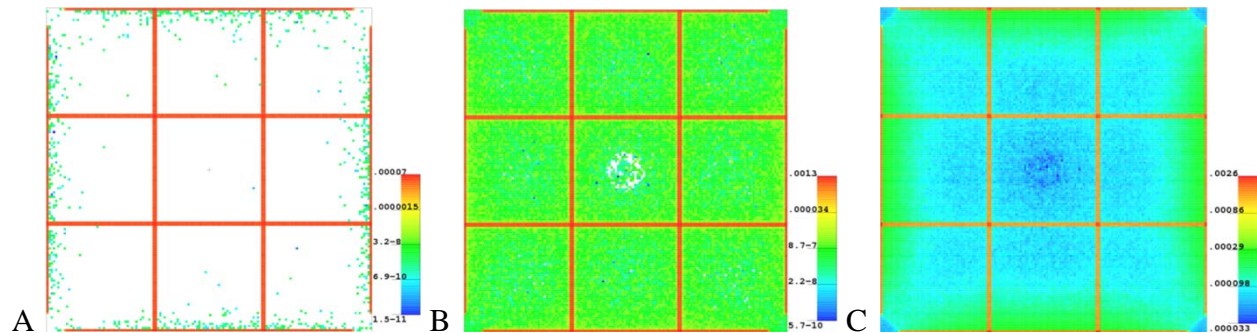


Figure 3-3. Flux of photons received after a MCNP simulation by each point of the CR plate for three photon energy: A) at 10 keV, B) at 50 keV and C) at 100 keV.

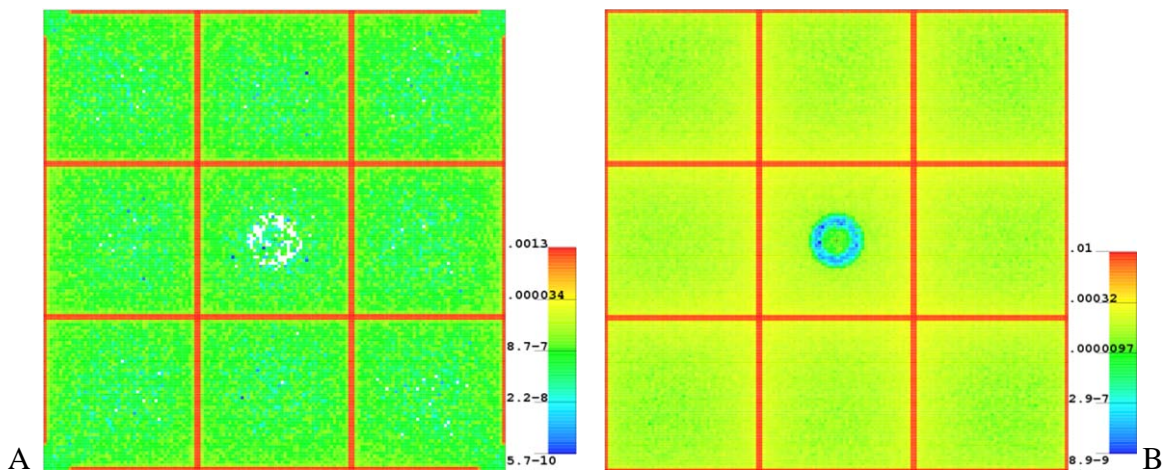


Figure 3-4. Flux of photons received after a MCNP simulation by each 0.5 pixel of the CR plate: A) with the regular source and B) with the modified, more efficient source.

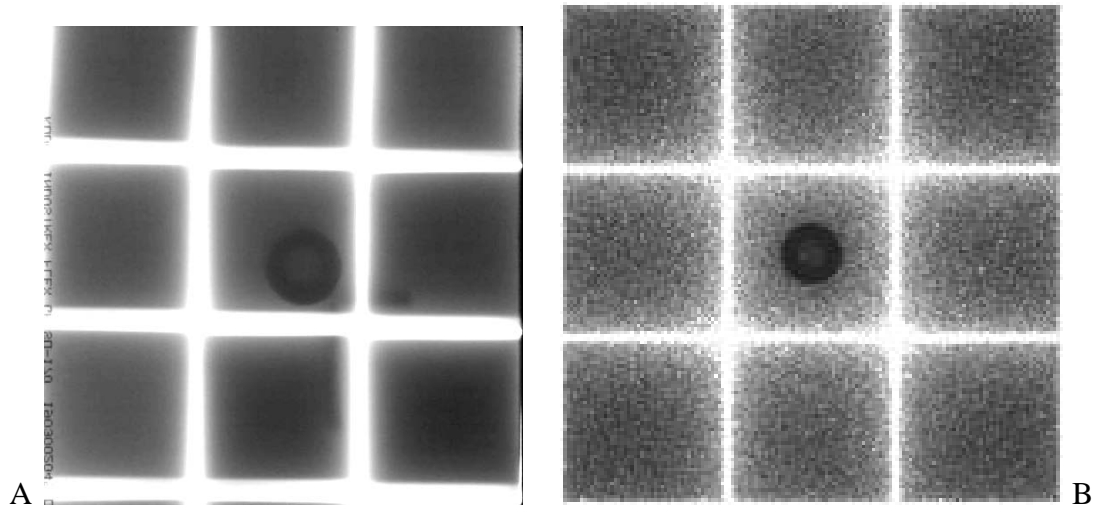


Figure 3-5. Steel Washer on nylon background: A) SABR image obtained at 75 kVp, 60mAs, at 25 inches and B) MCNP simulated SABR image based on the flux of photons detected by the CR plate.

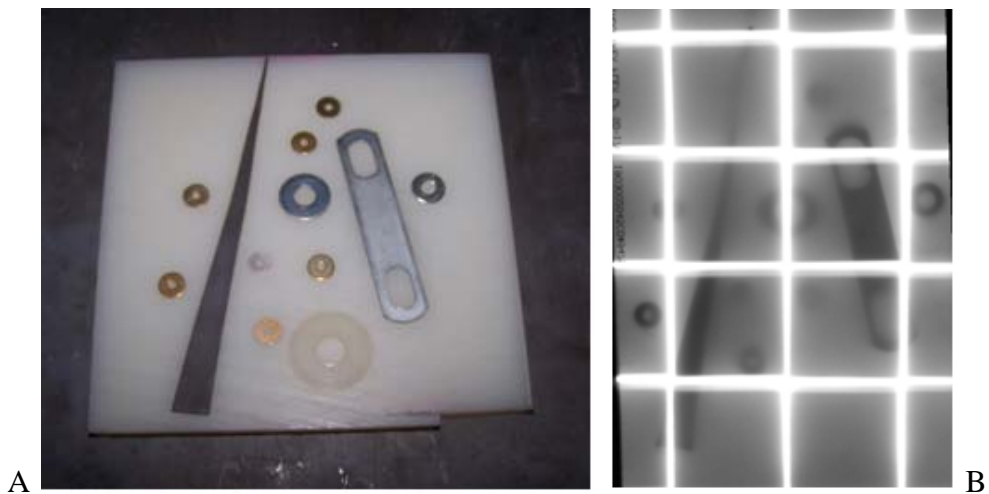


Figure 3-6. Foreign Object Debris on a nylon substrate: A) Photograph and B) SABR image obtained at 75 kVp, 60mAs, at 25 inches.

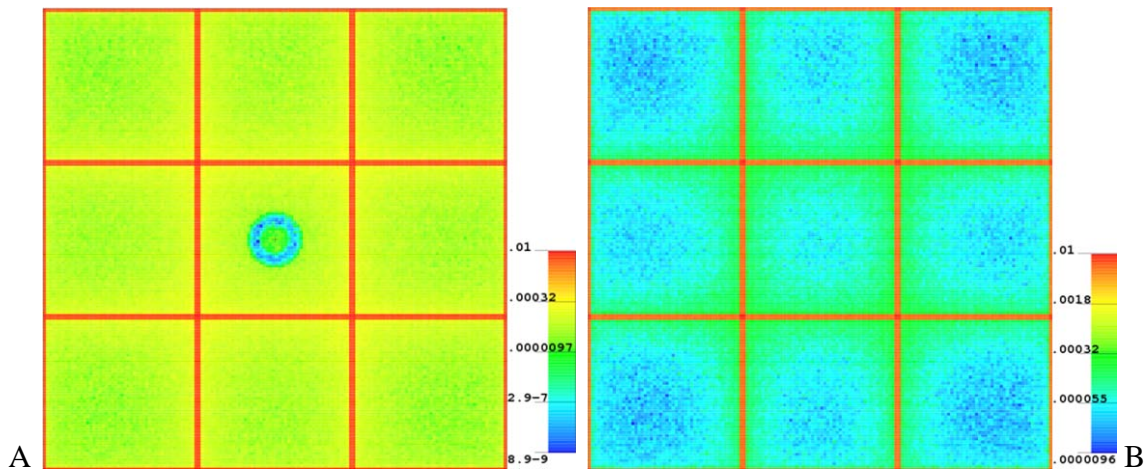


Figure 3-7. MCNP simulated SABR images of: A) a steel washer and B) a nylon washer, on a nylon substrate.

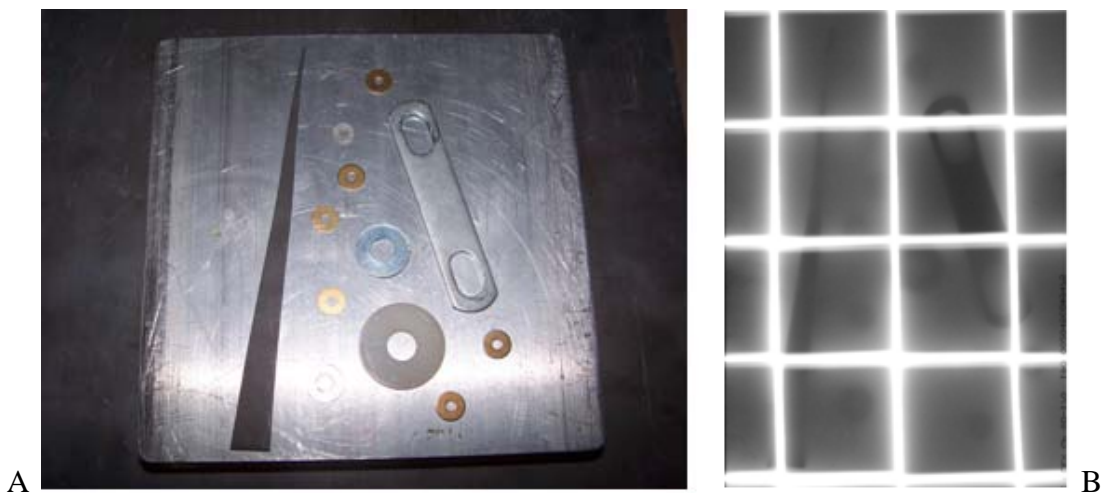


Figure 3-8. Foreign Object Debris on an aluminum substrate: A) Photograph and B) SABR image obtained at 75 kVp, 60mAs, at 25 inches.

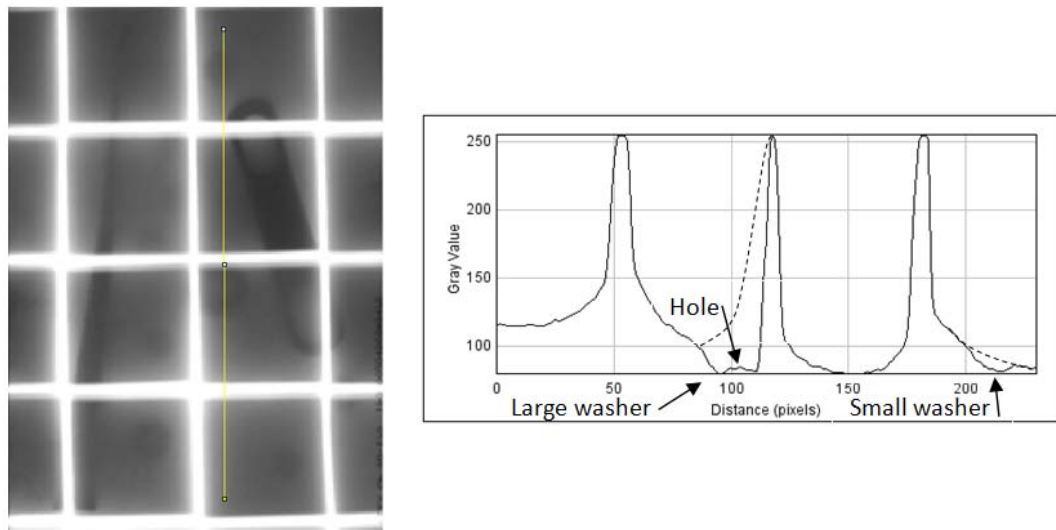


Figure 3-9. Profile plot of the previous SABR image on which can be seen two features (the hole in the large washer and a small washer).

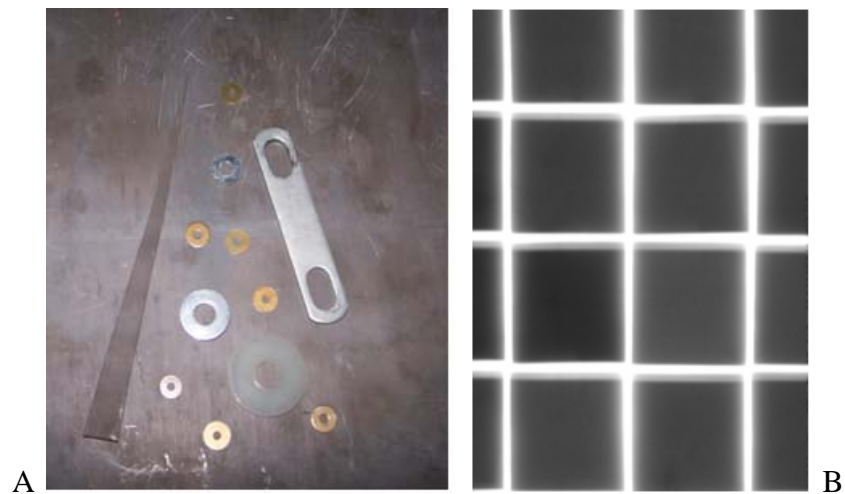


Figure 3-10. Foreign Object Debris on a lead substrate: A) Photograph and B) SABR image obtained at 75 kVp, 60mAs, at 25 inches.

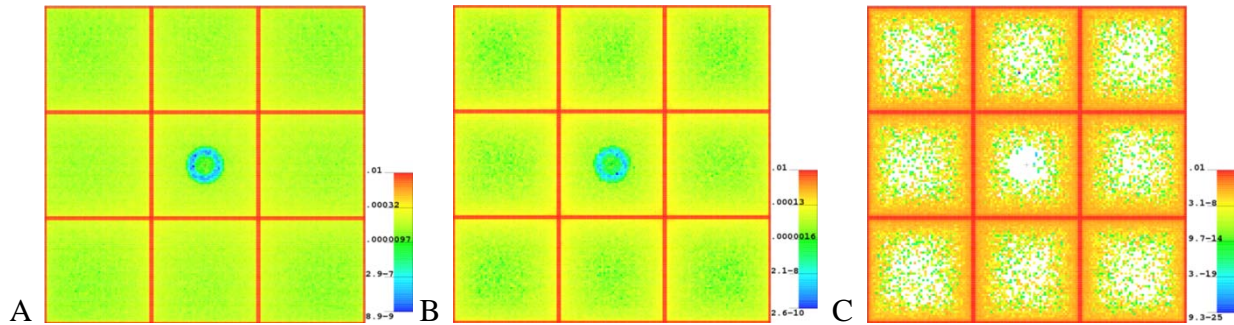


Figure 3-11. MCNP simulated SABR images of a steel washer: A) on a nylon background, B) on an aluminum background and C) on a lead background.

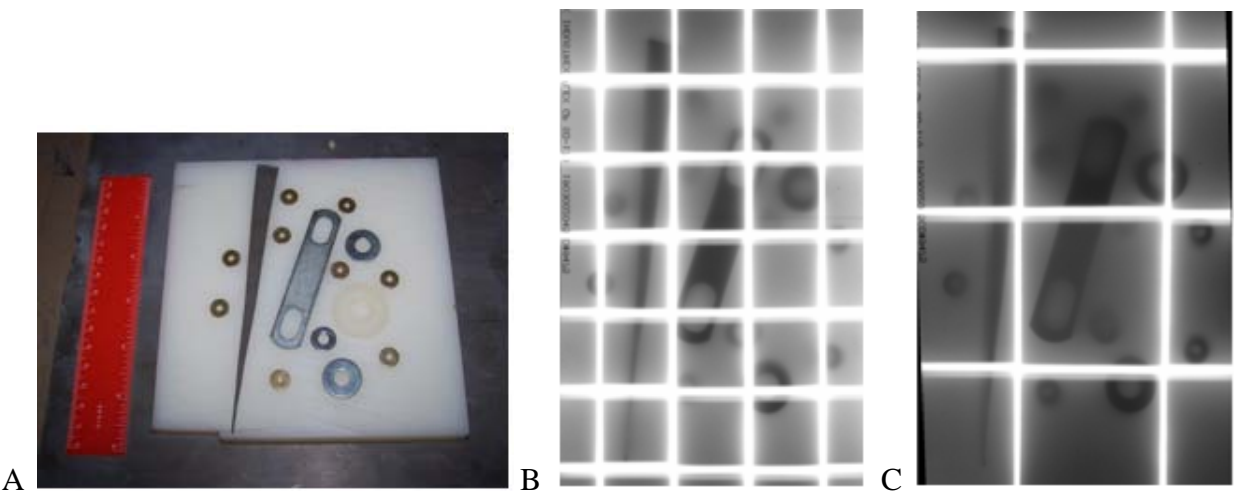


Figure 3-12. Foreign Object Debris on a nylon substrate: A) Photograph, B) SABR image with small lead tiles and C) with large lead tiles, obtained at 75 kVp, 60mAs, at 25 inches.

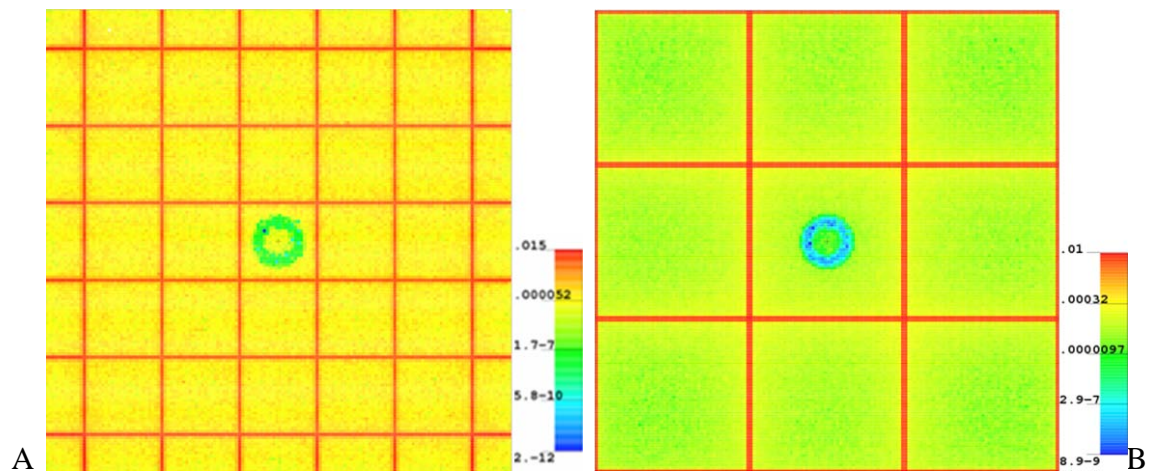


Figure 3-13. MCNP simulated SABR images of a steel washer on a nylon background: A) with 1 inch lead tiles and B) with 2 inches lead tiles.

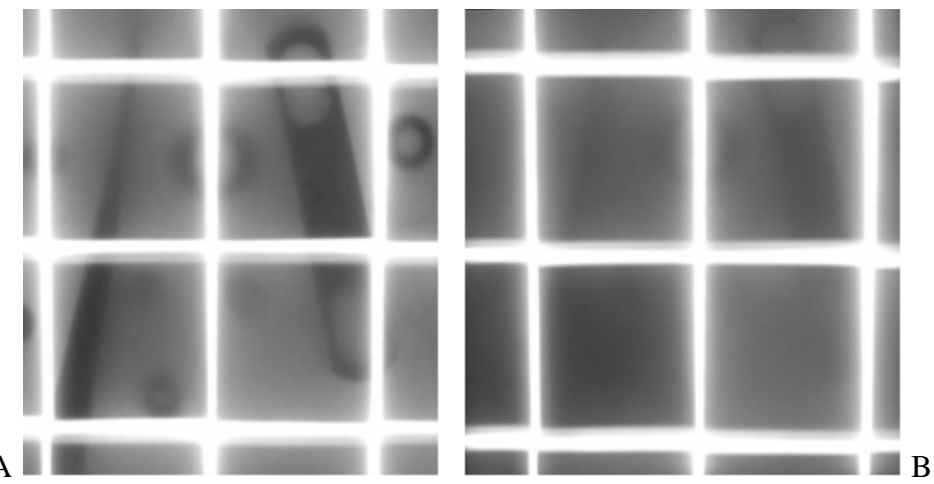


Figure 3-14. SABR images of Foreign Object Debris on a nylon background at 75 kVp, 60mAs, at 25 inches: A) with no gap between the CR plate and the objects and B) with a 4 mm gap.

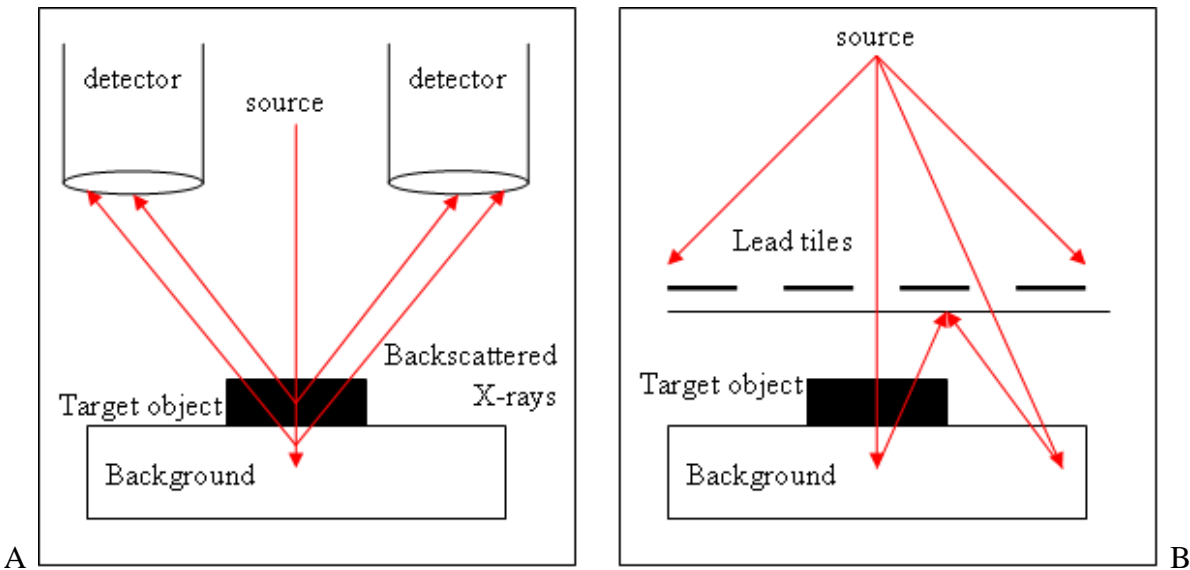


Figure 3-15. Possible paths of photons backscattered in the target object: A) for the RSD technique and B) for the SABR technique with a gap between the CR plate and the target object.

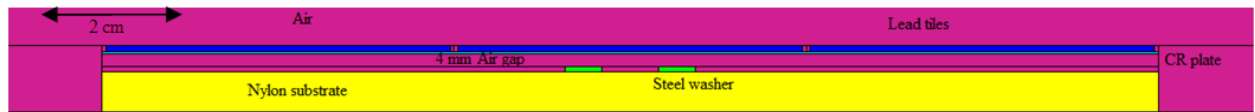


Figure 3-16. Geometry of the MCNP simulation of the Shadow Aperture Backscatter Radiography of a steel washer on a nylon substrate, with a 4 mm gap between the washer and the CR plate.

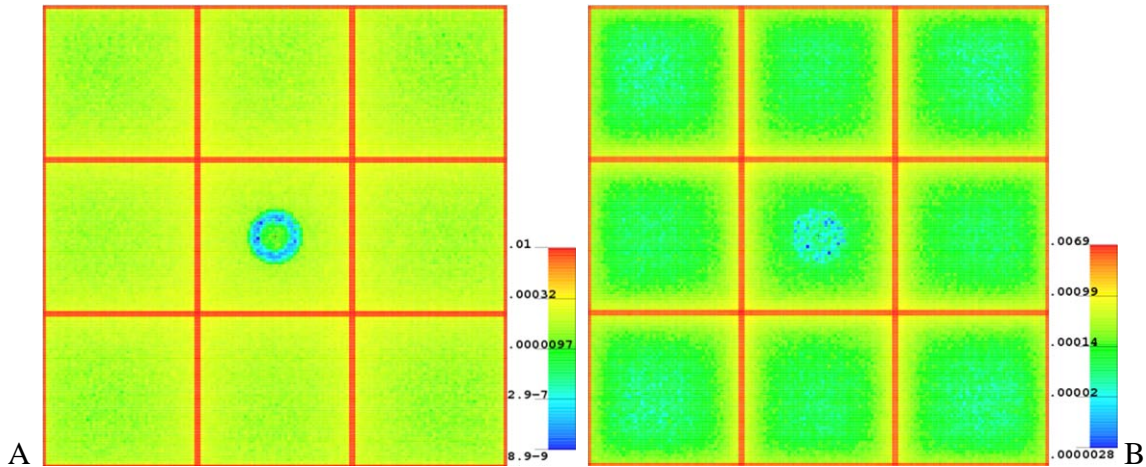


Figure 3-17. MCNP simulated SABR images of a steel washer on a nylon background: A) without a gap and B) with a 4 mm gap between the washer and the CR plate.

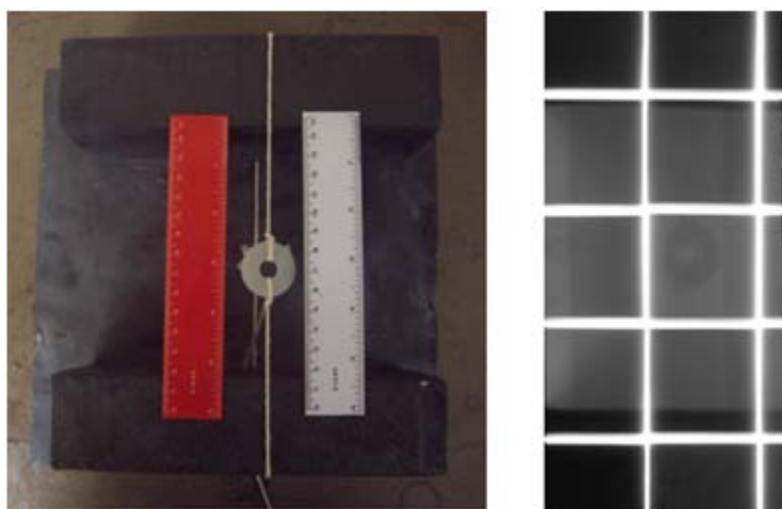


Figure 3-18. Nylon washer suspended by a thread over a lead background: A) Photograph and B) SABR image taken at 75 kVp, 60mAs, at 25 inches.

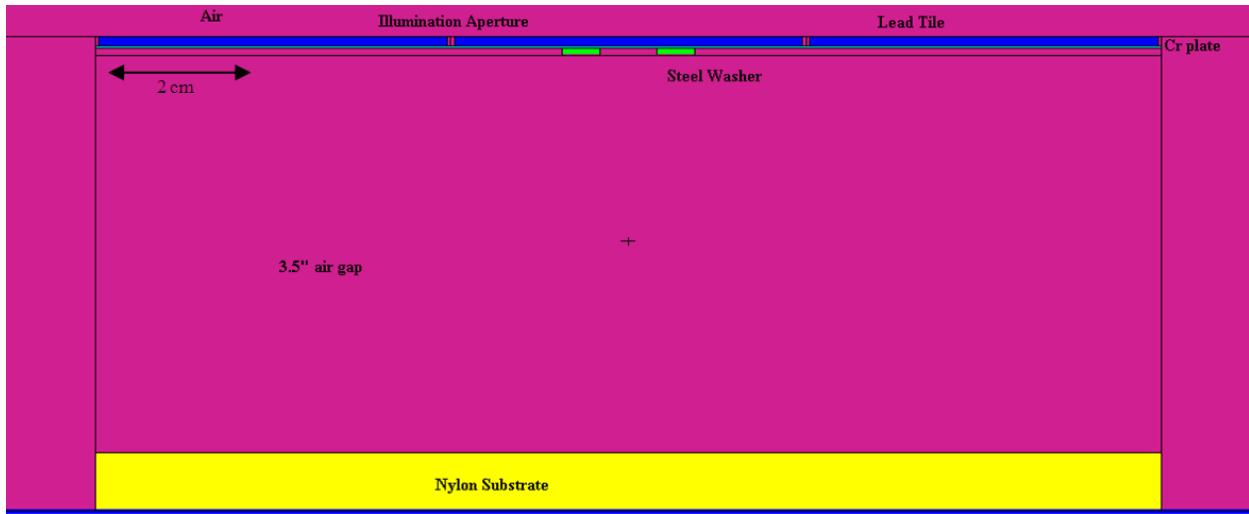


Figure 3-19. Geometry of the MCNP simulation of the Shadow Aperture Backscatter Radiography of a steel washer located 3.5 inches over a nylon substrate.

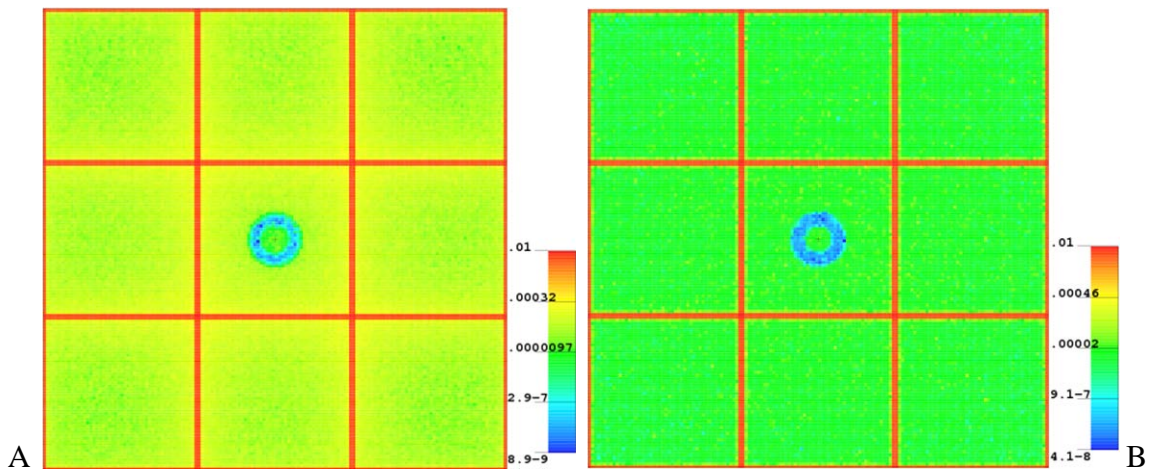


Figure 3-20. MCNP simulated SABR images of a steel washer on a nylon background: A) without a gap and B) with a 3.5 inches gap between the background and the washer.

CHAPTER 4

SABR: VARIOUS OBJECTS THAT HAVE BEEN IMAGED

Foreign Object Debris behind a thin aluminum or carbon-carbon composite plate

One of the conditions for the SABR technique to be used to detect Foreign Object Debris is the ability to take images through thin layers of common materials, such as aluminum or carbon-carbon composite. The three SABR images of lead and steel pieces on a nylon substrate, which can be seen in Figure 4-1, were all taken at 75 kVp, 60 mAs, and 25 inches. The SABR image shown in Figure 4-1A was obtained with the CR plate directly on the objects, while the SABR image in Figure 4-1B shows the same objects but with a 1 mm thick aluminum plate placed between the objects and the CR plate. Even though most of the metallic objects can still be detected, the image quality is greatly reduced when the image is taken through 1 mm of aluminum. However, this loss in image quality is not necessarily due only to x-ray attenuation in the aluminum, but also to the 1 mm gap between the CR plate and the metallic objects induced by introducing the aluminum plate. It was stated earlier in Chapter 3 that a gap between the CR plate and the objects dramatically reduces the contrast in the SABR image.

The SABR image of the same objects in Figure 4-1C was also taken through a 1 mm thick aluminum plate, but with a 5 mm stand-off distance between the objects and the aluminum plate. The CR plate was placed on the aluminum. In this image, it becomes very difficult to detect even the largest metallic objects. This is again due to the effect of a gap between the CR plate and the objects on the SABR image contrast. In order to understand the effect of introducing an aluminum plate and a stand-off distance, all three images were taken with the same experimental setup. As a result, the last two images of Figure 4-1 are both slightly underexposed. However, even by increasing the exposure for these two images, the contrast remained very low, and no other object could be detected.

Each of the three previous SABR images was simulated by MCNP calculations, with results displayed in Figure 4-2. The various metallic objects were replaced by a single steel washer. This object can be detected on the first two simulated SABR images (Figure 4-2A and Figure 4-2B) but not in the one with the 5mm gap between the object and the aluminum plate (Figure 4-2C), as was observed experimentally on the SABR images.

The same three SABR images were taken, but this time, with a 1.5 mm thick carbon-carbon composite plate, consisting of carbon fibers reinforcing a carbon matrix, instead of the aluminum plate to test for depth penetration capabilities for other materials. These SABR images can be seen in Figure 4-3. The first two (Figure 4-3A and Figure 4-3B), which are images without and with the carbon-carbon plate, were taken at 75 kVp, 60 mAs and at 25 inches. The SABR image in Figure 4-3C was taken with the carbon-carbon composite plate and a 5 mm stand-off at 75 kVp and at 25 inches, with an exposure of 90 mAs, to avoid underexposure.

Again, the image quality was greatly decreased when a carbon-carbon plate was introduced between the objects to be imaged and the CR plate. And with a 5 mm stand-off between the objects and the 1.5 mm carbon-carbon composite plate, even the largest objects were almost invisible.

SABR Images of a Spray-on-Foam Insulation Block

The next object to be imaged was a block of foam (12 inches long, 12 inches wide, 2 inches thick), with 5x5 regularly spaced holes in it, all different in diameter (0.25", 0.38", 0.5", 0.65" and 0.75") or in depth (0.125", 0.25", 0.375", 0.5" and 0.65"). This block of foam, which was placed on an aluminum plate, can be seen in Figure 4-4. Radiography by Selective Detection is able to detect flaws in this kind spray-on-foam insulation that covers the Space Shuttle external tank.² As stated before, flaws inside the foam were responsible for parts of the external

tank's insulation striking the Colombia's heat shield in the 2003 accident. Detecting flaws in the foam could help prevent such an accident from happening again.

At first, the 5 holes with the largest diameter (0.75 inches) were imaged with the SABR technique. However, contrary to what can be obtained with the Radiography by Selective Detection, the holes are invisible on the SABR image. This can be seen in Figure 4-5. This SABR image was taken at 70 kVp, 60 mAs, and 25 inches with the large tiles (2 inches). Different energy levels and exposures were tried, but the holes could never be detected in the SABR images.

In order to detect those holes, a dime (cupronickel, 18 mm in diameter) was placed in each of them. This is shown in Figure 4-6. The SABR image was taken at 70 kVp, 60 mAs, and 25 inches.

Only the coins placed in the two shallowest holes were clearly visible. This can again be explained by the dramatic loss of contrast in the SABR images when a gap between the objects and the CR plate is introduced. Because a dime is about 1.35 mm thick, the true gap between the CR plate and the last clearly visible dime measures only roughly 0.5 mm. A surface plot shows that the third dime is also visible with some image processing as shown in Figure 4-7. However, it is very unlikely that this third coin would have been detected if the operator did not know where to look. Because of the very low density of this foam, it is likely that the image contrast would be the same if the coins were introduced inside of the foam at the equivalent depths instead of just being placed in holes.

SABR Images of a Corroded Piece of Aluminum

A small, extremely corroded plate of aluminum, shown in Figure 4-8A, was also imaged with the SABR technique. The ability to see corrosion with an X-ray backscatter technique can be used for instance during the maintenance of airplanes to check the general state of the inside

of the plane, without the need of tearing it apart. The SABR image on Figure 4-8B was taken at 70 kVp, 120 mAs, at 25 inches. The exposure was increased compared to most of the previous scans because almost the entire nylon substrate was covered by the 1 mm thick corroded aluminum plate which has a high absorption cross-section. Even by increasing the exposure, the image quality remained very poor, and some of the holes could not even be detected. Also the corrosion is invisible on this SABR image.

A similar SABR image was taken, with the aluminum plate suspended between two 5 cm thick blocks of lead, about 3.5 inches above the nylon substrate, as shown in Figure 4-9A. The corresponding SABR image (Figure 4-9B) was also taken at 70 kVp, 120 mAs and 25 inches. As shown earlier, it is not surprising to observe that the image quality was greatly improved compared to when the corroded part of aluminum was laid on the nylon substrate.

For this setup, lead and aluminum can also be used for the background, with no noticeable loss in relative contrast. This was surprising because much brighter images had been expected for the nylon background than for the lead background. Also, despite the relatively good quality of this SABR image, the corrosion itself could not be detected, mainly because the contrast could not be improved enough for it to be visible.

Another SABR image of this corroded aluminum part was taken at 75 kVp, 120 mAs and at 25 inches, through a 1 mm thick aluminum plate. This image, along with the experimental setup can be seen in Figure 4-10. As mentioned earlier, the introduction of an aluminum plate decreased the image quality by a large factor.

However, some of the holes in the corroded aluminum plate are still slightly visible with the help of some image enhancement, as can be seen in Figure 4-11. The corrosion can obviously not be detected through the aluminum plate.

Other Objects that have been Imaged with the SABR Technique

SABR images have been taken of many different objects, including metallic objects inside a block of foam, bones covered by tissue simulant material, objects made of plastic (a screwdriver for example) and other highly scattering materials. None of them showed a reasonable image of the objects, mainly because of the inability of the SABR technique to detect materials in which the mean free path of X-ray photons is too long, and because this technique, using the configurational setups examined in this work, can only image flat, near surface objects, due to the dramatic loss in image quality when the CR plate is not directly in contact with the objects.

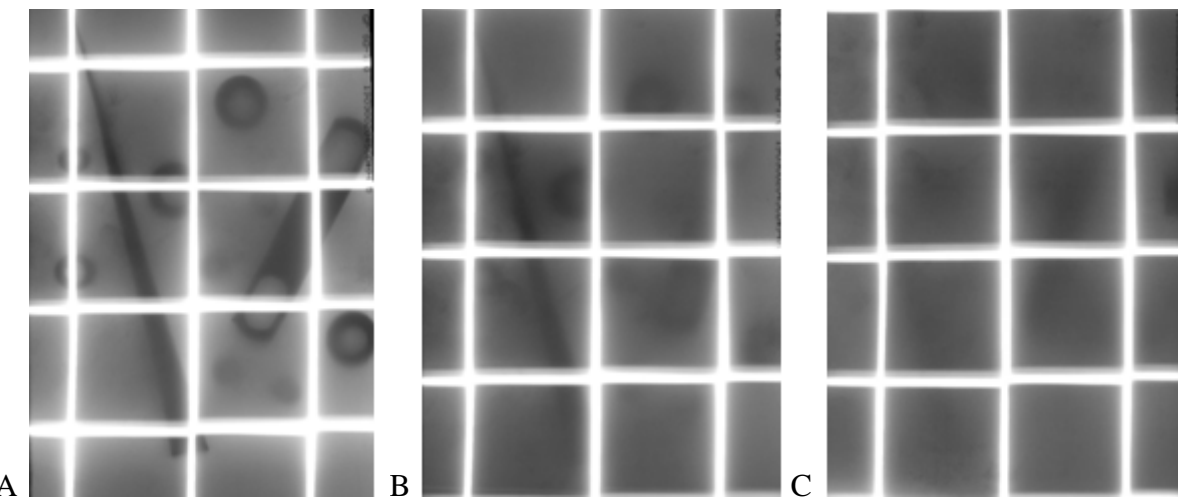


Figure 4-1. SABR of Foreign Object Debris on a nylon background taken at 75 kVp, 60 mAs, 25 inches: A) without an aluminum plate, B) with a 1 mm thick aluminum plate between the CR plate and the objects and C) with the 1 mm thick aluminum plate with a 5 mm stand-off distance.

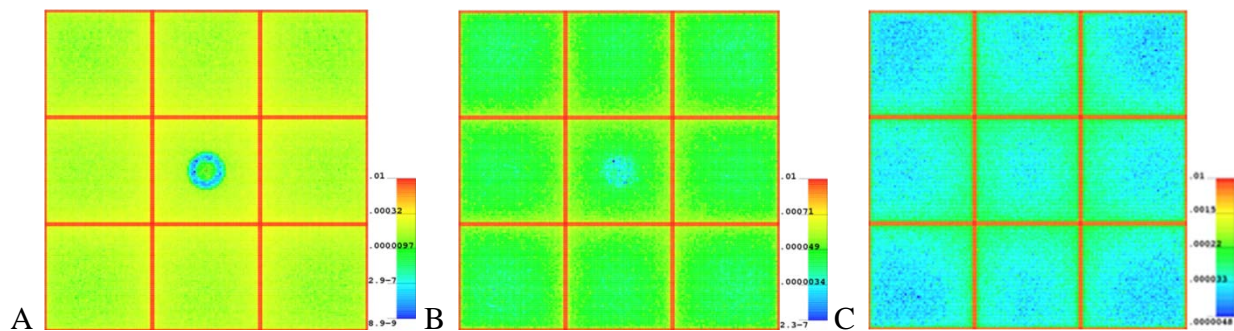


Figure 4-2. MCNP simulated SABR images of a steel washer on a nylon background: A) without an aluminum plate, B) with a 1 mm thick aluminum plate between the CR plate and the washer and C) with the 1 mm thick aluminum plate with a 5 mm stand-off.

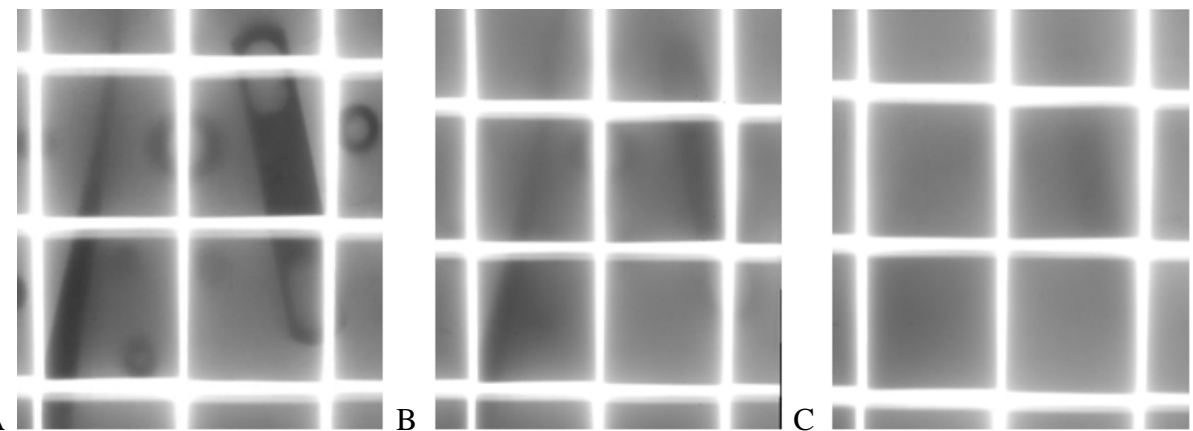


Figure 4-3. SABR of Foreign Object Debris on a nylon background taken at 75 kVp, 60 mAs, 25 inches: A) without a carbon-carbon plate, B) with a 1.5 mm thick carbon-carbon plate between the CR plate and the objects and C) with the 1.5 mm thick carbon-carbon plate with a 5 mm stand-off (taken at 90 mAs).

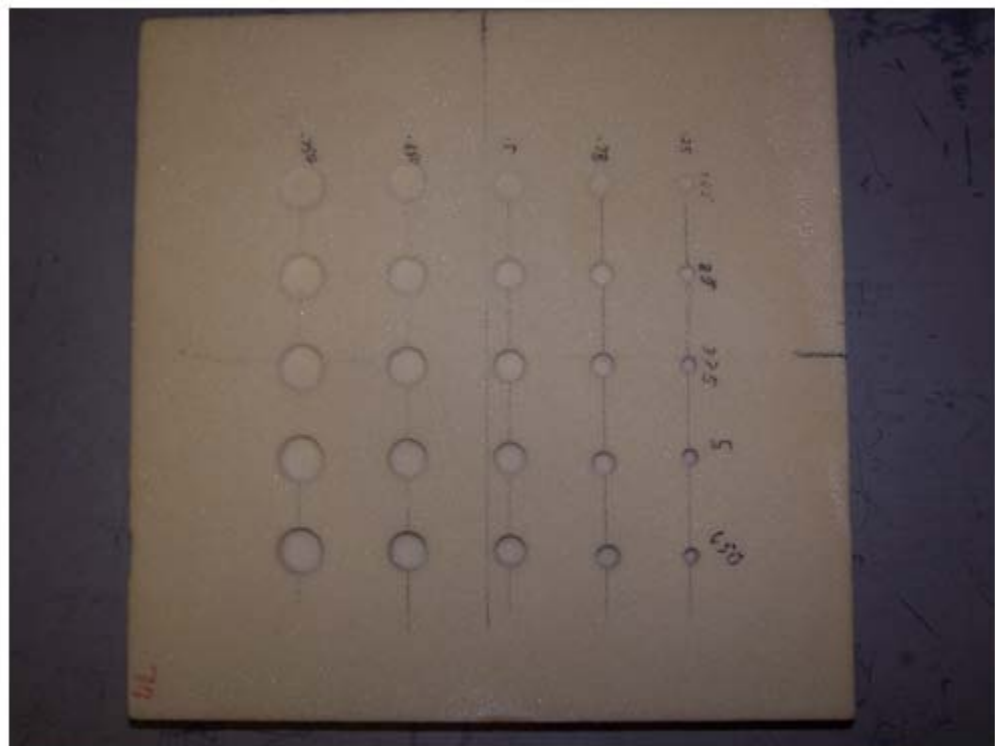


Figure 4-4. Block of spray-on-foam insulation.

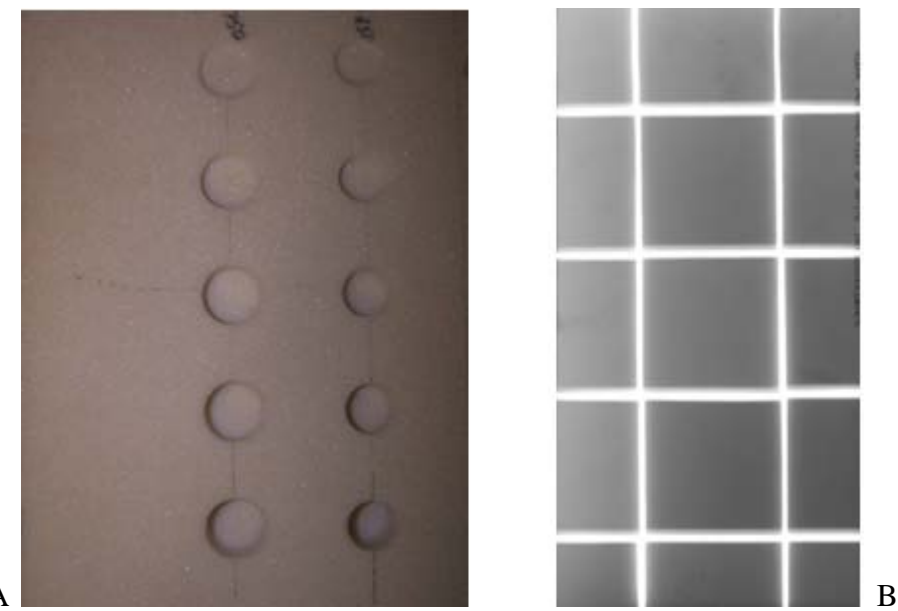


Figure 4-5. Five holes, 0.75 inch in diameter and of different depth in a spray-on-foam block: A) photograph and B) SABR image at 70 kVp, 60 mAs, and 25 inches.

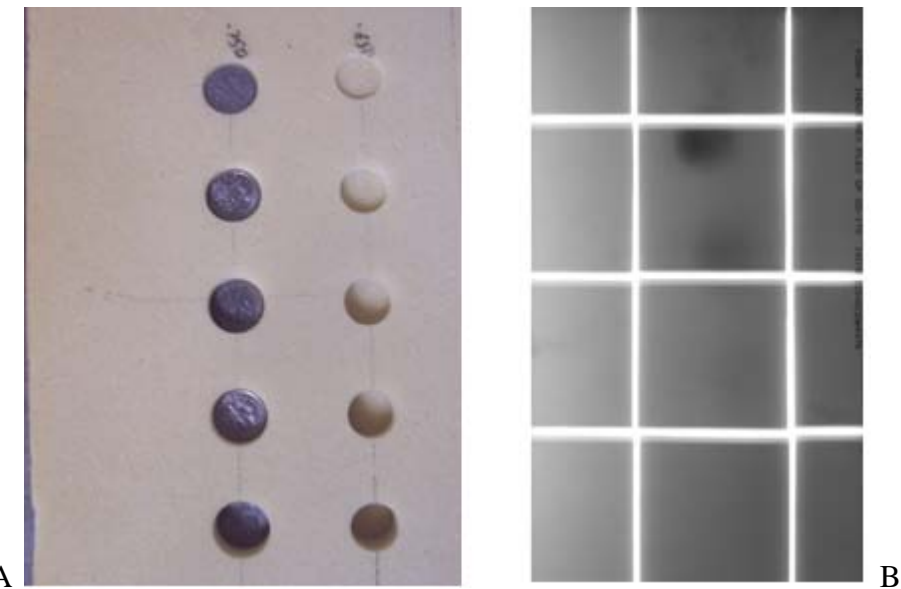


Figure 4-6. Five dimes placed in holes drilled in foam, 0.75 inch in diameter and of different depth: A) photograph and B) SABR image at 70 kVp, 60 mAs, and 25 inches.

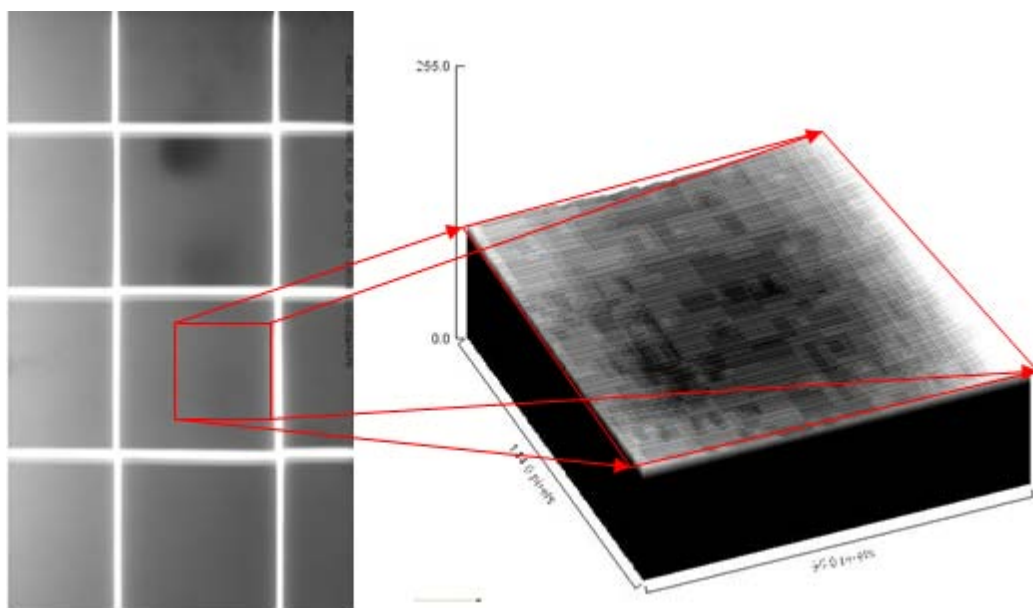


Figure 4-7. Zoom of the area of the previous SABR image that contained the third coin.

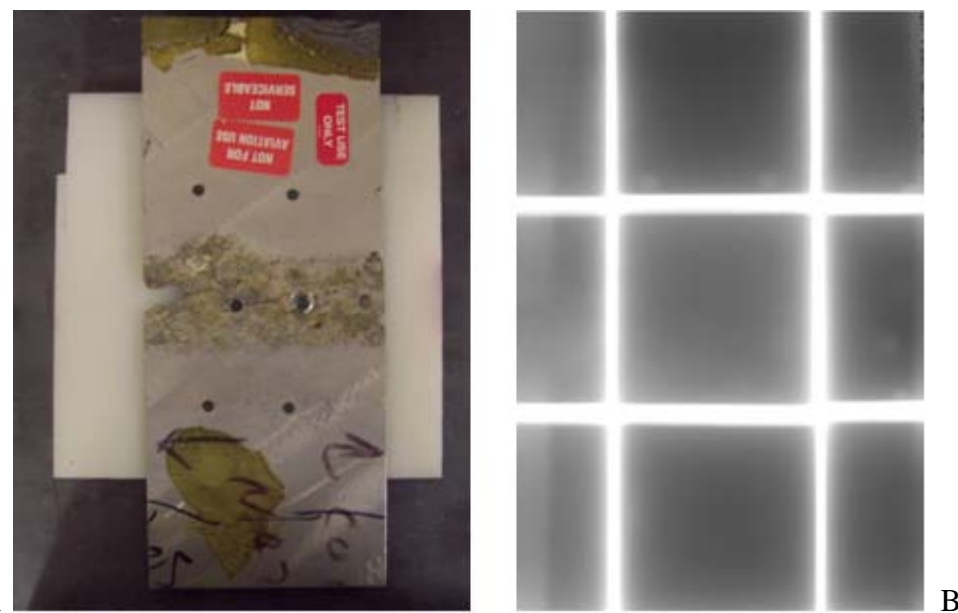


Figure 4-8. Corroded aluminum plate on a nylon background: A) photograph and B) SABR image at 70 kVp, 120 mAs, and 25 inches.



Figure 4-9. Corroded aluminum plate suspended 3.5 inches over a nylon background: A) photograph and B) SABR image at 70 kVp, 120 mAs, and 25 inches.

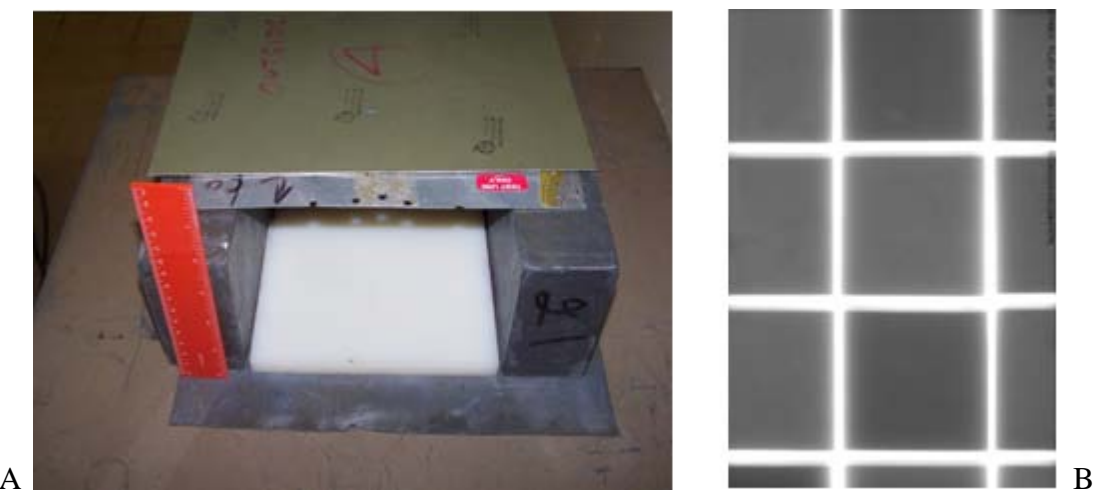


Figure 4-10. Corroded aluminum plate covered by a 1mm thick aluminum plate and suspended 3.5 inches over a nylon background: A) photograph and B) SABR image at 70 kVp, 120 mAs, and 25 inches.

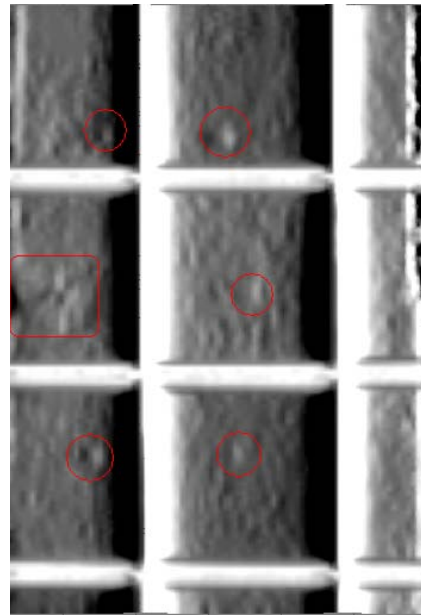


Figure 4-11. Image enhancement of the previous SABR image with features surrounded in red.

CHAPTER 5

SABR: CONCLUSIONS

The Shadow Aperture Backscatter Radiography technique is an X-ray backscatter imaging technique that is based on a snapshot acquisition method instead of the scanning acquisition method which is used for X-ray backscatter imaging. It uses assemblies of lead tiles to block the transmission signal. This prevents overexposure of the CR plate as the X-ray photons cross it to reach the target objects. By limiting the superimposition of irradiation photons on the backscatter signal, the signal-to-noise ratio is dramatically improved compared to the SBR technique. The snapshot mode of acquisition allows the operator to obtain images much faster than with systems that use scanning to acquire images (two images can be obtained in a couple of minutes with the SABR technique while the acquisition time with the RSD system currently in use at UF would be of the order of hours). But on the other hand, the image quality is not nearly as good, and fewer objects can be detected in a SABR image. Also, because the areas just under the apertures, between the tiles, are overexposed (lines about 1 mm wide), small objects can be completely hidden on the image and therefore, at least two images of a given target need to be taken in order to be sure to see all the areas in examined target.

The SABR technique offers fairly accurate X-ray backscatter images of near surface highly absorbing objects (metallic objects for instance) that are placed on a substrate made of a good scattering material such as nylon. Images acquired on more absorbing substrates, such as aluminum, can be good too despite a loss in contrast. However, it was not possible to detect objects made of highly scattering material. For example, a nylon washer on an aluminum substrate remained invisible in the SABR images when a steel washer would have appeared, and this was true no matter what X-ray energy level was used. Also, introducing a small gap between the CR plate and the objects reduces the image contrast, and gaps as small as 5 mm can prevent

any object from being detected. However, a gap between the object and the background can greatly increase the SABR image quality, to the point where objects that did not appear when laid directly on the substrate were very clear in the image when suspended a few inches over the background.

Some large metallic objects could also be seen through a plate of carbon-carbon composite or aluminum of about 1 mm in thickness which was placed directly over them. However, in this case the image quality was greatly decreased, and most of the smallest objects (less than 1 cm in size) were invisible. When a stand-off was introduced between the plate and the objects, nothing could be seen in the SABR image because of the gap between the CR plate and the objects. This problem reduces the field of possible applications of the SABR technique because in most cases, the objects that need to be detected are not directly in contact with an external surface. A lead or tungsten collimation grid placed between the target and the CR plate could prevent the averaging of contrast.

CHAPTER 6

CSD-SXI: INTRODUCTION

Computed Image Backscatter Radiography

Computed Image Backscatter Radiography (CIBR) is another X-ray backscatter imaging technique developed by the SXI group. It employs a fan beam source and rotational motion rather than a pencil beam source and rastering motion; it uses the same collimated scintillation detectors as RSD. It was originally designed to acquire X-ray backscatter images faster than RSD. This is because a larger fraction of the X-ray photons produced in the tube is used to obtain the image, the count rate is higher than with RSD, and therefore a scan of the same object and with the same statistical uncertainty tolerance is faster with the CIBR technique. Computed Image Backscatter Radiography requires scanning across the target objects at different angles with relatively small increments in order to obtain acceptable images, and it also needs image reconstruction, much like Computed Radiography.⁸ However, further research is required to improve resolution and reduce reconstruction artifacts through algorithm improvement. Figure 6-1 shows a comparison between the RSD and CIBR images of letters of lead on nylon. Some artifacts are visible on Figure 6-1B.

Backscatter Radiography using an Uncollimated Segmented Detector

The possibility of adding a linear pixelated detector, parallel to the fan beam source, to the CIBR technique in order to acquire more information on the target object was considered. This case, with geometry shown in Figure 6-2, was simulated using MCNP. In this simulation, a lead strip (6.0 cm x 2.0 cm x 0.1 cm) is fitted in a block of nylon, which is a highly scattering material contrary to lead which is a strong absorber. A 1 mm wide and 6 cm long fan beam normal to the X-axis illuminates the strip of lead and the nylon around it. A linear Gadolinium Orthosilicate (GSO) array detector (4.0 cm x 1.5 cm x 0.1 cm) is placed 3.0 cm above the surface of the

object, and starts 1.5 cm away from the fan beam. A flux mesh tally records the flux averaged over the pixelated detector. The dots seen in Figure 6-2 represent the collision sites of the X-ray photons in the matter, their colors varying continuously from red corresponding to the highest energy particles prior to collision (in this case, 60.6 keV) to blue corresponding to the lowest energy (6.3 keV). In order to accelerate the MCNP simulation, a DXTRAN sphere (not shown in Figure 6-2) was included in the MCNP input in such a manner that it encircled the entire segmented detector.⁹

The source of X-ray photons for this simulation was located 3 cm above the surface of the target object because a non-negligible flux was detected by the upper part of the detector when the source was higher due to scattering in air toward the detector. In practice, the source would need to be placed at a 20 cm distance to obtain a wide fan beam but the source scattering in air problem could be solved by ensuring that the top of the detector is shielded. The voltage used for this simulation was 65 kVp, meaning that the X-ray spectrum ranged from 0 to 65 keV. The energy distribution of the X-ray source at 65 kVp, generated by the program “XRSPEC” from the SXI group is shown in Figure 6-3. The hump around 10 keV is due to the L series characteristic X-rays for tungsten.¹⁰

The flux of X-ray photons measured by the mesh tally in the MCNP simulation was then compared with that obtained for the exact same geometry (4.0 cm x 1.5 cm x 0.1 cm GSO array detector, 6.0 cm x 2.0 cm x 0.1 cm lead strip on nylon) but with a pencil beam source. This MCNP simulation geometry can be seen in Figure 6-4.

As for the previous case, one measure of the flux for every 1 mm pixel (in the y-direction) was taken over the volume of the detector. Instead of having to do multiple simulations for each value (forty 1.0 mm pixels), the source was defined as 40 circular sources, 1.0 mm in diameter

placed on a line and 40 different flux tallies were obtained with the SCD option using FU cards.⁹

This association of data cards allowed the tally corresponding to each region of the detector to count only the particles coming from the corresponding source. As a result, there is no interaction between the different parts of the image. Figure 6-5 shows the averaged, normalized flux in the uncollimated linear array detector with a pencil beam and a fan beam X-ray source with the associated relative error.

It is clear in Figure 6-5 that the averaged flux in the detectors in the case of the pencil beam shows a strong contrast between when the pencil beam is above the nylon or the lead, because of the fact that lead is a highly absorbing material (which results in a low count rate of backscattered X-rays) and that nylon is a highly scattering material (which results in a high count rate). However, in the case of the fan beam source with an uncollimated pixelated detector, the flux shows very little difference between pixels located over the nylon and those over the lead. This phenomenon can be simply explained by the fact that each pixel can detect photons backscattered toward any direction and not exclusively those coming directly from below. Consequently, each pixel of the detector sees photons backscattered in both the lead and the nylon as can be seen in Figure 6-6, and as a result, the contrast is averaged out and greatly reduced. The exact same effect was observed in the case of the Snapshot Aperture Backscatter Radiography (SABR), a backscatter X-ray imaging technique based on a snapshot illumination, and which offers very poor contrast when there is a stand-off between the target object and the detector (a CR plate in the case of SABR experiments).

Very little information can be obtained from the flux measured for the fan beam case in Figure 6-5 when compared to the flux for the pencil beam, and it does not seem that a fan beam

associated with an uncollimated pixelated detector could really be of any use in backscatter radiography.

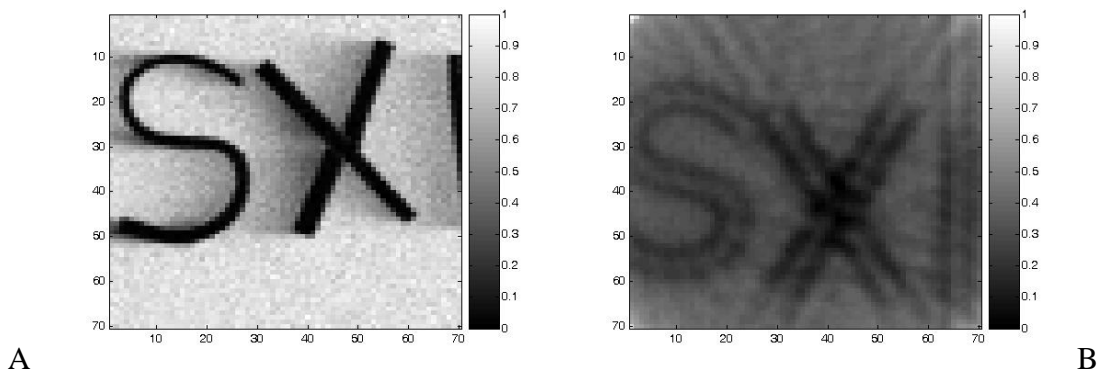


Figure 6-1. Backscatter radiography images with a 1 mm resolution of letters of lead on nylon:
A) with the RSD technique with 1 mm pixels and B) with the CIBR technique with 10 degrees rotational increments and 1 mm radial increments.

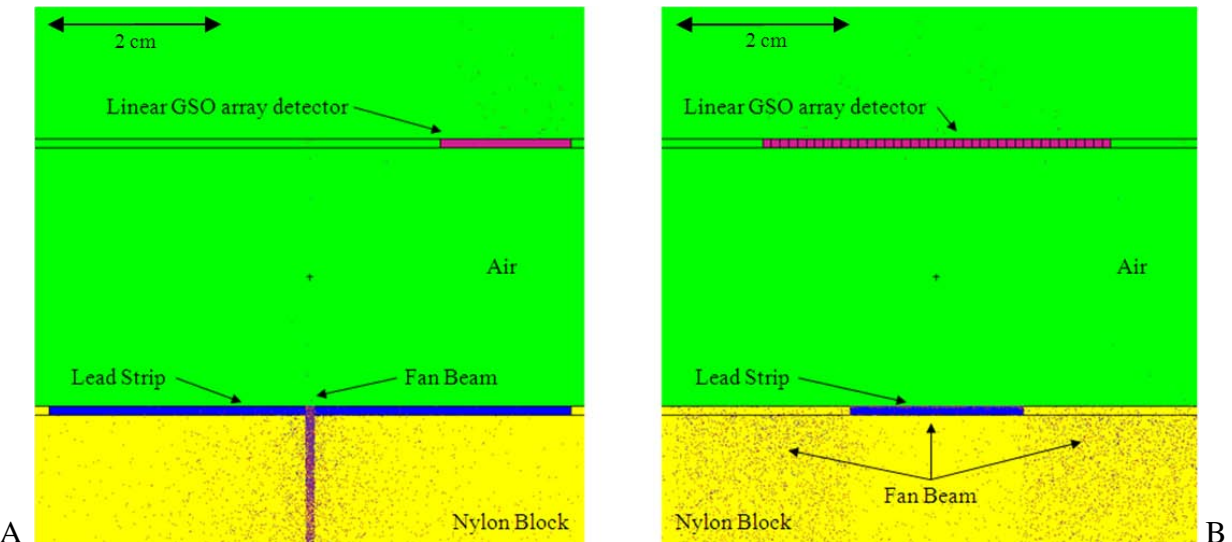


Figure 6-2. Geometry of the MCNP simulation of the backscatter radiography of a lead strip on a nylon background using an uncollimated segmented detector: A) view of the XZ-plane and B) view of the YZ-plane.

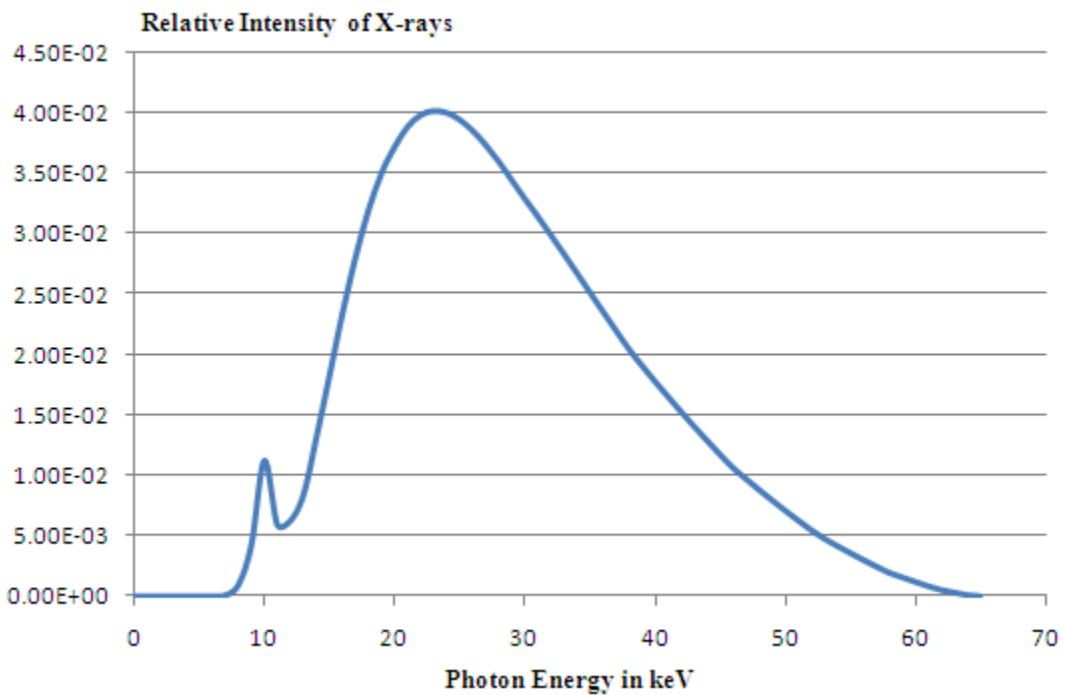


Figure 6-3. Energy spectrum of the X-ray source at 65 kVp.

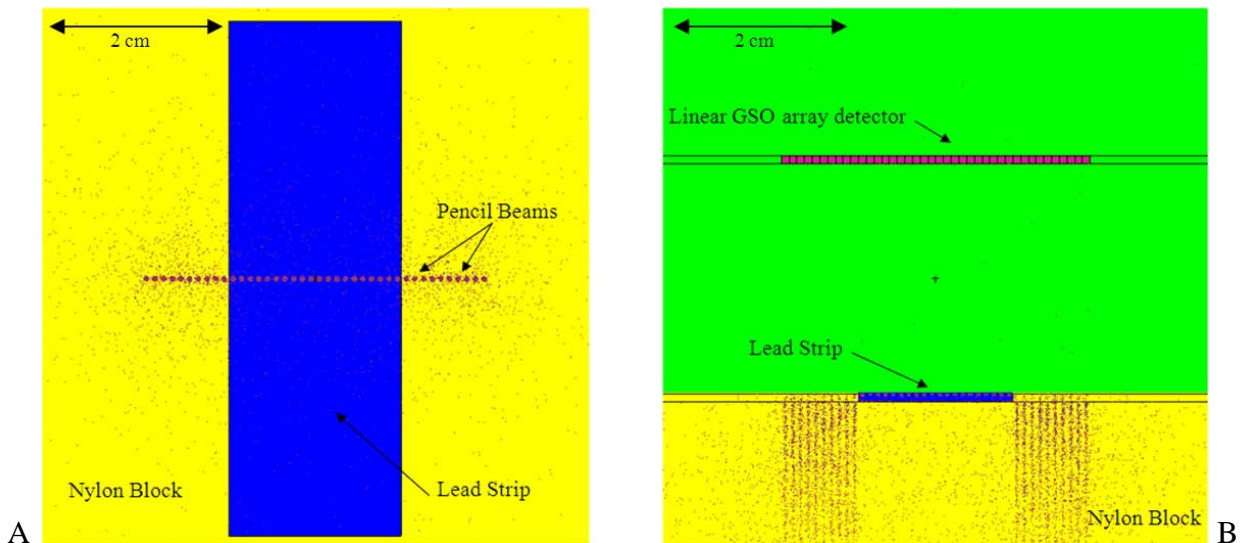


Figure 6-4. Geometry of the MCNP simulation of the pencil beam backscatter radiography of a lead strip on a nylon background: A) view of the YX-plane and B) view of the YZ-plane.

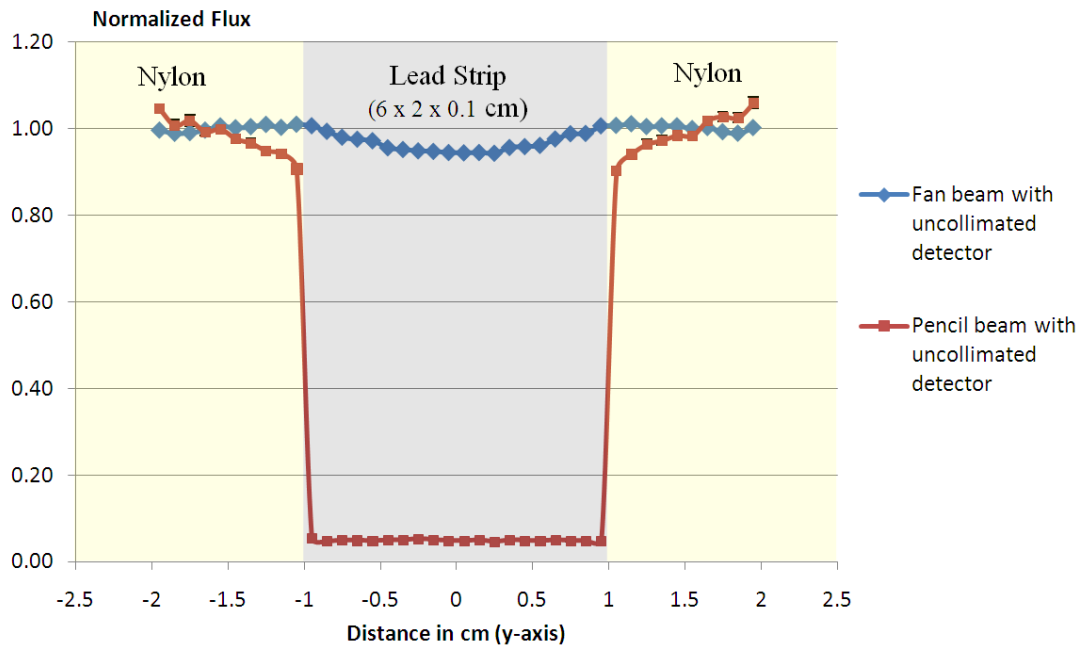


Figure 6-5. Comparison between the normalized fluxes observed in the uncollimated array detector with a fan beam source and with a pencil beam source.

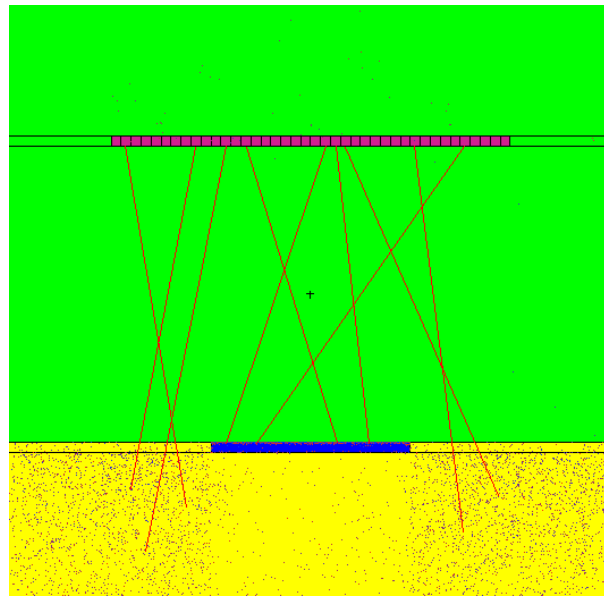


Figure 6-6. Possible paths of backscattered X-ray photons toward the uncollimated segmented detector with a fan beam source.

CHAPTER 7

CSD-SXI: PRINCIPLE AND MONTE CARLO SIMULATIONS

Principle of Collimated Segmented Detector Scatter X-ray Imaging

A more suitable way to use a segmented detector with a fan beam source would be to somehow force the photons backscattered in the target object to be detected only by the corresponding pixels (i.e. the pixels located directly over the location at which they backscattered) through collimation.

This can be done by fitting a grid made of a highly absorbing material onto the pixelated detector, in such a way that pixels or clusters of pixels would be separated from each other at regular intervals by the grid and could only see photons coming from a limited solid angle. Such a grid could be made of tungsten or lead, which are both strongly absorbing materials. Tungsten would be preferable to lead because its macroscopic absorption cross-section is about 26 % higher at 30 keV⁷, due to a higher electron density, and also because it is a much stronger material and would more easily resist deformation especially if the collimation grid is very fine.

Figure 7-1 shows the geometry of a MNCP simulation of Collimated Segmented Detector backscatter radiography of a lead strip on a nylon background. The collimation grid, shown in light blue, is composed of 0.4 mm thick tungsten plates (2 cm x 1 cm) separated by a regular 1 mm spacing. A 0.4 mm thick tungsten shielding was placed all around the array detector and the collimation plates to ensure uniform collimation. The resolution of the image is limited by the spacing between collimation plates, but also depends on other factors, such as the distance between the target object and the detector, the thickness of the tungsten plates and their collimation length (1 cm in this particular simulation). In practice, the spacing between the plates should be adjusted in such a manner that it would correspond to a natural number of pixel widths which would then be grouped to form a cluster. Matching the grid with the pixel clusters could

be one of the technical difficulties associated with this imaging method. In this chapter, this problem will be ignored and clusters of pixels of the segmented detector will be referred as pixels of the image.

With such a collimation grid, each pixel is shielded from the X-ray photons that do not come from directly under it, as seen in Figure 7-2. Therefore, it can be expected that this configuration reduces the averaging of the contrast between the pixels, which is the reason why an uncollimated array detector with a fan beam source could not work.

Figure 7-3 shows the comparison between the fluxes recorded by each pixel of the segmented detector with a fan beam source and with a pencil beam source from an MCNP simulation. In both cases, the tungsten collimation grid is placed below the detector to make the fluxes comparable. It is clear in Figure 7-3 that the introduction of a collimation grid has improved the contrast between the lead and nylon regions in the case of the fan beam source and that the contrast is now very similar with a fan beam source and with a pencil beam source.

In fact, the contrast is even slightly higher with the fan beam source; the relative contrast, defined as the ratio of the average fluxes over nylon and over lead is 36 with the fan beam against 25 with the pencil beam source. A possible explanation for this is shown in Figure 7-4. The scattering-to-absorption cross section ratio for 30 keV photons is 5% in lead and 400% in nylon and their mean free path in nylon is about 3 cm against 0.06 mm in lead.⁷ Therefore it can be expected that with a fan beam source, a large number of particles can travel inside the nylon and follow the same path as particle 1 in Figure 7-4. This increases the flux detected by pixels located over nylon with a fan beam source by 70% relative to when the pencil beam source is used. On the other hand, pixels located over lead will see a flux dominated by short path and single scatter photons since the scattering-to-absorption ratio is so low in lead. Consequently,

with a fan beam source, the flux detected by pixels located over nylon is increased by 70% while the one over lead is only increased by 15% and this results in a higher contrast between the nylon and the lead.

For a pencil beam however, this is not true because only the area directly under the pixel is illuminated so the surrounding regions cannot contribute to the flux. This theory is confirmed by the fact that the flux normalized to the number of source particles is 1.7 times higher with a fan beam source than with a pencil beam source over the nylon region and only 1.2 times higher over the lead region.

The average fraction of source particles in the detected fluxes was, in the case of the uncollimated detector (Figure 6-5), 8.49×10^{-5} and 2.78×10^{-6} with a fan beam and a pencil beam source, respectively, and, in the case of the collimated detector (Figure 7-3), 1.64×10^{-6} and 9.87×10^{-7} with a fan beam and a pencil beam source respectively. The uncertainties on these values are on the order of 1% for the uncollimated detector, and 4% for the collimated detector.

These figures confirm the theory described in Figure 7-2. For the fan beam source, the flux recorded in the detector is almost two orders of magnitude smaller when the tungsten collimation is introduced because then, the segmented detector mainly detects photons that are backscattered up and toward the corresponding pixel while other photons are absorbed in the tungsten. The decrease in recorded flux with a pencil beam source when the tungsten collimation is introduced is much smaller, less than a factor of three. Even though the count rate recorded with the fan beam source is less than twice as large as with the pencil beam source in the case of the collimated detector, it should be noted that experimentally, a fan beam source yields many more

photons per unit time than a pencil beam source, and this is why an acceleration relative to the pencil beam techniques is expected.

Resolution

Figure 7-3 also shows that the resolution with the fan beam source is lower than with the pencil beam source. Whereas going from within 10% of the largest flux value (corresponding to the nylon) to within 10% of the smallest (corresponding to the lead) takes only 1 mm in the case of the pencil beam, the same transition takes about 3 mm for the fan beam method.

Contrary to pencil beam imaging techniques for which the image resolution is roughly the step between each measurement, the calculation of the resolution with a fan beam source is slightly more complex. Figure 7-5 shows the span of the target object that can be seen by a collimated detector with a fan beam source, where P is the pixel size, H is the distance between the target object and the detector, L is the collimation length and R is the resolution. From the intercept theorem, the resolution, R is defined as:

$$R = P \frac{\left(\frac{H-L}{2}\right)}{\frac{L}{2}} \quad (7-1)$$

In the case of the lead strip laid on the nylon block for which $P = 0.6$ mm, $H = 30$ mm and $L = 10$ mm, the resolution R was 3.0 mm which is about 3 times larger than the resolution obtained by the pencil beam technique.

This value of $R = 3$ mm for the fan beam versus $R = 1$ mm is confirmed by the results from Figure 7-3, in which the transition from the lead to nylon flux value is done in about 3 mm with the fan beam source against only 1 mm with the pencil beam source. However, the resolution cannot be so simply defined; indeed, the area below the central part of the target object can be seen from every part of the pixel whereas some other areas can only be seen from a fraction of the pixel's surface, and therefore have less impact on the measurement of the flux. In fact, if the

target object is homogeneous, it can be assumed that each point $y = t$ of a pixel receives equal flux contribution from every point of the target object that it sees, as seen in Figure 7-6. The contribution of this point of the pixel to the image is therefore:

$$c(t, y) = \begin{cases} 1 & \text{if } (t - H \tan \theta_1) < y < (t + H \tan \theta_2) \\ 0 & \text{else} \end{cases} \quad (7-2)$$

where:

$$\tan \theta_1 = \frac{t}{L} \quad \text{and} \quad \tan \theta_2 = \frac{P-t}{L} \quad (7-3)$$

Consequently, a pixel with width P would see the following contribution from each point y of the target object:

$$C(y) = \int_0^P c(t, y) dt \quad (7-4)$$

Figure 7-7 shows the normalized contribution from a homogeneous target object to a pixel of the image of width $P = 0.06$ cm, with collimation length $L = 1$ cm and with an $H = 3$ cm stand-off. It can be noticed that the resolution is indeed 3 mm, as shown previously. The area directly under the pixel has a contribution of 1 because it can be seen from any part of the image pixel. On the other hand, areas that are not located directly under the pixel can only be seen by a fraction of its surface, which results in a smaller contribution to that pixel.

Influence of Collimation

Figure 7-8 shows the geometry of another MCNP simulation. In this case, the target object is the same lead strip located 2 cm deep inside a nylon block. For this simulation, for which we obviously expect the contrast to be smaller between the two types of material, the stand-off distance, H , is 3 cm, and the pixel width and the collimator length are 1 mm and 1 cm, respectively. For all the simulations in this section, the maximum energy of X-ray photons was set to 120 keV, in order to have a better depth penetration in the nylon.

The comparison between the flux observed by the collimated and shielded detector with the pencil beam and the fan beam sources is shown in Figure 7-9. In this case, the contrast is also higher with the fan beam source, with a relative contrast of 1.61 between the nylon and the lead against 1.34 with the pencil beam source. However, whereas the resolution remains close to 1 mm with the pencil beam technique, it seems that the resolution with the fan beam was greatly reduced, to about 5 mm (transition from the value of the flux over the nylon to over the lead), and indeed the formula for the resolution gives $R = 5.4$ mm at the depth of the lead strip. The average fraction of particles counted in the fluxes relative to the source was 5.76×10^{-6} with the fan beam source, and 3.18×10^{-6} with the pencil beam source.

Other MCNP simulations were done with different collimation lengths in order to improve contrast as well as resolution, and to understand the effect of collimation on resolution. In practice, it would be too expensive and unpractical to purchase sets of tungsten grids with different collimation lengths. Instead, simply lowering the position of the collimated detector should be almost equivalent to extending the length of the collimator. The other collimation lengths that were tried are $L = 1.5$ cm, $L=2$ cm and $L = 2.5$ cm for which the theoretically calculated fan beam image resolutions are, respectively, $R = 3.4$ mm, $R = 2.4$ mm and $R = 1.8$ mm.

Figure 7-10 shows the difference between the detected fluxes for the four collimation lengths with a fan beam source. The resolution improves as the collimation is increased: R is about 4 mm for the 1.5 cm collimation, 3 mm for the 2 cm collimation and 2 mm for the 2.5 cm collimation. The best contrasts were obtained with the 2.0 and 2.5 cm collimation, but, in the case of the latter, the count rate was reduced by a factor of two due to over-collimation. The average fraction of source particles in the detected fluxes was 5.76×10^{-6} with 1.0 cm

collimation, 2.40×10^{-6} with 1.5 cm collimation, 9.95×10^{-7} with 2.0 cm collimation and 5.06×10^{-7} with 2.5 cm collimation.

Depth information and Possibility of 3D Imaging

2D Collimation Grid for Better Depth Resolution

Replacing a linear grid by a 2D grid, as seen in Figure 7-11, could improve the depth selection. Such a grid could prevent photons that do not backscatter in the region of interest from being detected. In such a case, it might be more efficient to tilt the detector toward the fan beam; otherwise, the count rate for the regions that are far away from the source would not detect anything. For the particular grid used in the following MCNP simulations, there were 6 rows of 40 pixels for a total of 240 grid elements, each of which was 2.5 mm long and 1 mm wide. The thickness of tungsten plates was 0.4 mm.

Three MCNP simulations, with geometries shown in Figure 7-12, were performed with a linearly collimated segmented detector with no inclination, with a linearly collimated segmented detector at a 45° inclination, and with a 2D grid collimated segmented detector at a 45° inclination. In all cases 1.5 cm collimation was used. The target object consists of a 1 cm thick and 2 cm wide air gap located 1.0 cm deep inside an aluminum block. In the case of the linear detector with no inclination, the stand-off was 3 cm from the bottom of the detector (1.5 cm from the bottom of the collimator). The collimation length was chosen to obtain the best possible contrast for the linearly collimated detector array without inclination. The maximum energy of the photons was 120 keV.

Figure 7-13 shows the flux recorded in each pixel of the segmented detector for all 3 cases from the MCNP simulations. For the 2D collimated detector, each of the 6 rows had different weights to prevent the overall flux from being dominated by the first row only; the count rate detected by the first row is about 3 times larger than for the second row, and even more than for

the others. This is why the flux for each row was normalized and then were all averaged to give only one value.

The graph from Figure 7-13 shows that the contrast in the detected flux between the air and the aluminum is in the 5 to 10% range for both the linearly collimated detector without any inclination and the 2D collimated array detector at a 45° inclination. It is lower than 5% in the case of the linearly collimated detector at a 45° inclination due to poor collimation.

The areas of the array detector corresponding to the air should detect a lower flux because the scattering cross section of photons in air is lower than in aluminum. However, it can be noticed that the contrast is inverted in the case of the linearly collimated detector without any inclination. This is because with these settings, for which the contrast is optimal, the array detector is over-collimated so the flux that is recorded represents mostly the area located under the air. Because the absorption cross section of photons in air is smaller than in aluminum, more photons reach that depth when they went through the air first and therefore the flux recorded by the detectors is higher for this region. This is one type of shadowing effect.³

However, the flux recorded by each row of the 2D collimated array detector contains much more information than the flux averaged over all rows.

Possibility of 3D Backscatter Imaging

Each row of the 2D collimated array detector corresponds to a certain depth. A closer view of the 2D collimated array detector is shown in Figure 7-14. At the intersection with the fan beam plane, row 1 corresponds to a depth of 0.80 cm below the surface of the aluminum, row 2 to a depth of 1.14 cm, row 3 to 1.50 cm, row 4 to 1.85 cm, row 5 to 2.21 cm and finally, row 6 corresponds to a depth of 2.59 cm.

However, each row represents in fact a certain depth distribution which can be seen as resolution on the z-axis. Therefore, the contribution of each z-level of the target object to every

row of pixels of the array detector can be obtained similarly to the contribution of each point of the y-axis. However, because of the inclination θ_d of the detector, the expression for the contribution is slightly more complicated. Also, an absorption term must be introduced to account for depth penetration. Each point t of a pixel row ($0 < t < P$) can directly see the photons scattered in the plane containing the fan beam (red arrow in Figure 7-15). Therefore:

$$c(t, z) = \begin{cases} 1 & \text{if } (D \tan(\theta_d - \theta_1) - H) < z < (D \tan(\theta_d + \theta_2) - H) \\ 0 & \text{else} \end{cases} \quad (7-5)$$

where:

$$\tan \theta_1 = \frac{t}{L} \quad \text{and} \quad \tan \theta_2 = \frac{P-t}{L} \quad (7-6)$$

and, with H_c and D_c the height of the center of the pixel and its distance to the beam, respectively:

$$D = D_c + \left(t - \frac{P}{2}\right) \sin(\theta_d) \quad \text{and} \quad H = H_c + \left(t - \frac{P}{2}\right) \cos(\theta_d) \quad (7-7)$$

However, if $P \ll D$, then $H \approx H_c$ and $D \approx D_c$. The contribution of each point of the z-axis to the pixel row is then:

$$C(z) \cong e^{-2z/mfp} \int_0^P c(t, z) dt \quad (7-8)$$

where mfp is the mean free path of photons in the medium. The exponential term allows taking into account the absorption in the medium as the photons travel downward and then upward, toward the detector after backscattering.

Figure 7-16 shows the contribution of every z-level of the target object to each pixel row of the array detector. The value of the mean free path used in this case was 1.5 cm which is the average mean free path of 120 keV photons in the aluminum surrounding the void.

From the graph in Figure 7-16, it appears that row 1 is under-collimated and only a small fraction of photons detected by this row would have been backscattered in the region of the void,

located between 1.0 and 2.0 cm deep in the aluminum; the image would be dominated by the flux of photons scattering in the region above the void. On the contrary, rows 5 and 6 are over-collimated. Rows 2, 3 and 4 are all reasonably collimated even though they also see significant flux contribution from the regions located over and below the void. This is a simplified contribution model (it was assumed that photons remain on the fan beam plane as they travel through the target object). Figure 7-17 shows the fluxes detected in the MCNP simulation by each of the six rows of pixels of the 2D array detector with a 45° inclination in the case of the 1 cm thick air gap.

All rows show contrast of at least 10% between the void and the aluminum, with rows 2 (30%), 3 (40%), 5 (30%) and 6 (50%) showing the best contrasts. It should be recalled that the best contrast that could be achieved with a linearly collimated detector with no inclination was below 10%. It can be noticed that the contrast in the flux detected at rows 1, 2, 3 and 4 is inverted compared to the flux at rows 5 and 6. This is because rows 5 and 6 are over-collimated and are tallying fluxes of particles backscattered below the region of the void. Indeed the absorption cross section of photons in aluminum is higher than in air, therefore X-rays reaching that depth are more numerous if they traveled through air. This is the same shadowing effect as was observed for the linearly collimated detector in Figure 7-13. The flux measured at row 4 shows a smaller contrast than at rows 3 and 5 because in this collimation range, the contrast goes from negative (row 3) to positive (row 5), as the shadowing effect cancels out the difference in scattering cross section in air and aluminum.

It should be noted that the fluxes detected in this MCNP simulation were, on average, 1.36×10^{-6} for row 1, 7.14×10^{-7} for row 2, 4.27×10^{-7} for row 3, 3.19×10^{-7} for row 4, 2.56×10^{-7} for row 5 and 2.02×10^{-7} for row 6. By comparison, the linearly collimated

detector with no inclination saw an average flux of 9.04×10^{-7} . Because the flux detected for rows corresponding to the highest depths is low, the statistical error for these rows can be high. Also, actual detection of a feature is always better than detection of its shadow. This is why it is expected that rows 2 and 3 give the best results.

The fluxes measured by the different rows of a 2D collimated segmented detector put together could form a 3D image of a feature. It is roughly equivalent to changing the collimation of a linearly collimated detector for each depth. Although the statistical error is larger, the contrast is much higher and it only requires one scan so it is faster. However, true 3D imaging with a backscatter X-ray method is difficult since features can show on an image even though they are below the collimation plane, due to shadowing effects. Therefore, some features could be hidden by others located at a shallower point.

CSD-SXI 3D Imaging: Example of a Ring of Air Inside Aluminum

X-ray backscatter images of a ring of air located 1.0 cm below the surface of an aluminum block were obtained using MCNP simulations. This ring, shown in Figure 7-18, has an inner diameter of 0.5 cm, an outer diameter of 1.5 cm and is 1.0 cm high.

Images of this ring were simulated for three different setups: a pencil beam system with a NaI detector 5.9 cm in diameter, a fan beam system with a linearly collimated GSO array detector with no inclination and a fan beam system with a 2D collimated GSO array detector at a 45° inclination. The pencil beam system is similar to the RSD system developed by the SXI group; the detector is located 9.5 cm away from the pencil beam and the collimation used varied between 0.1 and 1.5 cm. The distance between the bottom of the detector and the surface of the target is 3.0 cm. The geometries of all three systems are shown in Figure 7-19.

The average normalized flux detected per 1 mm pixel at the bottom surface of the detector after MCNP simulations for the pencil beam systems with a 1 cm collimation was equal to

4.08×10^{-6} averaged over a total detector surface of 27.3 cm^2 . In the case of the linearly collimated segmented detector, the average normalized flux is 4.02×10^{-6} averaged over a pixel surface of $1.5 \times 10^{-1} \text{ cm}^2$. For the 2D collimated segmented detector system, the average normalized flux was 4.0×10^{-6} for row 1, 2.1×10^{-6} for row 2, 1.2×10^{-6} for row 3, 8.9×10^{-7} for row 4, 7.2×10^{-7} for row 5 and 5.6×10^{-7} for row 6 average over a pixel surface of $2.5 \times 10^{-2} \text{ cm}^2$. This means that the detection rate of the NaI detector is about two hundred times larger than for each linearly collimated pixel, and more than one thousand times larger than for each 2D collimated pixel.

However, it should be remembered that for the pencil beam system, only one pixel value can be measured at a time. So if a 40x40 1 mm pixel image is considered, the pencil beam system will have to spend some time on each of the 40 pixels of the line, while the fan beam systems will record one entire 40 pixel line of the image at a time. In this case, the pencil beam system would be 4.5 times faster than the linearly collimated array detector system with the same statistical error on average for the pixels of the image. The 2D collimated array detector system would be 27 times slower, with the same statistical uncertainty for the NaI detector and row 1, or almost 200 times slower, with the same statistical uncertainty for the NaI detector and row 6, although six images would be acquired simultaneously.

However, it should be remembered that these values are given for the image acquisition of a 4x4 cm target object. The use of a longer segmented detector would reduce these ratios and it can be estimated that with a 1 meter long pixelated detector, CSD-SXI would become faster than pencil beam systems. CSD-SXI would then be suitable for large area inspection, such as the inspection of the hull of commercial airplanes. Some manufacturers, such as Envision Product Design can build linearly segmented detector up to 2 meters long.¹¹

Figure 7-20 shows the MCNP generated X-ray backscatter images (40x40 pixels, 1 mm per pixel) of the air ring located 1 cm deep inside aluminum with a RSD-like pencil beam system. The four images were obtained with different collimation lengths: 0.1 cm, 0.5 cm, 1.0 cm and 1.5 cm. The average flux values for each of these images were 1.24×10^{-5} , 8.62×10^{-6} , 4.08×10^{-6} and 8.58×10^{-7} , respectively, averaged over a surface of 27.3 cm^2 . The corresponding statistical error was below 8% for all collimation levels (less than 1% at 0.1 cm). Each of these images required 1600 MCNP runs, each of them taking a few seconds, one for every pixel. It seems that the best images of the ring with this pencil-beam system are the first two, which were generated with 0.1 and 0.5 cm collimation. However all four images are rather blurry and have fairly poor contrast. Moreover, the exact dimensions of the ring cannot be measured in any of these images.

Figure 7-21 shows the MCNP generated images of the air ring in aluminum with a fan beam source and using a linearly collimated array detector without any inclination. These three images were generated using different collimation lengths (0.5 cm, 1.0 cm and 1.5 cm) and the average flux recorded by the MCNP simulations were 3.98×10^{-5} , 1.35×10^{-5} and 4.02×10^{-6} for a pixel surface of 0.15 cm^2 . The statistical error for each pixel of these images was below 7%. 40 MCNP runs (30 minutes each) were necessary to generate these images. The last two images show the best contrast. It can be noticed that the ring appears lighter than the aluminum as was previously observed in Figure 7-13. Also the ring is not perfectly centered in the middle of these images, and this indicates that they show some kind of shadow of the ring rather than the ring itself. Even though the contours of the ring of air seem clearer than in the case of the pencil beam system, the inverted contrast and the shadowing effect make these images more difficult to read.

Figure 7-22 shows the MCNP generated images of the air ring in aluminum with a fan beam source using a 2D collimated array detector at a 45° inclination. Each of these six images represents one of the rows of the collimated pixelated detector and corresponds to the following depths in the aluminum: 0.80 cm, 1.14 cm, 1.50 cm, 1.85 cm, 2.21 cm, and 2.59 cm. It should be recalled that the air ring is located between 1 and 2 cm below the surface of aluminum. This is better shown in Figure 7-23. All six images were generated using 40 MCNP runs (30 minutes each), one for each row and, in practice, they would be generated by only one scan across. The average flux recorded by the MCNP simulations was 4.00×10^{-6} for row 1, 2.09×10^{-6} for row 2, 1.24×10^{-6} for row 3, 8.94×10^{-7} for row 4, 7.19×10^{-7} for row 5 and 5.61×10^{-7} for row 6. The statistical error for each pixel was of the order of 8% for the first row and about 15% for the last row. The image corresponding to the first row is under-collimated and this is why its contrast is so poor. The images generated by rows 4, 5 and 6 are all over-collimated (the collimation plane is either at the bottom of or below the ring). As a result they show either poor contrast or blurry ring contours. Also, for the last two rows, the ring can only be detected because of the shadowing effect and the contrast is inverted. However for rows 2 and 3, the contrast is very high (of the order of 50%) and the shape of the ring is perfectly clear. The dimensions of the ring can also be measured with a fairly good precision. These two rows represent depths of around 1.15 cm and 1.50 cm, which correspond to the location of the air ring. The contrasts observed in these six images are consistent with what was observed in Figure 7-17.

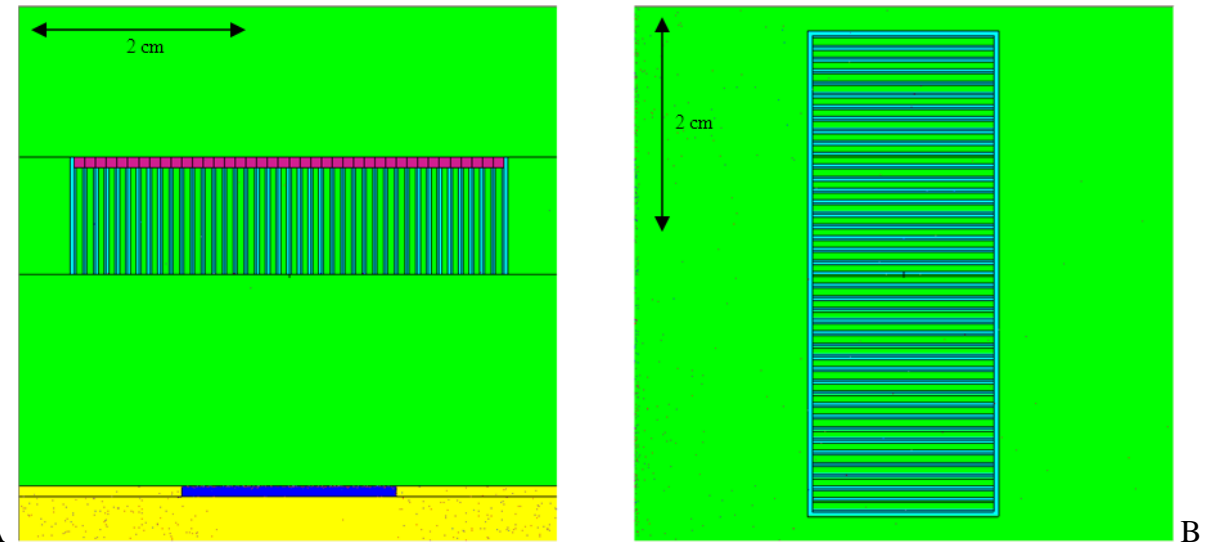


Figure 7-1. Geometry of the MCNP simulation of a Collimated Segmented Detector Scatter X-ray Image of a lead strip on a nylon background: A) view of the YZ -plane and B) view of the XY-plane.

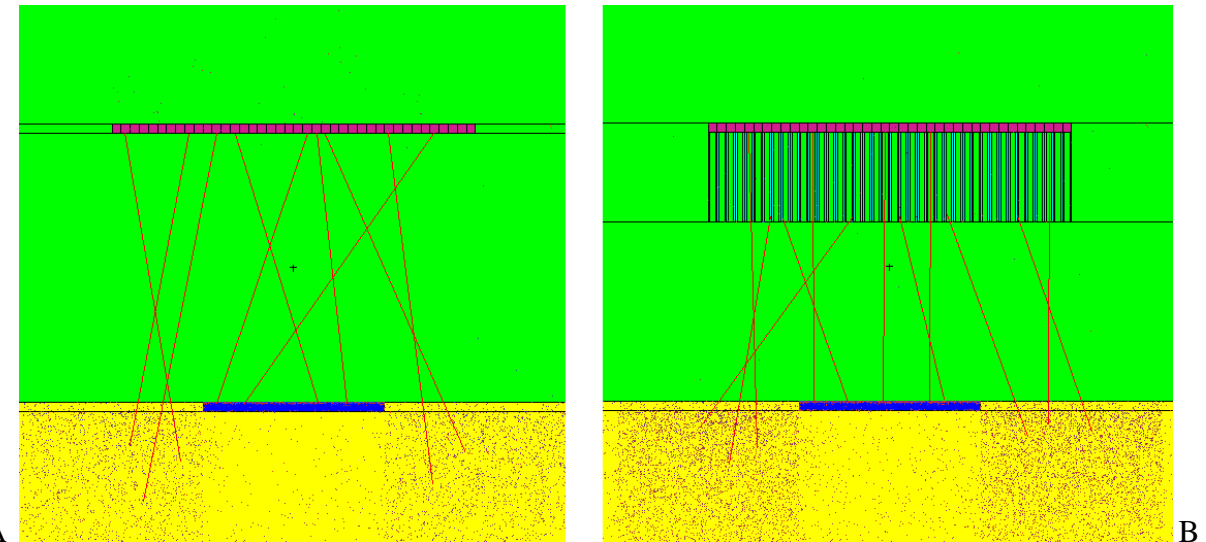


Figure 7-2. Possible paths of backscattered X-ray photons from a fan beam source toward the segmented detector: A) without collimation and B) with a collimation grid.

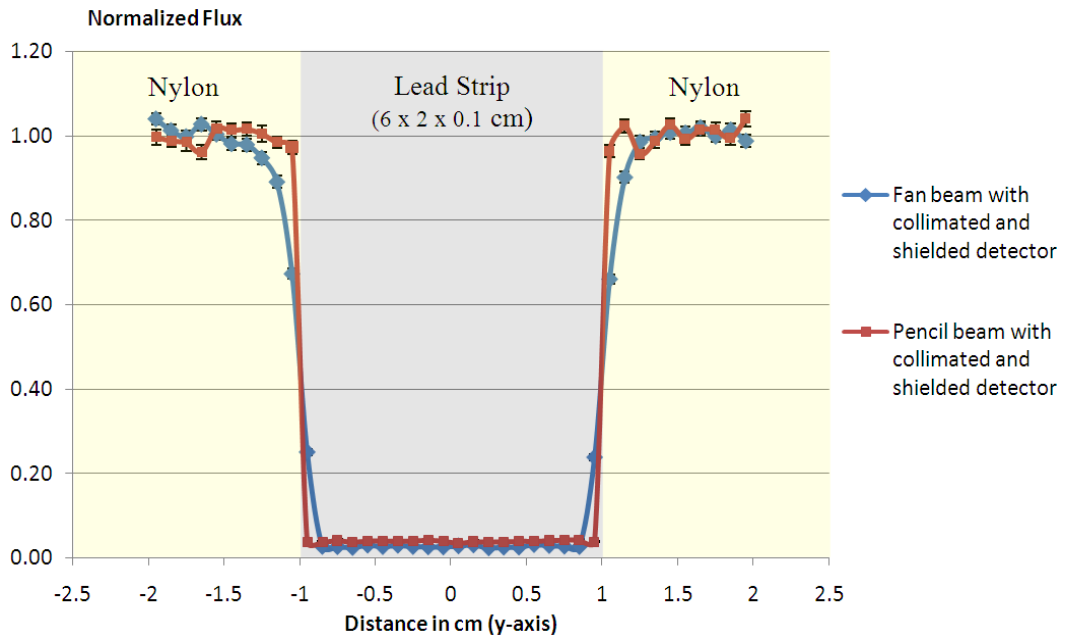


Figure 7-3. Comparison between the normalized fluxes observed in the collimated array detector with a fan beam source and with a pencil beam source for a lead strip on the surface of a nylon block.

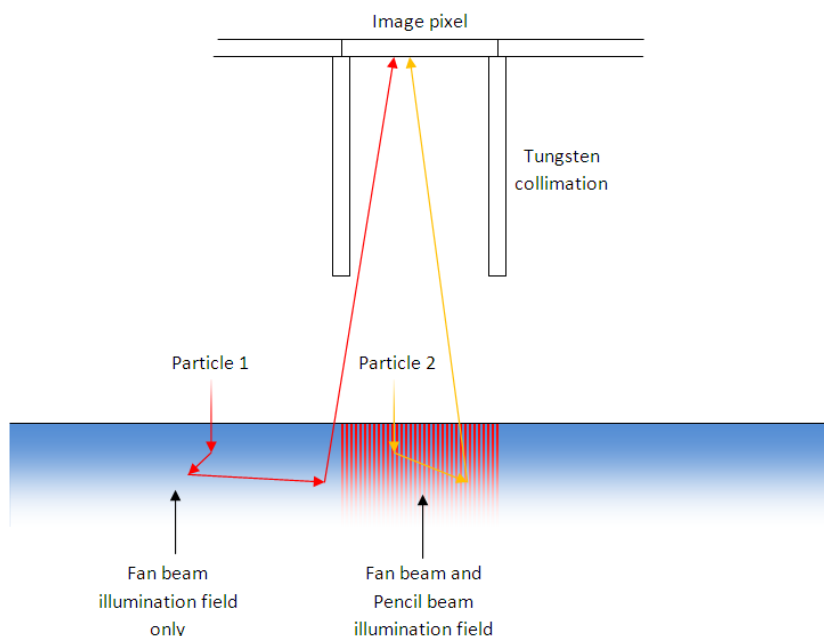


Figure 7-4. Possible paths of X-ray photons eventually reaching an image pixel. The path of particle 1 is only valid with a fan beam source because it starts outside the pencil beam illumination field.

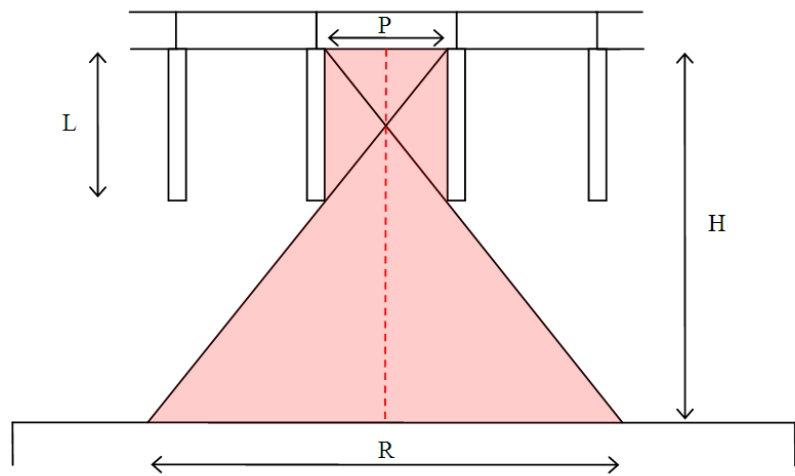


Figure 7-5. Measure of the resolution for Collimated Segmented Detector Scatter X-ray Imaging.

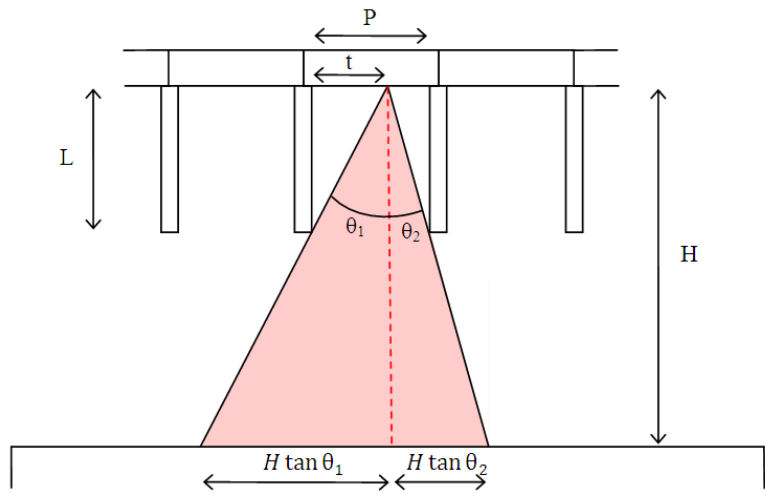


Figure 7-6. Backscatter X-ray secondary source as seen from point $y = t$.

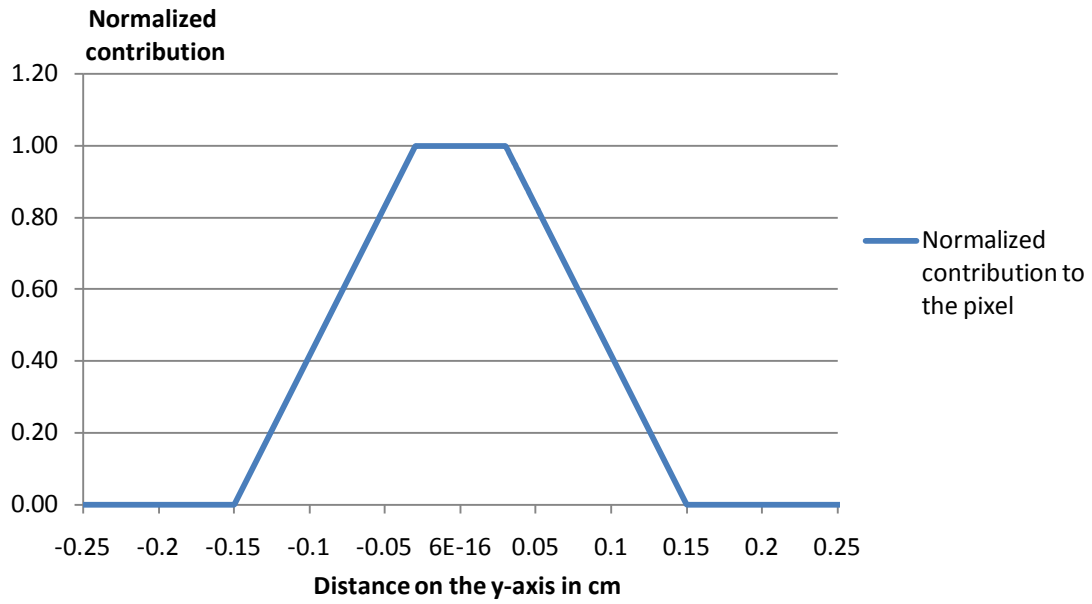


Figure 7-7. Normalized contribution to a 0.6 mm wide pixel, with a 1 cm collimation.

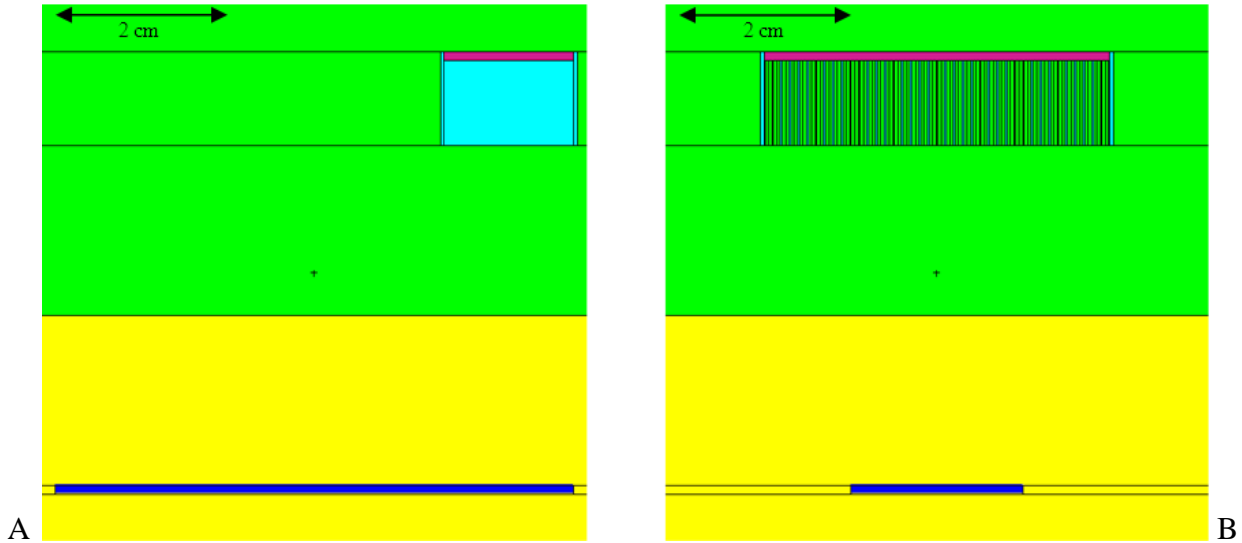


Figure 7-8. Geometry of the MCNP simulation of a Collimated Segmented Detector Scatter X-ray Image of a lead strip 2 cm deep inside a nylon block: A) view of the XZ-plane and B) view of the YZ-plane.

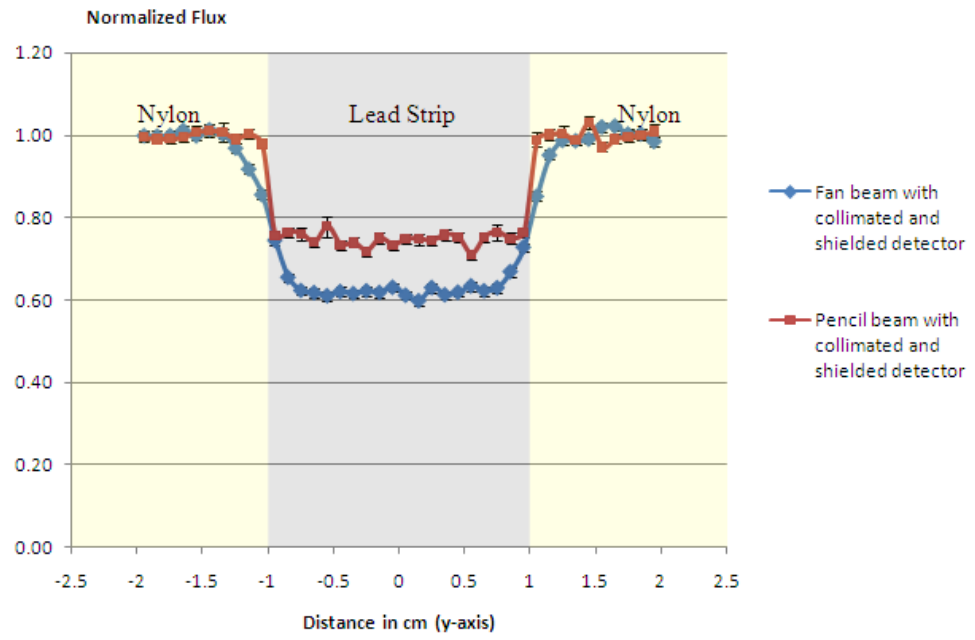


Figure 7-9. Comparison between the normalized fluxes observed in the collimated array detector with a fan beam source and with a pencil beam source for a lead strip 2 cm deep in a nylon block.

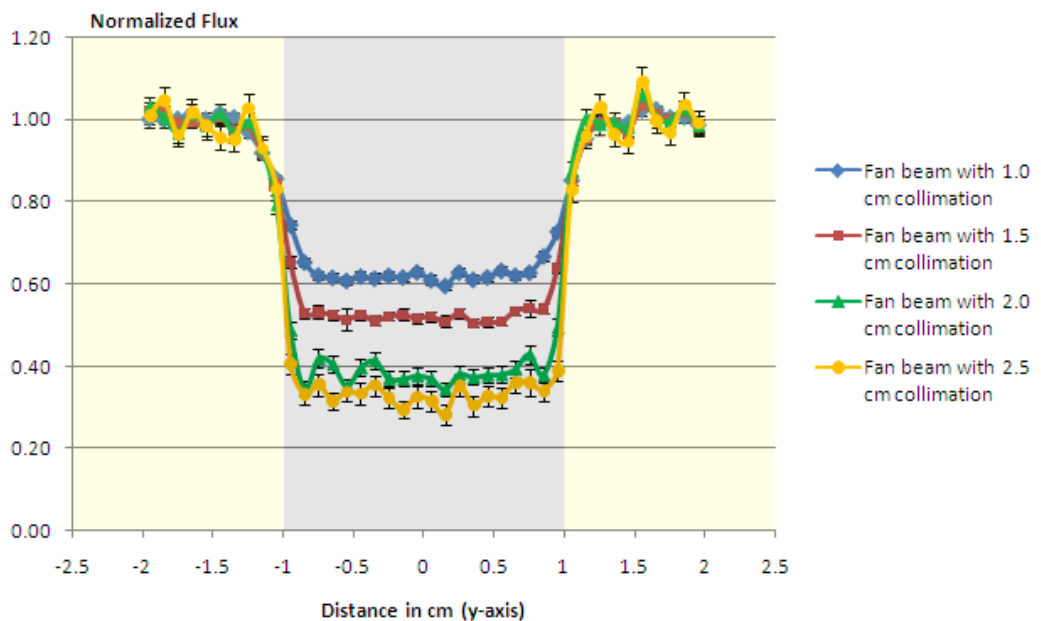


Figure 7-10. Comparison between the normalized fluxes observed in the collimated array detector with a fan beam source for four different collimation lengths for a lead strip 2 cm deep in a nylon block.

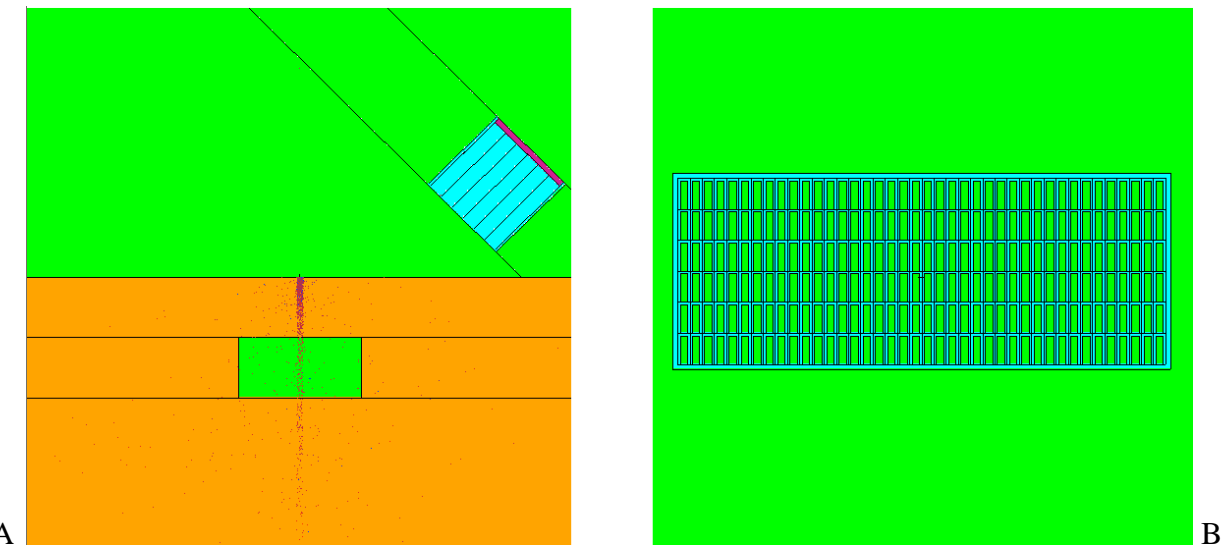


Figure 7-11. Geometry of the MCNP simulation of a Collimated Segmented Detector X-ray Image of a 1 cm deep air gap inside an aluminum block with a 2D grid collimated detector at a 45° inclination: A) view of the XZ-plane and B) view of a plane parallel to the detector.

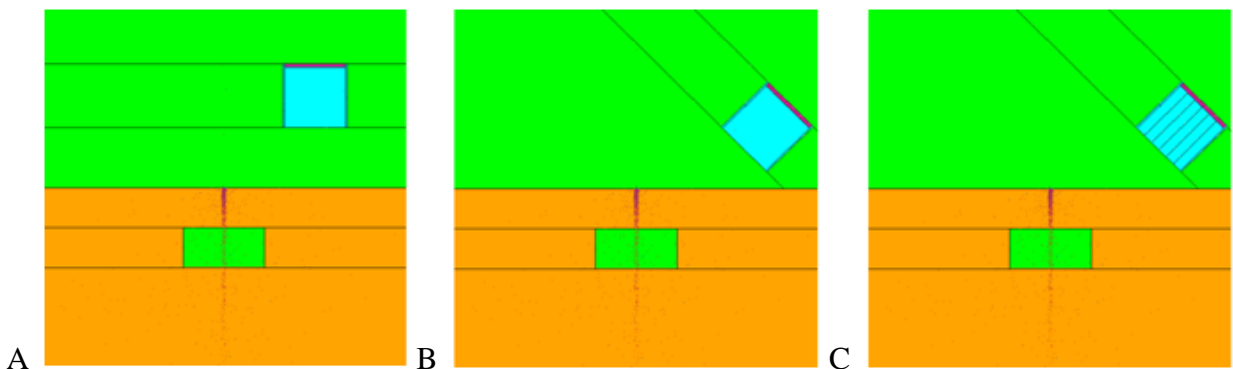


Figure 7-12. Geometries of the 3 MCNP simulations of an air gap inside an aluminum block, views of the XZ-plane: A) linearly collimated segmented detector, B) linearly collimated segmented detector at a 45° inclination, and C) 2D collimated segmented detector at a 45° inclination.

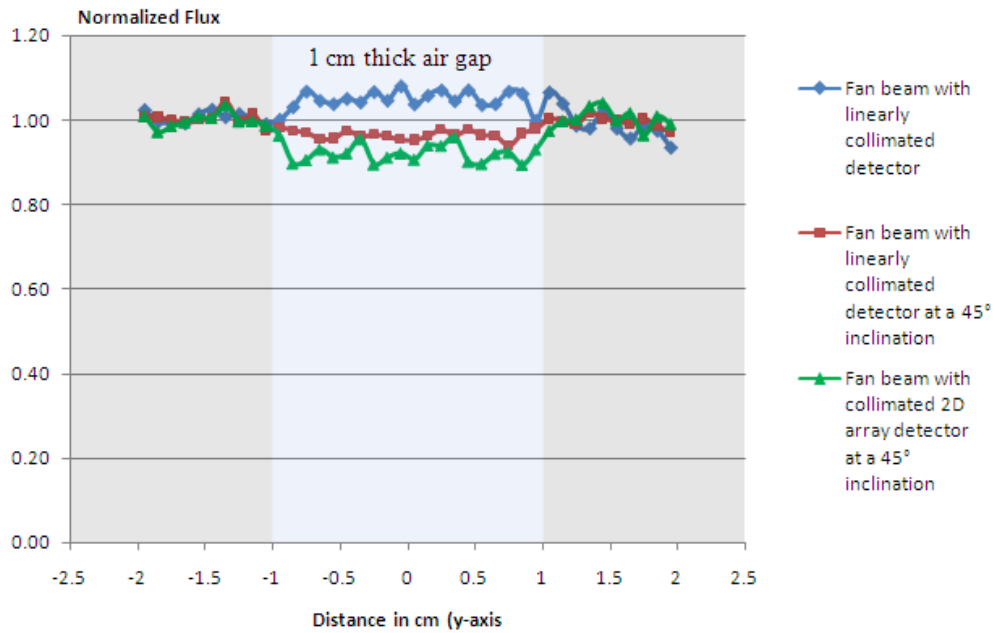


Figure 7-13. Comparison between the normalized fluxes from MCNP simulations of a 1 cm deep air gap inside an aluminum block with a fan beam source.

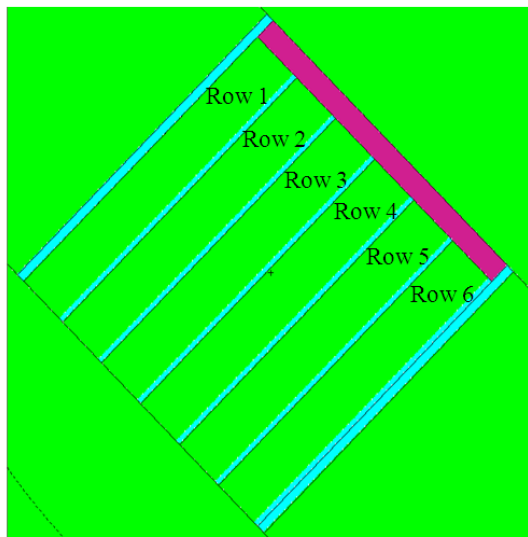


Figure 7-14. Geometry of the 2D collimated array detector at a 45° inclination, view of the XZ-plane.

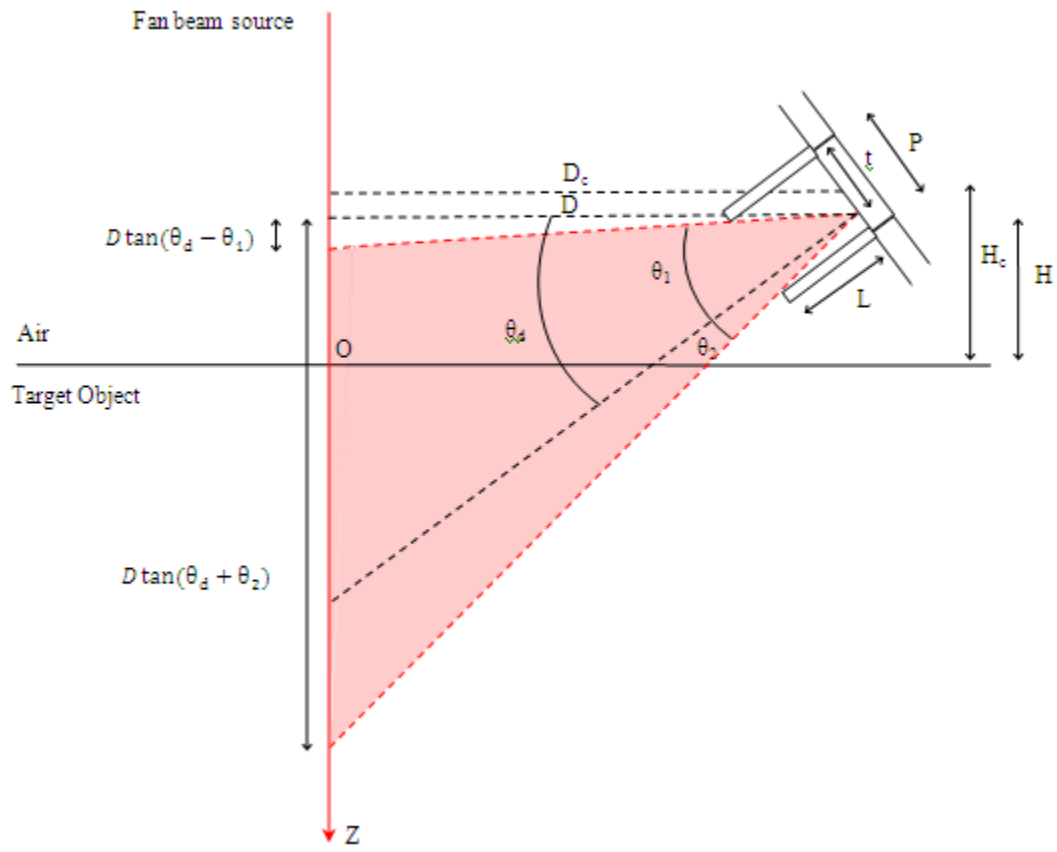


Figure 7-15. Backscatter X-ray secondary source as seen from point t .

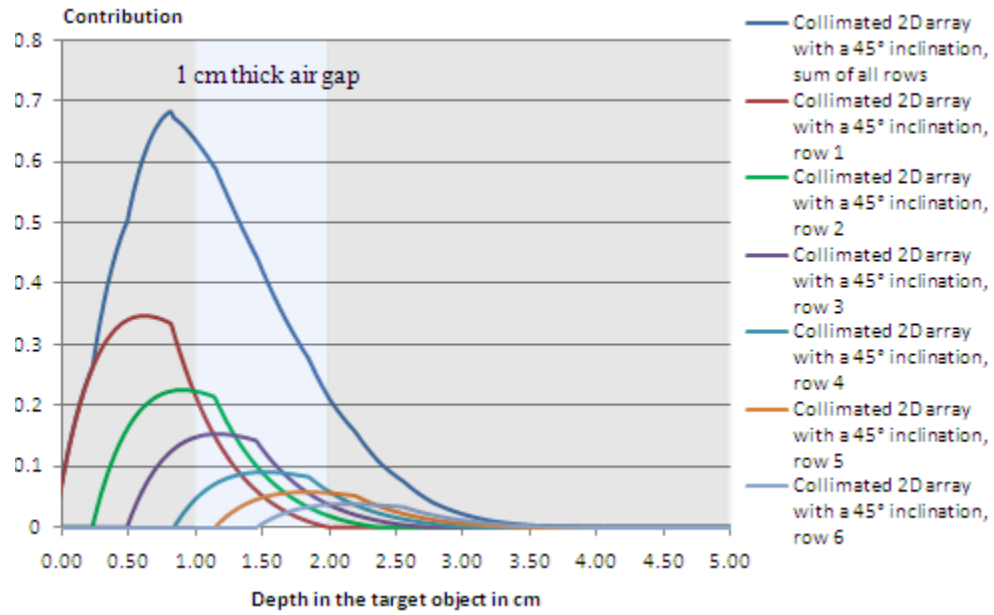


Figure 7-16. Normalized contribution of each z-level in the target object to all 6 rows of pixels and to the sum of the rows.

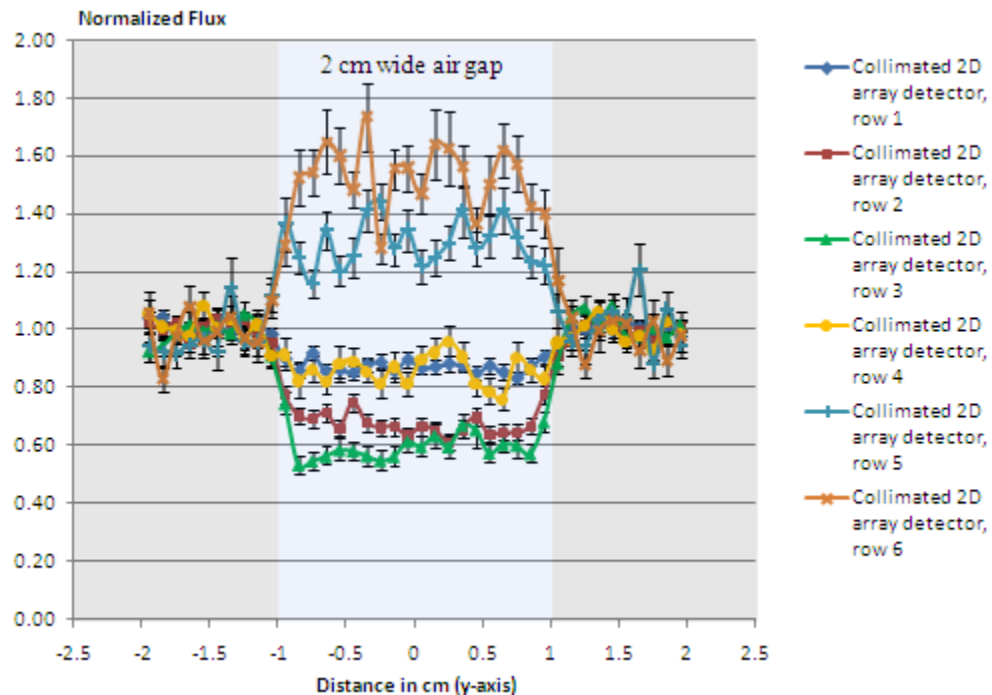


Figure 7-17. Comparison between the fluxes recorded by rows 1, 2, 3, 4, 5 and 6 of the 2D collimated array detector, with a 45° inclination from an MCNP simulation of CSD-SXI of an air gap inside an aluminum block.

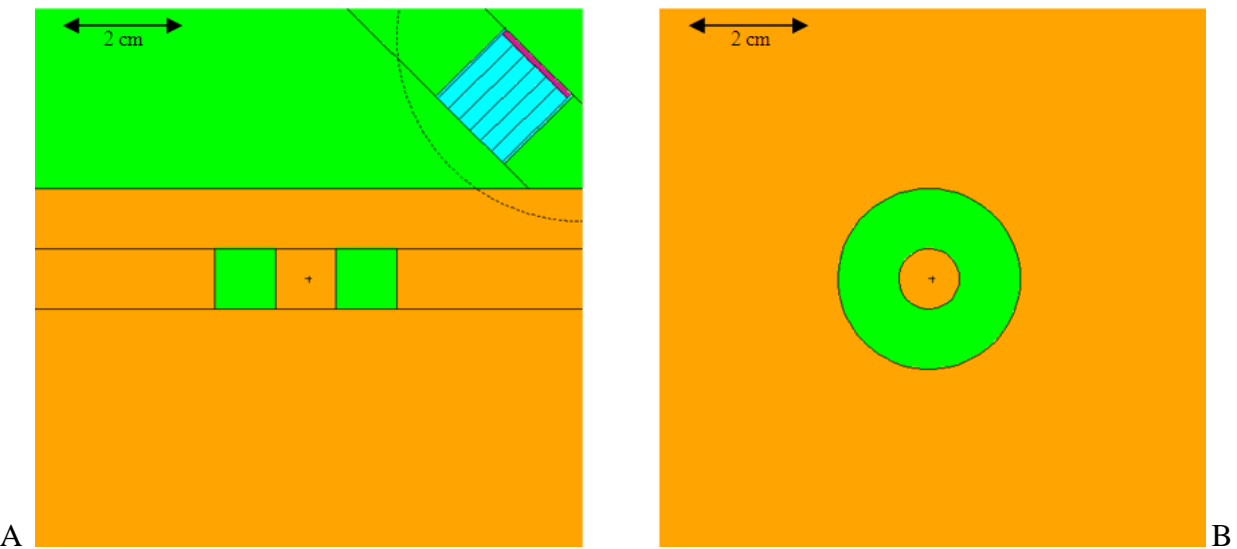


Figure 7-18. Geometry of the ring of air located 1 cm deep inside aluminum: A) view of the XZ-plane and B) view of the XY-plane.

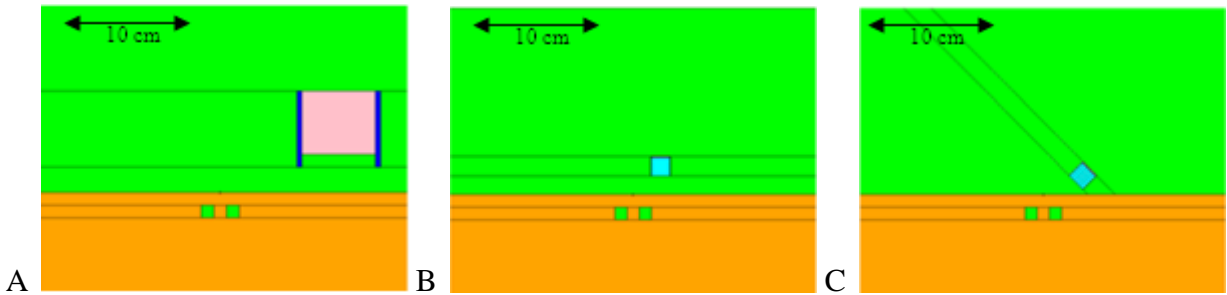


Figure 7-19. Geometries of the three different imaging systems: A) NaI detector with pencil beam source, B) linearly collimated array detector with fan beam source and C) 2D collimated array detector at a 45° inclination with fan beam source.

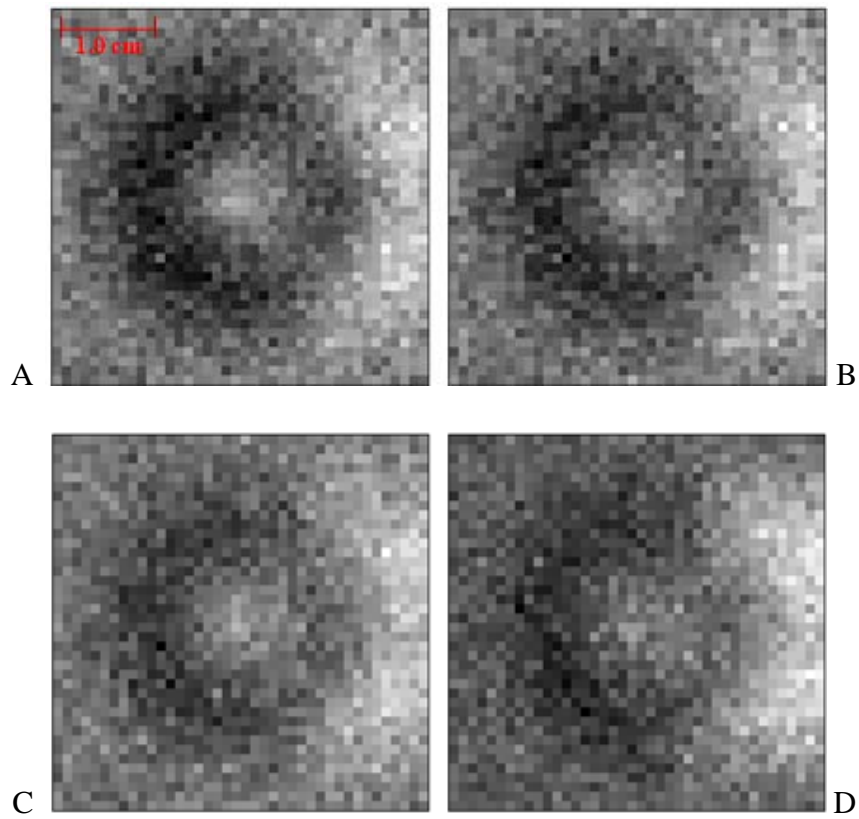


Figure 7-20. MCNP generated X-ray backscatter images of a ring of air inside aluminum using a NaI detector with a pencil beam source with the following collimation lengths: A) 0.1 cm, B) 0.5 cm, C) 1.0 cm and D) 1.5 cm.

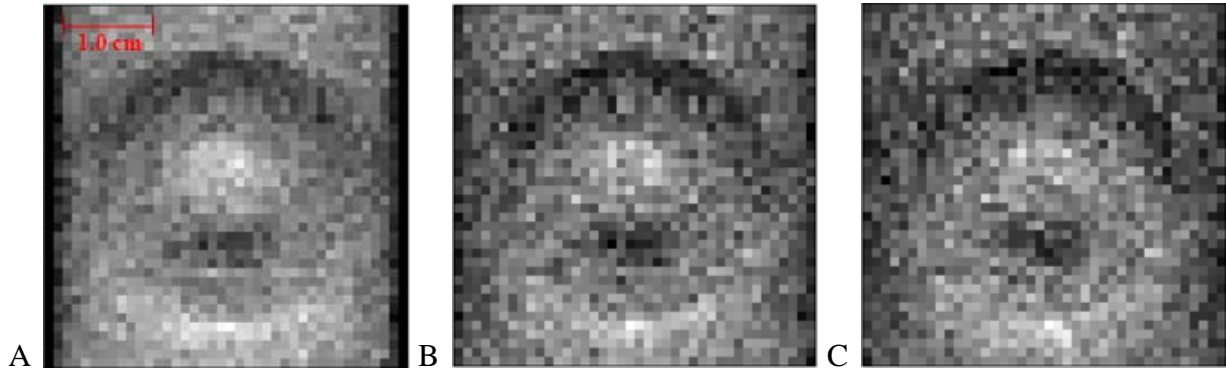


Figure 7-21. MCNP generated X-ray backscatter images of a ring of air inside aluminum using a linearly collimated segmented detector with a fan beam source with the following collimation lengths: A) 0.5 cm, B) 1.0 cm and C) 1.5 cm.

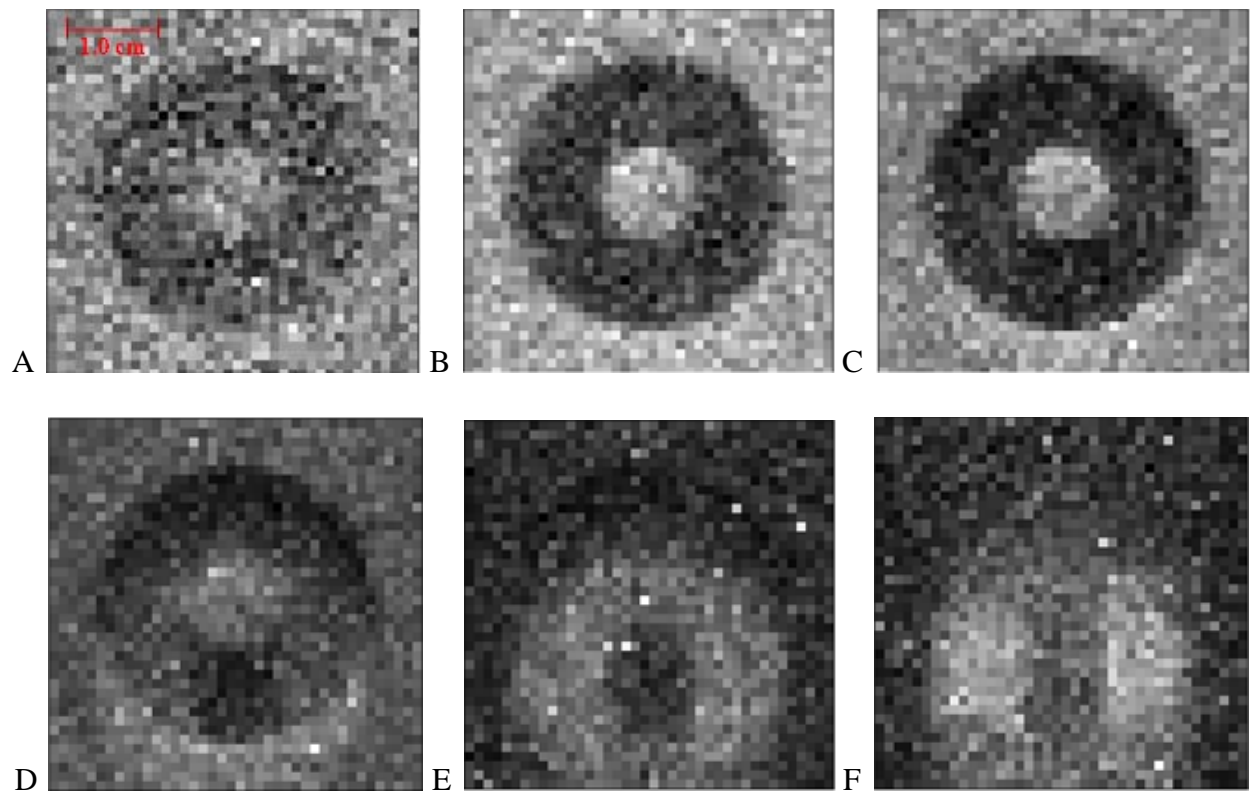


Figure 7-22. MCNP generated X-ray backscatter images of a ring of air inside aluminum using a 2D collimated segmented detector at a 45° inclination with a fan beam source. Each image correspond to one of the six rows of the pixelated detector A) row 1, B) row 2 , C) row 3, D) row 4, E) row 5 and F) row 6.

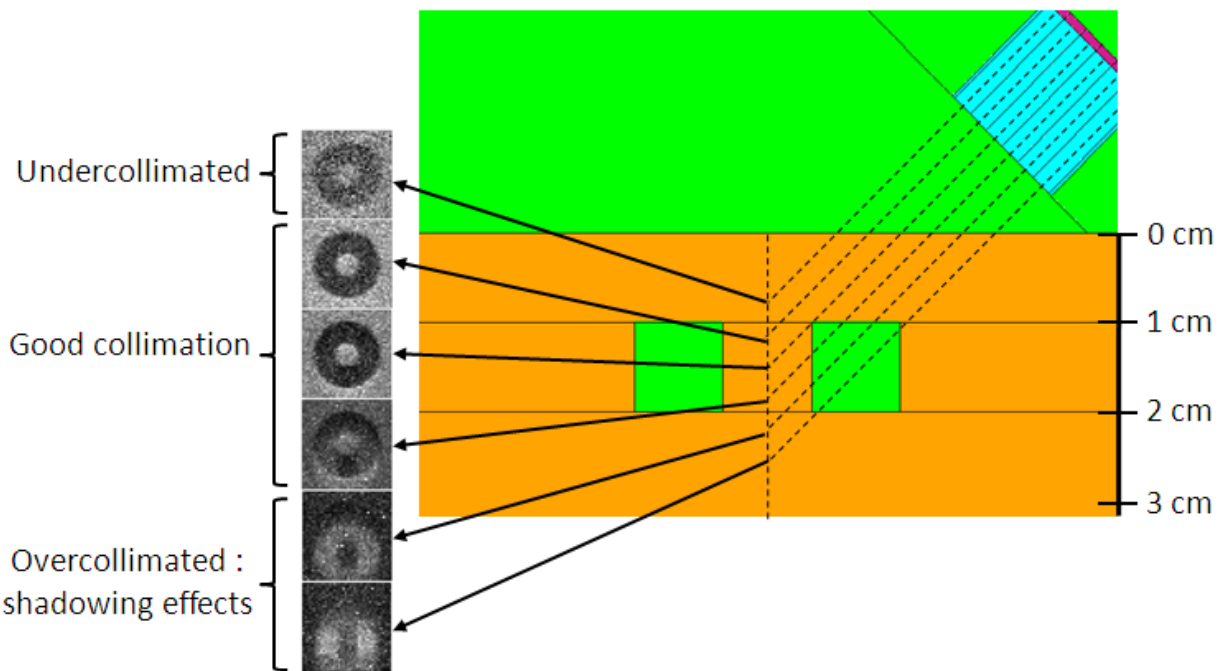


Figure 7-23. Z-levels corresponding to each of the six MCNP generated images of the ring of air.

CHAPTER 8

CSD-SXI: CONSTRUCTION AND TEST OF A FIRST PROTOTYPE

Experimental Setup

Segmented Detector

The detector used for the prototype is a 12 inch long linearly segmented CMOS detector built by Envision Product Design. It is shown in Figure 8-1. It is composed of three thousand, eight hundred and ten 80 micron wide pixels.¹¹ X-rays are allowed into the detector through a 2 mm wide and 1 cm deep collimated slot in the tungsten housing and strike the scintillator. The visible light produced is then guided via fiber optics to a CMOS active-pixel sensor array (Figure 8-2). The slot in the tungsten provides depth collimation. The detector is mounted on the X-ray tube stand, 4 cm away and 9 cm below the X-ray tube window. It is given a 40 degree angle toward the X-ray source because the collimation slot is so tight that no photon would be detected otherwise (Figure 8-3).

The segmented detector is connected to a workstation through a PCI card. Software displays in real time the intensity recorded by each pixel. It is possible to group up to 16 pixels together, which is very useful because the pixel bins must be of the same size as the collimation grid pitch. The integration time can vary from 6 to 4000 ms, and while times as short as 20 ms are commonly used for direct transmission imaging, integration times between 500 and 2000 ms are needed for X-ray backscatter imaging purposes. A function allows recording a grey level image for a given scanning speed. The RSD motion control software was used to move the X-ray source and the detector for the scan. Before the acquisition of an image, calibration of the detector must be performed each time the target background and the X-ray tube voltage are significantly modified. This is done automatically by the software and takes between two and

five minutes. A successful calibration should result in a straight line across the whole detector as shown in Figure 8-4.

Collimation Grid

The collimation grid for this CSD-SXI prototype is made of about eighty 0.4 mm (or 1/64") thick lead plates and twice as many spacers glued together , in an alternating pattern resulting in a 7 cm long, 4 cm wide and 2 cm thick grid with a 0.88 mm pitch (Figure 8-5). Although the grid built with this method is not exactly evenly spaced, it was much less expensive than a specially machined tungsten grid would have been. Moreover, thanks to the calibration of the detector, irregularities in the grid, such as slightly bent lead plates, have no effect on CSD-SXI images. This collimation grid is mounted on the bottom part of the detector (Figure 8-6). Obviously, the lead collimation grid is critical to the quality of images. Figure 8-7 shows the difference between the image obtained with the segmented detector when it is collimated by the grid and when it is not. Shapes and details are only visible when the detector is collimated, while the uncollimated detector yields images with very limited contrast information and in only one dimension.

It was previously stated that pixel bins must be of the same size as the grid pitch. In fact, a first lead collimation grid was built with 1.06 mm (or 1/24") thick lead. The pitch of this grid, which is shown in Figure 8-8, was 2.18 mm. However, because the software only allows grouping up to 16 pixels, the maximum pixel bin size was 1.41 mm. This resulted in artifacts on CSD-SXI images; because more than one group of pixels or “super-pixel” are collimated by the same lead plates, they do not have the same perspective of the target object (Figure 8-9). Consequently, the different groups of pixels do not detect the same flux of X-rays during the transition between the background and a feature with a different scattering-to-absorption ratio,

and this leads to oscillation in image contrast as shown in Figure 8-10. MCNP simulations have confirmed this behavior.

X-ray fan Beam Source

Another important point is to have a sufficiently narrow fan beam X-ray source. In all previous MCNP simulations, it was assumed that the width of the beam was only 1 mm. In practice, a machined lead part with a 1 mm slit aperture that was designed to provide a fan beam source for CIBR (Figure 8-11A) was positioned at the X-ray tube exit window. However, the actual width of the fan beam with this lead shield is about 1 cm as shown in Figure 8-11B. MCNP simulations have shown that if the fan beam width is larger than a few millimeters, the image quality is greatly reduced. This is why another lead part was design to allow changing the aperture (Figure 8-12A). This shielding provides a narrower fan beam illumination, but on the other hand, the flux of X-ray photons received by the detector can be too low which can be a problem for both calibration and acquisition time (Figure 8-12B). Both Figure 8-11B and Figure 8-12B were obtained using the segmented detector pointed toward the moving X-ray source.

Test of the First CSD-SXI Prototype

Contrast and Details

The various objects shown in Figure 8-13A, were imaged using CSD-SXI and RSD. Figure 8-13B shows the CSD-SXI image of these objects on an aluminum background, taken at 120 kVp and 8.75 mA with an acquisition time of 3 minutes and 42 seconds (1000 ms integration time per pixel line). Figure 8-13C shows the RSD image of the same objects on the aluminum background, obtained with the same X-ray tube setup in 16 minutes 21 second. The first observation that can be made is that both images offer a similar level of detail, even though, most features are clearer on the RSD image. The plastic screwdriver handle for instance, is easily visible on the RSD image while it can barely be detected on the CSD-SXI image.

The ratio of contrast between the steel combination wrench and the aluminum background is about 0.4 on both the RSD and CSD-SXI images. However, the contrast ratio between the highly scattering plastic screwdriver handle and the background is 1.11 on the RSD image while it is indeterminate on the CSD-SXI image. On other CSD-SXI images of the same objects this plastic handle can be easily detected; it is a question of detector position and angle. The statistical error for the background is close to 4% for the CSD-SXI image, and it is as low as 0.7% for the RSD image.

Figure 8-14 shows letters of lead on a nylon background which were also imaged using CSD-SXI and RSD. Both images were obtained at 140 kVp and 4 mA, with acquisition time of 2 minutes and 46 seconds for CSD-SXI (1000 ms integration time per pixel line) and 8 minutes for RSD. It is clearer in this example that the quality of RSD images is better. Not only is the contrast better (lead-to-nylon ratio of 0.04 for RSD versus 0.12 for CSD-SXI), but the shape of the target object is much more accurate in the RSD image, and the gaps between the lead tiles composing the letters can even be detected although they are of the order of a few tenth of a millimeter.

Resolution and Modulation Transfer Function (MTF) for CSD-SXI

An attempt was made to quantify the resolution associated with CSD-SXI images. A test pattern composed of twelve 1 cm wide and 0.4 mm thick aligned lead tiles was scanned by CSD-SXI and RSD (Figure 8-15A). Because the resolution for CSD-SXI is not necessarily the same in both directions, parallel (Figure 8-15B) and perpendicular (Figure 8-15C) to the segmented detector), two images were taken for this system against only one for RSD (Figure 8-15D).

Figure 8-16 shows the MTF of the two CSD-SXI images and of the RSD image. While features as small as one millimeter can still be detected by RSD systems, this CSD-SXI prototype yields images with a better resolution in the direction parallel to the linearly segmented

detector than in the perpendicular direction. This is due to the fact that resolution in the parallel direction is controlled by the lead collimation grid with a 0.88 mm pitch whereas the resolution in the perpendicular direction is a function of the 2 mm wide tungsten collimation slot. However, increasing the collimation in the direction perpendicular to the segmented detector by decreasing the width of the collimation slot, for instance would result in a lower count rate.

Depth Penetration

An important feature of X-ray backscatter imaging systems is the ability to detect features located behind another object or deep below the surface of an object. Figure 8-17A shows various objects such as a screwdriver, a wrench, steel and nylon washers, and screws on an aluminum background. Figures 8-17B and 8-17C show the CSD-SXI and RSD images of these objects without any cover at 140 kVp and 21.4 mA and at 120 kVp and 8.0 mA, respectively, with a 1000 ms integration time per pixel line for CSD-SXI and 50 ms per pixel for RSD. The contrast of both scattering (screwdriver's plastic handle, nylon washer) and absorbing (steel wrench, screws) materials relative to aluminum is equivalent on both images. However, even if all objects can be detected in both cases, the RSD image is clearer than the CSD-SXI; shapes are more precisely represented and even the objects' shadows appear very clearly on the RSD image. Figure 8-18 shows the RSD and CSD-SXI images of the same objects through 3.2 and 6.4 mm thick aluminum plates. The objects appear slightly more distinctly and with more contrast on the RSD images, but CSD-SXI images are also of fairly good quality. The plastic ruler on the other hand can hardly be detected in both CSD-SXI images. Figure 8-19 also shows the RSD and CSD-SXI images of the same objects on an aluminum background but this time through 2 mm and 6.4 mm thick carbon-carbon composite. The RSD and CSD-SXI image quality are roughly equivalent even though RSD offers images with much clearer contours than CSD-SXI. All the RSD images shown in Figures 8-17, 8-18 and 8-19 were all acquired in 10 minutes and 47

seconds against only 3 minutes and 42 seconds for the CSD-SXI images. It should also be noted that the lead collimation grid used for CSD-SXI was only 7 cm long. Increasing this length would result in a longer active area for the segmented detector and therefore, CSD-SXI image acquisition time would be reduced.

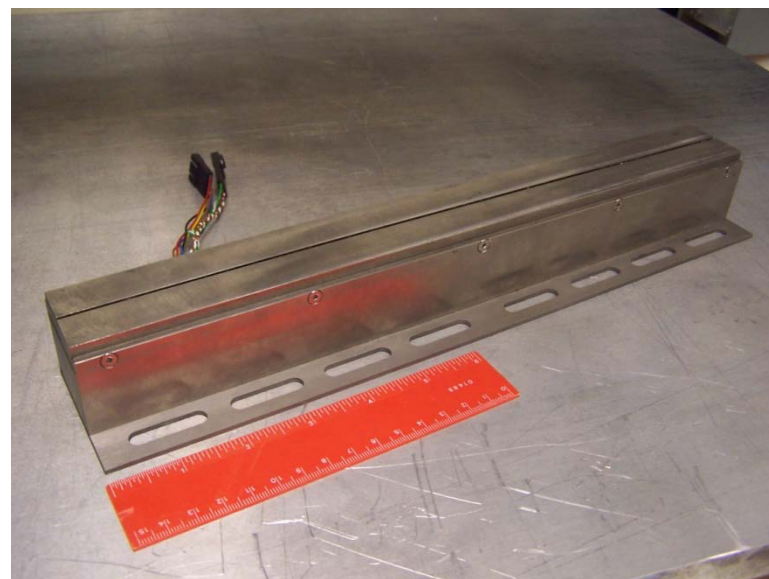


Figure 8-1. Photograph of the 12" Envision Product Design segmented detector.

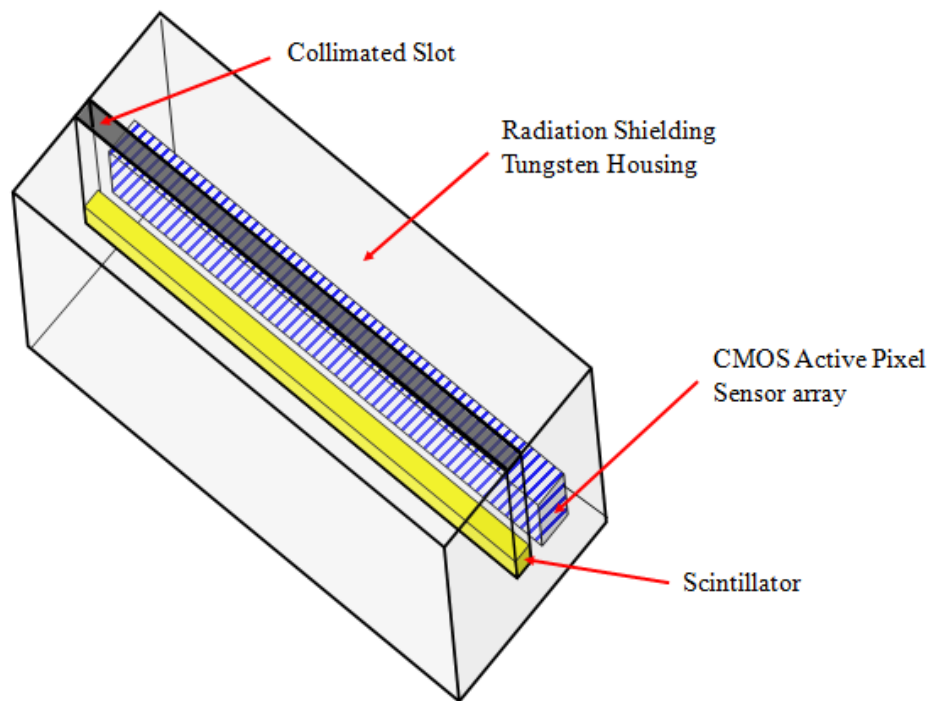


Figure 8-2. Simplified diagram of the segmented detector used for CSD-SXI.

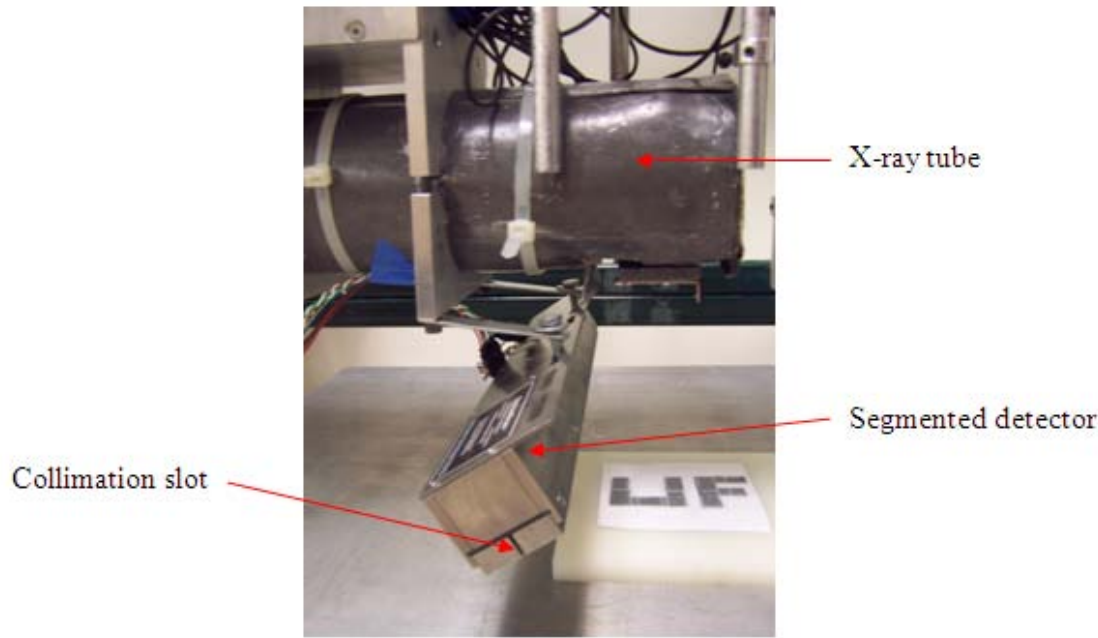


Figure 8-3. Segmented detector mounted on the X-ray tube at a 40° angle.

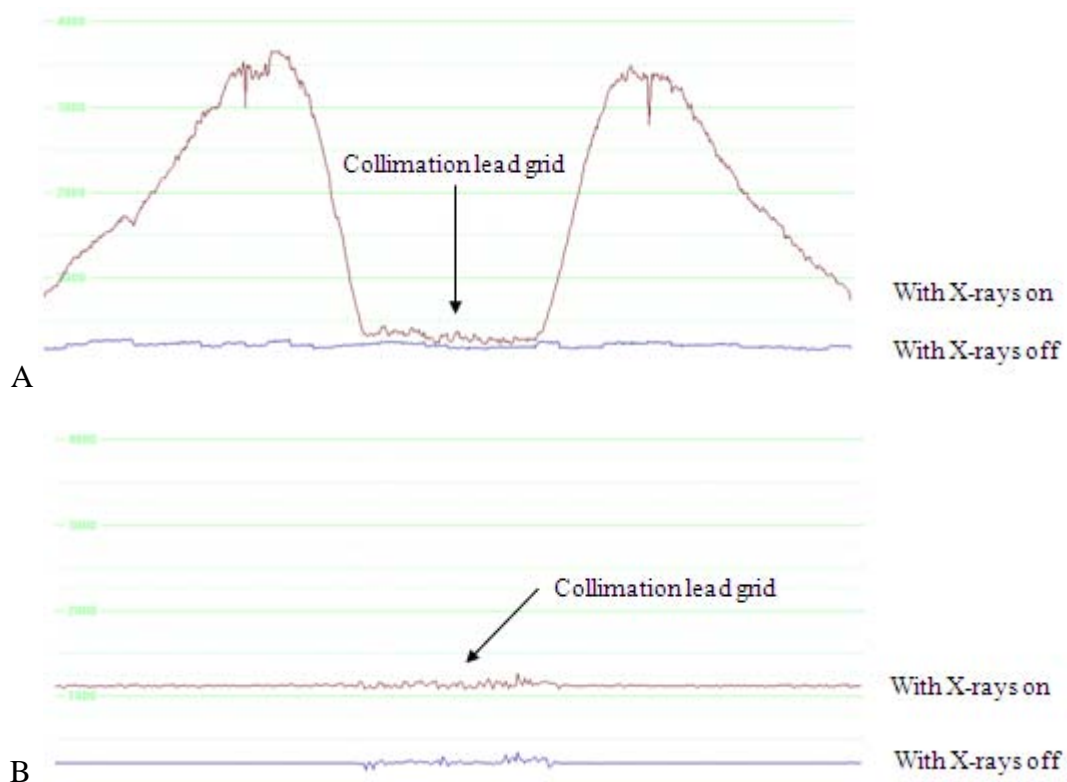


Figure 8-4. Flux detected by the linearly segmented detector with and without the X-rays on: A) before calibration and B) after calibration.

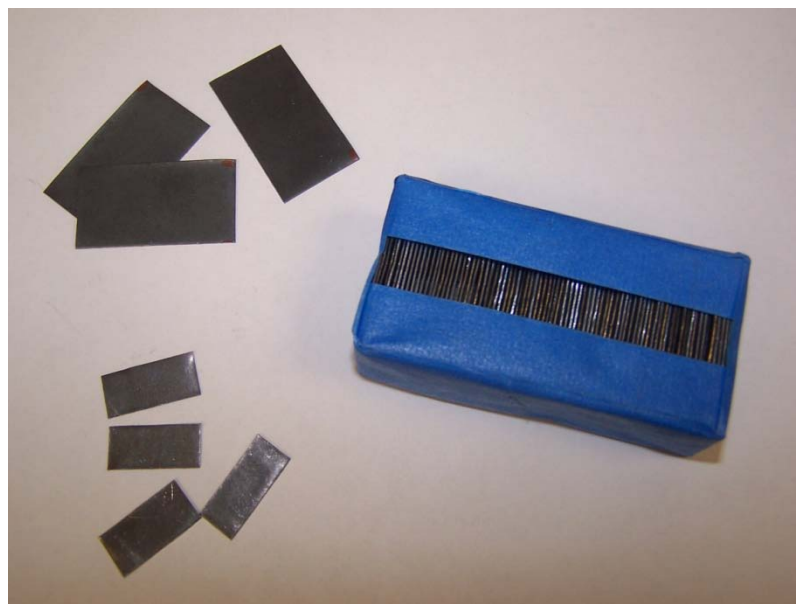


Figure 8-5. Collimation grid made of 0.4 mm thick lead.

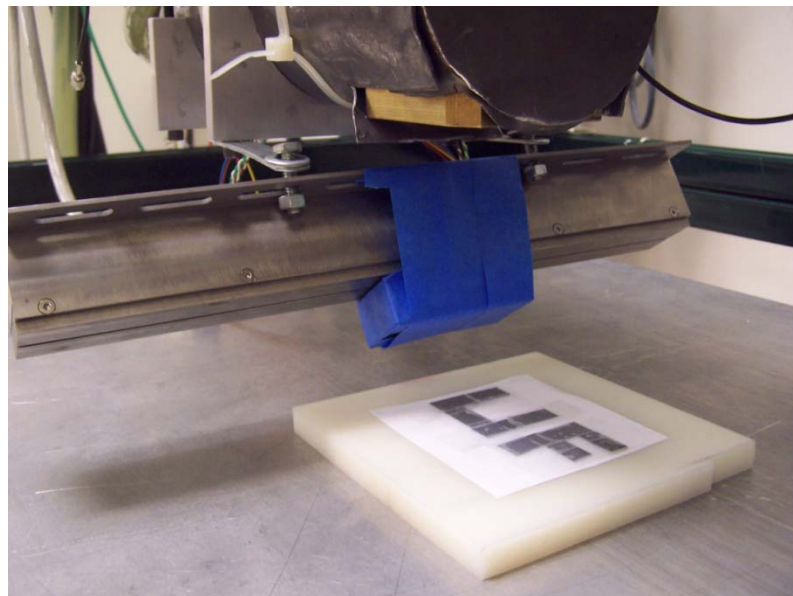


Figure 8-6. Lead collimation grid mounted on the bottom surface of the segmented detector.

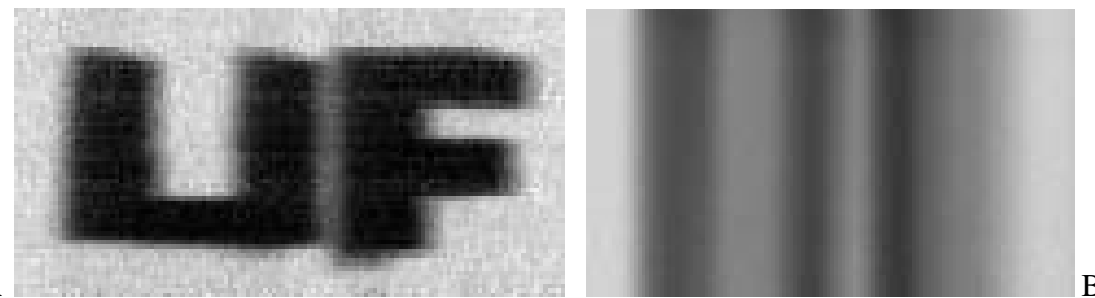


Figure 8-7. CSD-SXI image of letters of lead (1 mm thick) on nylon: A) with the lead collimation grid and B) without the lead collimation grid.

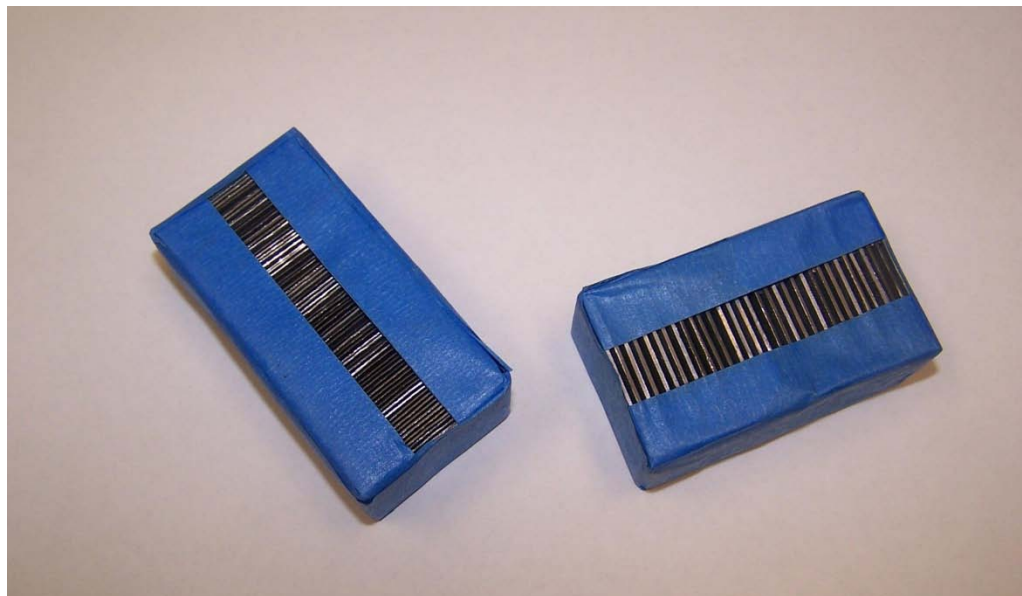


Figure 8-8. Lead collimation grids made of 0.4 mm and 1.08 mm thick lead plates and spacers.

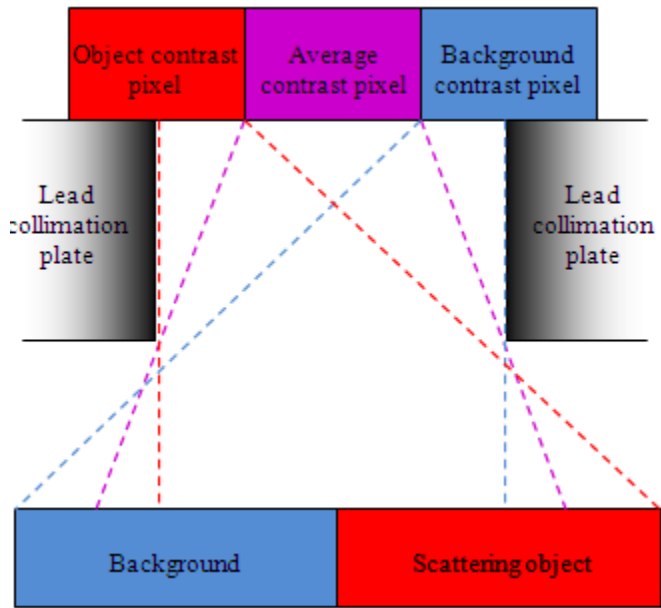


Figure 8-9. Explanation of the apparition of artifacts in CSD-SXI images when the collimation grid pitch does not match the size of pixel bins.

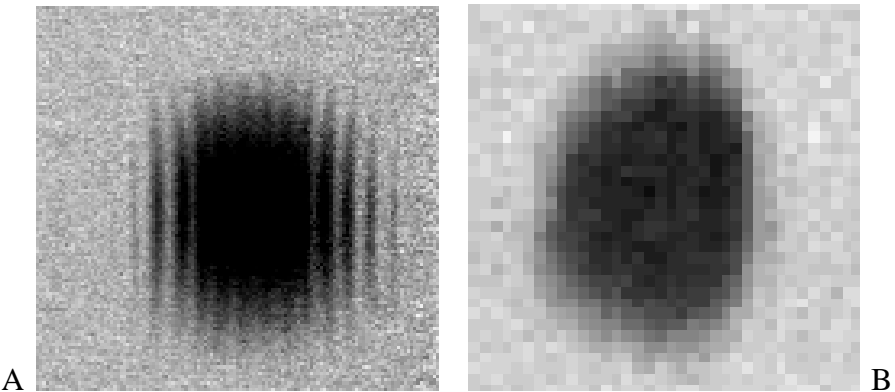


Figure 8-10. CSD-SXI images of a disk of lead on nylon: A) with a 2.18 mm collimation grid pitch and 0.4 mm pixel bins and B) with a 0.88 mm collimation grid pitch and 0.88 mm pixels bins.

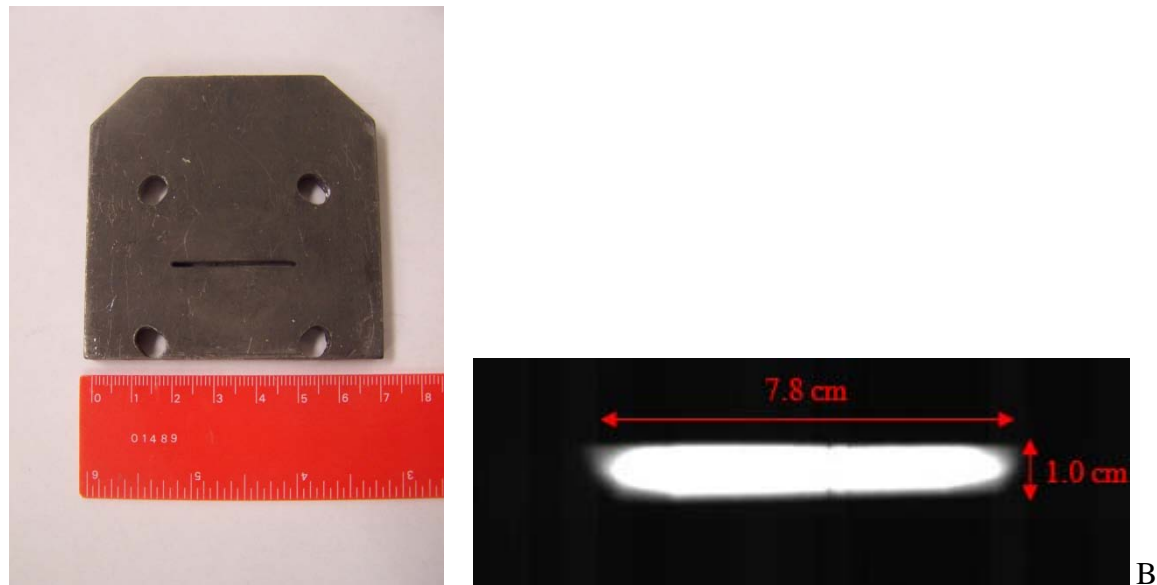


Figure 8-11. Lead shield with a 1 mm slit: A) photograph and B) Resulting X-ray fan beam at a 20 cm distance imaged with the segmented detector.

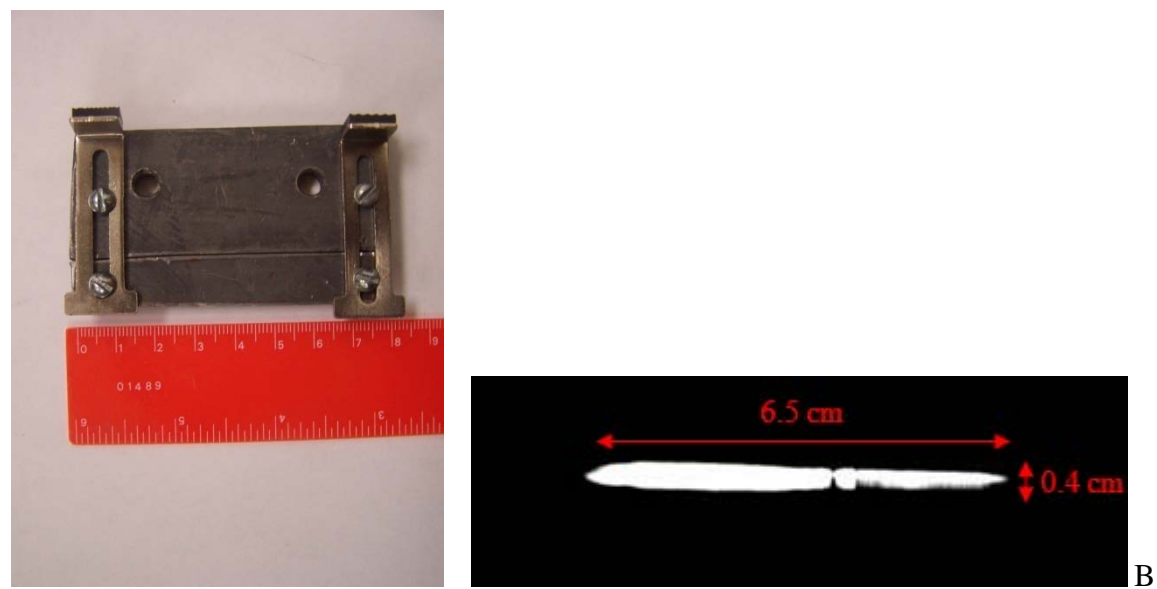


Figure 8-12. Lead shield with variable aperture, in this case 0.2 mm: A) photograph and B) Resulting X-ray fan beam at a 20 cm distance imaged with the segmented detector.

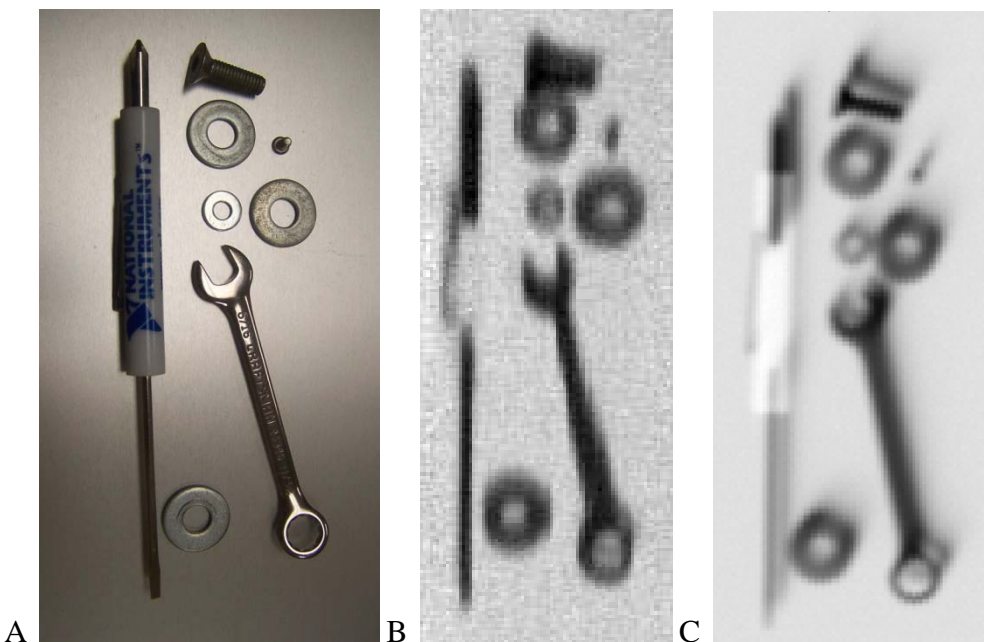


Figure 8-13. Various objects on an aluminum background: A) photograph, B) CSD-SXI image at 120 kVp and 8.75 mA and C) RSD image at 120 kVp and 8.75 mA.

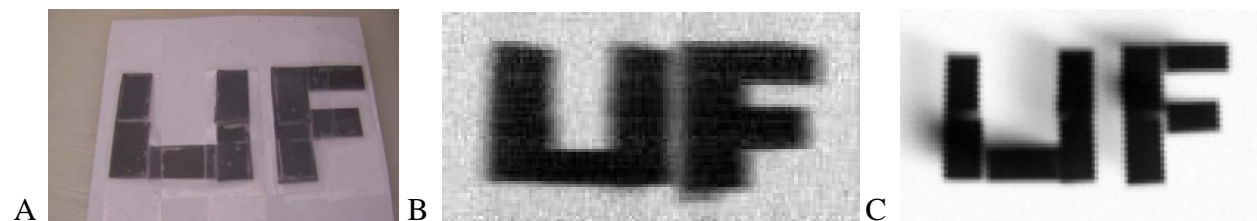


Figure 8-14. Letters of lead on a nylon background: A) photograph, B) CSD-SXI image at 140 kVp and 4 mA and C) RSD image at 140 kVp and 4 mA.

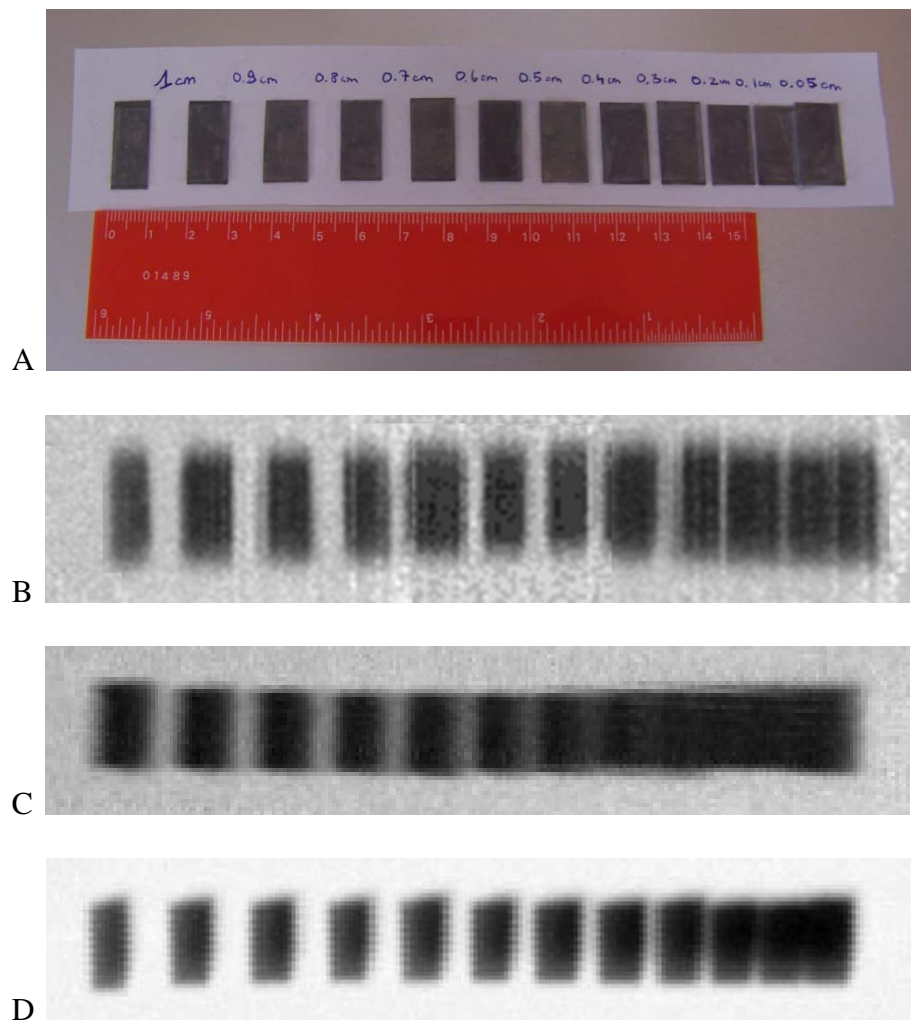


Figure 8-15. Lead test pattern on an aluminum background: A) photograph, B) CSD-SXI image at 120 kVp and 8.80 mA with the pattern parallel to the segmented detector, C) CSD-SXI image at 120 kVp and 8.80 mA with the pattern perpendicular to the segmented detector, and D) RSD image at 120 kVp and 8.80 mA.

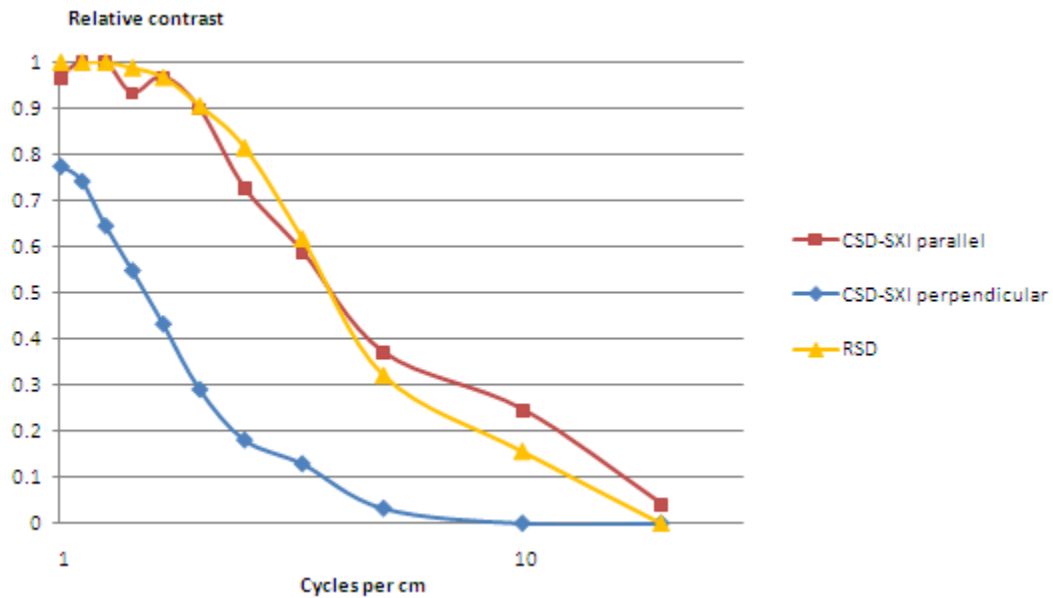


Figure 8-16. Modulation Transfer Functions (MTF) for the CSD-SXI and RSD images shown in Figure 8-15.

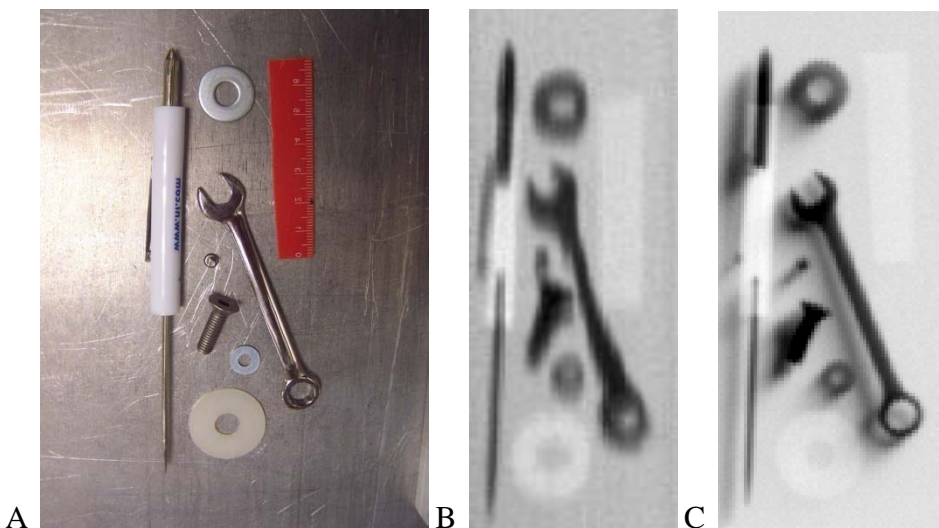


Figure 8-17. Various objects on an aluminum background: A) photograph, B) CSD-SXI image at 140 kVp and 21.4 mA, and C) RSD image at 120 kVp and 8.0 mA.

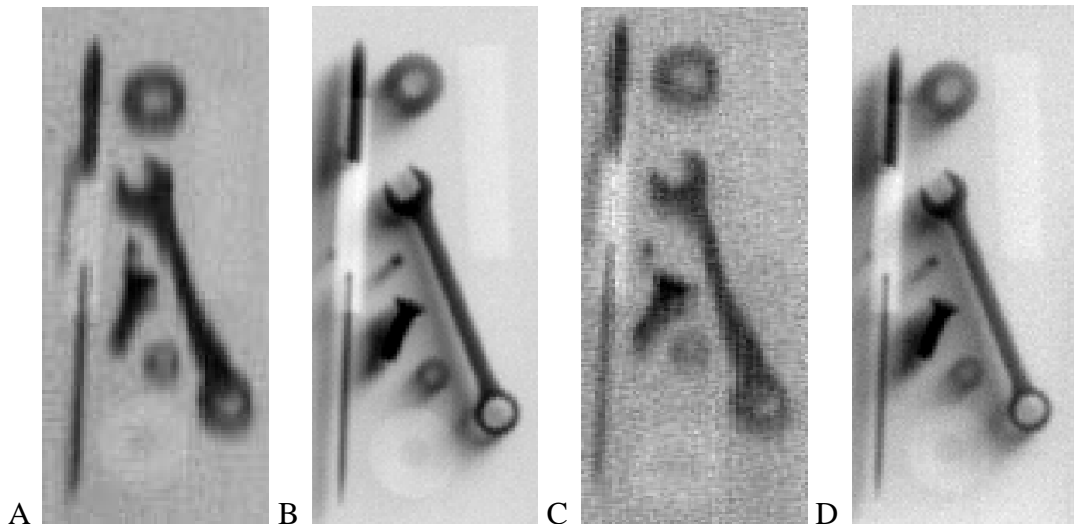


Figure 8-18. Various objects on an aluminum background: A) CSD-SXI image through a 3.2 mm thick aluminum cover at 140 kVp and 25.0 mA B) RSD image through a 3.2 mm thick aluminum cover at 120 kVp and 8.0 mA, C) CSD-SXI image through a 6.4 mm thick aluminum cover at 160 kVp and 18.75 mA and D) RSD image through a 6.4 mm thick aluminum cover at 120 kVp and 8.0 mA.

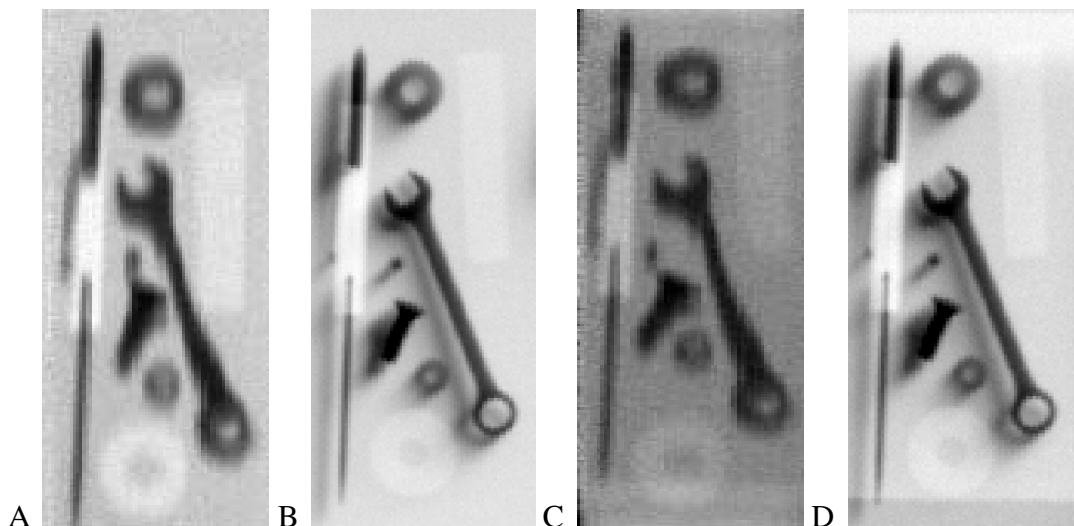


Figure 8-19. Various objects on an aluminum background: A) CSD-SXI image through a 2 mm thick carbon-carbon composite (C/C) cover at 140 kVp and 21.5 mA B) RSD image through a 2 mm thick C/C cover at 120 kVp and 8.0 mA, C) CSD-SXI image through a 6.4 mm thick C/C cover at 140 kVp and 21.5 mA and D) RSD image through a 6.4 mm thick C/C cover at 120 kVp and 8.0 mA.

CHAPTER 8

CSD-SXI: CONCLUSIONS AND FUTURE WORK

The association of collimated array detectors employing a lead or tungsten collimator grid with a fan beam source offers several advantages for X-ray backscatter imaging. The image acquisition time can be reduced relative to pencil beam systems such as RSD due to the use of the fan beam source and a simpler scanning pattern. Experimental tests on the prototype system have confirmed that CSD-SXI can yield images faster than RSD with an almost equivalent quality. Increasing the length of the collimator grid, and therefore the segmented active length, would also decrease image acquisition time.

However, the images obtained with RSD offer more distinct details of target objects than those taken with CSD-SXI. Moreover, the resolution of images obtained with this first CSD-SXI prototype in the direction perpendicular to the segmented detector is quite low compared to the resolution obtained with RSD. This could be solved by decreasing the width of the segmented detector collimation slot, but this would come at the cost of a smaller detection rate. More work is needed to improve these factors, but given the relative simplicity of this first prototype, significant progress can be expected.

MNCP simulations have shown that using a 2D collimated segmented detector could lead to accurate 3D backscatter X-ray imaging. This could be experimentally done by fitting a laser-cut tungsten collimation grid onto the bottom part of a 2D segmented detector. However, the fan beam source needs to be improved by building a lead shield with a finer slit than what is currently used because MCNP simulations have shown that too large a fan beam source adversely impacts the quality of 3D CSD-SXI images.

Other, more immediate future work includes writing a LabView program to provide a more adapted calibration for the segmented detector and to control the motion motors for easier image

acquisition. A small motor could also be placed on the segmented detector itself to control its angle and therefore the corresponding image depth.

LIST OF REFERENCES

1. A. JACOBS, E. DUGAN, D. SHEDLOCK, University of Florida Research Foundation, Inc, "Radiography by Selective Detection of Scatter Field Velocity Components", Patent No.: US 7,224,772 B2 (May 29,2007).
2. D. SHEDLOCK, B. ADDICOTT, E. DUGAN, and A. JACOBS, "Optimization of a RSD X-Ray Backscatter System for Detecting Defects in the Space Shuttle External Tank Thermal Foam Insulation", University of Florida (2005).
3. D. SHEDLOCK, "X-Ray backscatter imaging for radiography by selective detection and snapshot: evolution, development, and optimization", Ph.D. Dissertation, University of Florida (2007).
4. R. EVANS, "The Atomic Nucleus", p 683, Krieger Publishing Company (June 1982)
5. "Technical data", Kodak INDUSTREX Digital Imaging Plates, KODAK Publication No. TI-2632 (September 2006).
http://www.shawinspectionsystems.com/products/kodak/datasheets/EN_ti2632.pdf
6. "Film Based Portable X-ray Systems", Source-Ray, Inc (2005).
<http://sourceray.com/brochure/SR115%20-SR130%20Brochure%20web.pdf>
7. M. BERGER, J. HUBBELL, S. SELTZER, J. CHANG, J. COURSEY, R. SUKUMAR, and D. ZUCKER, "XCOM: Photon Cross Sections Database", NIST Standard Reference Database 8 (February 2009).
<http://physics.nist.gov/PhysRefData/Xcom/Text/XCOM.html>
8. C. MENG, "Computed Image Backscatter Radiography: proof of principle and initial development", Master Thesis, University of Florida (2008)
9. X-5 Monte Carlo Team, "MCNP – A General Monte Carlo N-Particle Transport Code, Volume II: User's Guide", LA-CP-03-0245, Los Alamos National Laboratory (April 2003)
10. G. KNOLL, "Radiation Detection and Measurement", p16, Third Edition, John Wiley & Sons, Inc (2000)
11. "CMOS Segmented Array™ Specifications", Envision Product Design (April 2003)
<http://cmosxray.com>

BIOGRAPHICAL SKETCH

Olivier Bougeant was born in Brittany, in northwestern France. After obtaining his high school diploma, he studied for two years in the “Classes Preparatoires aux Grandes Ecoles” in Rennes. He was then admitted to the “Ecole Nationale Supérieure de Physique de Grenoble” (ENSPG), where he obtained a bachelor’s degree in physics in 2007 and an Engineer’s degree in nuclear engineering in 2008. In 2007, he started a Master of Science in nuclear engineering at the University of Florida where he joined the Scatter X-ray Imaging group.